UNIVERSITY OF CALIFORNIA,
IRVINE

Understanding Regional Ice Sheet Mass Balance: Remote Sensing, Regional Climate Models, and Deep Learning

DISSERTATION

submitted in partial satisfaction of the requirements
for the degree of

DOCTOR OF PHILOSOPHY

in Earth System Science

by

Yara Mohajerani

Dissertation Committee:
Professor Isabella Velicogna, Chair
Professor Eric Rignot
Professor Mathieu Morlighem

2019

DEDICATION

To my parents.

TABLE OF CONTENTS

LIST OF FIGURES

LIST OF TABLES

ACKNOWLEDGMENTS

I would like to thank my advisor Dr. Isabella Velicogna for her guidance and support throughout my Ph.D. I am eternally grateful for numerous scientific, career, and life lessons from Dr. Velicogna during my years as a graduate student.

I would also like to thank my committee members, Dr. Eric Rignot and Dr. Mathieu Morlighem, for their constructive comments and insight. I am grateful for Dr. Rignot's collaboration and guidance on the published articles presented in this dissertation.

In addition, I would like to thank Dr. Tyler Sutterley for his invaluable input throughout my PhD, and Dr. Francois Primeau for numerous instructive conversations and learning opportunities.

I am grateful to the Earth System Science Department at UC Irvine, as well as the graduate student community. Special Thanks to the 2014 cohort for their support and friendship. Lastly, I would like to thank all the coauthors of the published material presented in this dissertation for their input and collaboration.

The work presented in this dissertation has been conducted at the University of California, Irvine, with support from the National Aeronautics and Space Agency (NASA), grant numbers NNX16AF69G, 80NSSC17K0698, and NNX15AE43G.

The American Geophysical Union and Wiley (publisher) have permitted the reprinting of previously published work in Geophysical Research Letters in Chapters 2 and 3 of this dissertation. Full cited is provided below:

Mohajerani, Yara, Isabella Velicogna, and Eric Rignot. "Mass Loss of Totten and Moscow University Glaciers, East Antarctica, Using Regionally Optimized GRACE Mascons." Geophysical Research Letters 45.14 (2018): 7010-7018. doi: 10.1029/2018GL078173.

Mohajerani, Yara, Isabella Velicogna, and Eric Rignot. "Evaluation of Regional Climate Models using Regionally-Optimized GRACE Mascons in the Amery and Getz ice shelves basins, Antarctica." Geophysical Research Letters. Accepted. doi: 10.1029/2019GL084665.

The work published in Remote Sensing with MDPI, Basel, Switzerland is under an Open Access license with copyright by the authors, and distributed under the terms and conditions of the Creative Commons Attribution (CC BY) license. Full citation for this work, which appears in Chapter 4, is provided below:

Mohajerani, Y.; Wood, M.; Velicogna, I.; Rignot, E. "Detection of Glacier Calving Margins with Convolutional Neural Networks: A Case Study." Remote Sensing 11.1 (2019): 74. doi: 10.3390/rs11010074.

CURRICULUM VITAE

Yara Mohajerani

EDUCATION

Doctor of Philosophy in Earth System Science — **December 2019**
University of California, Irvine — *Irvine, California*

International Summer School in Glaciology — **June 2018**
University of Alaska, Fairbanks — *McCarthy, Alaska*

Master of Science in Earth System Science — **June 2016**
University of California, Irvine — *Irvine, California*

H.B.Sc. in Physics and Mathematics — **June 2014**
with High Distinction
University of Toronto — *Toronto, Ontario, Canada*

CERTIFICATES

Data Science Certificate — **June 2017**
University of California, Irvine Data Science Program — *Irvine, California*

Scientific Writing and Publishing — **May 2017**
Nature Journal Masterclasses

PUBLICATIONS

Y. Mohajerani, Velicogna, I., Rignot, E. "Evaluation of Regional Climate Models using Regionally-Optimized GRACE Mascons in the Amery and Getz ice shelves basins, Antarctica',' *Geophysical Research Letters,* Accepted (2019).

Shepherd, A. et al. [including **Y. Mohajerani**] "Mass balance of the Greenland Ice Sheet from 1992- 2018." *Nature* Accepted (2019).

Britten G.L., **Mohajerani, Y.**, Primeau L., Aydin M., Garcia C., Wang W., Pasquier B, Cael B, Primeau F.W. "Bayesian research synthesis models in environmental science: a case study of marine organic carbon fluxes" *In Review at Frontiers in Environmental Science.*

Y. Mohajerani, M. Wood, I. Velicogna, E. Rignot, "Detection of Glacier Calving Margins with Convolutional Neural Networks: A Case Study," *Remote Sens.*, 11.1 (2019): 74. doi:10.3390/rs11010074.

Y. Mohajerani, Velicogna, E. Rignot, "Mass Loss of Totten and Moscow University Glaciers, East Antarctica, Using Regionally Optimized GRACE Mascons," *Geophysical Research Letters*, 45.14 (2018): 7010-7018. doi:10.1029/2018GL078173.

Pangaluru, K., Velicogna, I., **Mohajerani, Y.**, Ciracì, E., Cpepa, S., Basha, G., & Rao, S. "Soil Moisture Variability in India: Relationship of Land Surface–Atmosphere Fields Using Maximum Covariance Analysis." *Remote Sens.* 11.3 (2019): 335.

WCRP Global Sea Level Budget Group [including **Y. Mohajerani**] "Global sea-level budget 1993–present," *Earth Syst. Sci. Data*, 10, (2018) 1551-1590. doi:10.5194/essd-10-1551-2018

Shepherd, A. et al. [including **Y. Mohajerani**] "Mass balance of the Antarctic Ice Sheet from 1992 to 2017." *Nature* 556 (2018): pages219-222. doi:10.1038/s41586-018-0179-y

Kishore, P., Velicogna, I., Sutterley, T. C., **Mohajerani, Y.**, Ciracì, E., & Madhavi, G. N. "A case study of mesospheric planetary waves observed over a three-radar network using empirical mode decomposition." *Annales Geophysicae*. Vol. 36. No. 3. Copernicus GmbH, (2018).

Kishore, P., Jayalakshmi, J., Lin, P.L., Velicogna, I., Sutterley, T.C., Ciracì, E., **Mohajerani, Y.**, Kumar, S.B. "Investigation of Kelvin wave periods during Hai-Tang typhoon using Empirical Mode Decomposition." *Journal of Atmospheric and Solar-Terrestrial Physics* 164 (2017): 192-202.

S. Mohajerani, Percy, J.R. "Do Eclipsing Variable Stars Show Random Cycle-to-cycle Period Fluctuations?" *Journal of the American Association of Variable Star Observers (JAAVSO)* 39 (2011).

INVITED PRESENTATIONS

Gravity Recovery and Climate Experiment Follow-On **November 2019**
Space Studies Board Fall Meeting 2019 *Irvine, CA*
The National Academies of Sciences, Engineering, and Medicine

Mass Balance Estimates from GRACE **June 2018**
International Summer School in Glaciology *McCarthy, AK*

CONFERENCE PRESENTATIONS

Mohajerani, Y., Velicogna I., Sutterley T., Rignot E., Wiese D., "Evaluation of GRACE and GRACE-FO continuous solution on the ice sheets: harmonic inter-comparison and tai-

lored regional analysis." *GRACE-FO Science Team Meeting (GFO-STM) Continuity & Analysis Techniques, Pasadena, CA., Oct. 2019*

Velicogna I., **Mohajerani Y.**, Ciraci E, A. Geruo, Sutterley T., "Continuity of measurements of time-variable gravity across the GRACE and GRACE-FO missions over Greenland, Antarctica and the world's glaciers and ice caps" *GRACE-FO Science Team Meeting (GFO-STM) Cryosphere, Pasadena, CA., Oct. 2019*

He Z., Velicogna I., Ciraci E, Hsu C. **Mohajerani Y.**, Rignot E., "Reconstruction of 40-Year Measurement-Based Sea Level Fingerprints from Land-Ice Mass Changes" *GRACE-FO Science Team Meeting (GFO-STM) Oceanography, Pasadena, CA., Oct. 2019*

Mohajerani, Y., Velicogna I., Rignot E., "Regional Optimization of GRACE and GRACE-FO Processing and Inter-comparison with Regional Climate Models across the Antarctic Ice Sheet" . *AGU Fall Meeting, ABSTRACT C51A-07, Washington D.C., Dec. 2018*

Mohajerani, Y., Velicogna I., Rignot E., "Optimized Basin-Scale GRACE Harmonic Processing and Inter-comparison of GRACE Gravity Solutions in Antarctica". *GRACE/GRACE-FO Science Team Meeting (GSTM) B.2 Cryosphere GSTM-2018-81-1, Potsdam, Germany, Oct. 2018*

Velicogna I., **Mohajerani, Y.**, Ciraci E, A. Geruo, Sutterley T., "Time-variable gravity studies of ice sheets and glacier mass balance and partitioning of the water cycle in high mountain environment." *GRACE/GRACE-FO Science Team Meeting (GSTM) B.2 Cryosphere GSTM-2018-71, Potsdam, Germany, Oct. 2018*

Mohajerani, Y., Velicogna I., Sutterley T.C., Rignot E., "Regionally Optimized GRACE Processing and Inter-Comparison on the Antarctic Ice Sheet". *PARCA 2018 Meeting, College Park, Maryland, January 2018*

Velicogna I., **Mohajerani, Y.**, Sutterley T., "Glacier mass balance and surface mass balance evaluation with laser altimetry and other data." *Program for Arctic Regional Climate Assessment (PARCA) Meeting, College Park, Maryland, Jan. 2018*

Mohajerani, Y., Velicogna I., Sutterley T.C., Rignot E., "Regionally Optimized GRACE Processing and Inter-Comparison on the Antarctic Ice Sheet" *AGU Fall Meeting ABSTRACT G31B-0907, New Orleans, LA, Dec. 2017*

Kishore P, Velicogna I., Ciraci E., **Mohajerani, Y.**, "Evaluating the High Asia Reanalysis (HAR) using Gauge-based and Satellite Precipitation Data over High Mountain Asia." *American Geophysical Union (AGU) Fall Meeting, ABSTRACT H43D-1975, New Orleans, Louisiana, Dec 2017*

Mohajerani, Y., Velicogna I., Rignot E., Sutterley T.C. "Regionally Optimized GRACE Processing on Totten and Moscow University Glaciers." *GRACE Science Team Meeting (GSTM) B.3 Cryosphere, Austin, Texas, Oct. 2017*

Mohajerani, Y., Velicogna I., Sutterley T.C. "Optimization of Spherical Cap Mascon Processing on the Ice Sheets for the GRACE and GRACE-FO Missions." *CGU/CSAFM Annual Joint Meeting G03, Vancouver, Canada, May 2017*

Mohajerani, Y., Velicogna I., Sutterley T.C. "Optimization of Spherical Cap Mascon Processing on the Ice Sheets for the GRACE and GRACE-FO Missions." *AGU Fall Meeting ABSTRACT G13A-1092, San Francisco, CA, Dec. 2016*

Mohajerani, Y., Sutterley T.C., Velicogna I., Van den Broeke M.R., Fettweis X. "Reducing Uncertainties in Greenland Surface Mass Balance Using IceBridge and ICESat Altimetry, GRACE Data and Regional Atmospheric Climate Model Outputs." *AGU Fall Meeting ABSTRACT C23C-0803, San Francisco, CA, Dec. 2015*

Mohajerani, S., Kushner P., Derksen C. "October Eurasian Snow and its Effects on Wintertime Atmospheric Parameters." *Center for Global Change Science, University of Toronto, Toronto, Ontario, Aug. 2013*

TEACHING EXPERIENCE, DIVERSITY, AND OUTREACH

Teaching and Outreach at UC Irvine as a Minority Serving Institution (MSI), Asian American and Native American Pacific Islander-Serving Institution (AANAPISI) and Hispanic-Serving Institution(HSI):

Workshop on Website Development for Graduate Students **2018**

Developed content and instructed workshop for graduate students, particularly minorities and first-generation students, on developing student website and promoting their careers
Earth System Science graduate student retreat workshop

Introduction to Spatial-Temporal Statistics **Data Science Initiative, 2017**

Developed content, organized, and instructed course to graduate students at UC Irvine on key concepts and computational tools in spatial and temporal statistics
`https://github.com/yaramohajerani/SpaceTime`

Modelling the Earth *(ESS19)* **Earth System Science, 2017**

Teaching Assistant, Earth system modeling using STELLA

Sustainable Oceans *(ESS27)* **Earth System Science, 2016**

Teaching Assistant, concepts in sustainability, ocean pollution, and marine life

Oceanography *(ESS3)* **Earth System Science, 2016**

Teaching Assistant – general undergraduate introductory course in oceanography

Data Analysis *(ESS116)* **Earth System Science, 2015, 2016**

Teaching Assistant, scientific programming in earth system science using MATLAB – higher level undergraduate course

Training in inclusive teaching and active-learning techniques:

ESS Teaching Topics *(ESS280A)* **Fall 2015**
University of California, Irvine *Irvine, California*

Undergraduate-level physics tutoring **2013-2014**
Toronto, Canada

High school senior-level math tutoring **2013**
Tailored for women in STEM *Toronto, Canada*

RESEARCH EXPERIENCE

Graduate Research Assistant **Sept. 2014 – December 2019**
University of California, Irvine *Irvine, California*

Summer Internship **May – Aug. 2013**
Centre for Global Change Science (CGCS) *Toronto, Ontario, Canada*

Condensed Matter Physics **May – Aug. 2012**
Summer Research
U of Toronto, Dept. of Physics *Toronto, Ontario, Canada*

Undergraduate Researcher **May – Dec. 2011**
Condensed Matter Physics
U of Toronto, Dept. of Physics *Toronto, Ontario, Canada*

Student Summer Research Job **June – Aug. 2010**
U of Toronto, Dept. of Astronomy & Astrophysics *Toronto, Ontario, Canada*

Research Mentorship Program **Dec. 2009 – May 2010**
U of Toronto, Dept. of Astronomy & Astrophysics *Toronto, Ontario, Canada*

TECHNICAL SKILLS

Proficient in Python (NumPy, SciPy, MPI parallel processing, Matplotlib, Pandas, Shapely, rpy2, scikit-learn, scikit-image, etc.)

Neural Networks and Deep Learning with TensorFlow and Keras

Bash, HPC, Slurm, Cloud Computing

Linux/UNIX systems

Project management with Git/Github

Bayesian Stochastic Modeling in Stan, familiarity with PyMC3

Familiarity with MATLAB, R, STELLA

Working with NetCDF files (CDO, NCO, Ncview)

LaTeX, Markdown, and familiarity with HTML

ACHIEVEMENTS AND AWARDS

Altmetric's Top 100 Publications of 2018 — **December 2018**

Jenkins Family Graduate Fellowship — **October 2014**
Earth System Science, UC Irvine

KEGS Foundation Scholarship — **July 2014**
Canadian Exploration Geophysical Society

Don Salt Memorial Scholarship — **March 2014**
Canadian Exploration Geophysical Society

Hymie and Roslyn Mida — **January 2014**
Student Award in Theoretical Physics

The Dean's List — **June 2011-2014**
University of Toronto

Arthur Leonard Schawlow Scholarship — **June 2010-2013**
University of Toronto

Queen Elizabeth II — **September 2010-2013**
Aiming for the Top Scholarship

The 3T0 M&P and Associates Scholarship — **November 2012**
University of Toronto

Leslie Langbord Saunders Scholarship — **November 2011**
University of Toronto

Dr. John Knowles Colling Memorial — **August 2011**
University of Toronto

University of Toronto Scholar Scholarship — **September 2010**
University of Toronto

ABSTRACT OF THE DISSERTATION

Understanding Regional Ice Sheet Mass Balance: Remote Sensing, Regional Climate Models, and Deep Learning

By

Yara Mohajerani

Doctor of Philosophy in Earth System Science

University of California, Irvine, 2019

Professor Isabella Velicogna, Chair

The Antarctic and Greenland ice sheets are experiencing significant mass change with heterogeneous spatial and temporal characteristics and global consequences such as sea level rise affecting millions of people in low-lying coastal areas. Advances in large-scale satellite remote-sensing, modeling, and machine learning have ushered a new era of improved monitoring and understanding of these changes. In this dissertation, we analyze the mass balance of glaciers across the ice sheets at basin and sub-basin scales using satellite gravimetric data from the Gravity Recovery and Climate Experiment (GRACE) mission using a novel regionally-optimized mascon methodology, as well as Mass Budget Method (MBM) estimates from grounding line discharge measurements and surface mass balance from regional climate models. We find that Totten and Moscow University glaciers in the marine sector of East Antarctica, with a total 5-meter sea level rise potential, have been losing mass at a rate of 18.5±6.6 Gt/yr from April 2002 to August 2016. The MBM estimate obtained with RACMO2.3p1 (Regional Atmospheric Climate Model version 2.3 part 1) is in excellent agreement with GRACE at a sub-basin scale, while those obtained with RACMO2.3p2 and MAR (Modèle Atmosphérique Régional) version 3.6.41 show less negative trends. These results are robust with respect to Glacial Isostatic Adjustment (GIA) uncertainty. By extending this methodology to the Amery Ice Shelf drainage basin in East Antarctica, we find

this basin is in balance and is also in agreement with MBM/RACMO2.3p1 at a sub-basin scale, while MBM/RACMO2.3p2 and MBM/MAR3.6.41 produce more positive trends. The discrepancies shown by RACMO2.3p2 and MAR3.6.41 in these regions of East Antarctica are attributed to larger mean monthly SMB magnitudes. By adjusting all models to have the same mean magnitude as RACMO2.3p1, all MBM time-series fall into agreement with the independent gravimetric data. Furthermore, we implement the regional optimization approach in the Getz Ice Shelf drainage basin in West Antarctica, where previous studies have shown disagreements between GRACE and MBM estimates, and find that by minimizing leakage in the GRACE estimate, all MBM estimates are in excellent agreement with the gravimetric result. The Getz Ice Shelf basin is found to have a mass loss rate of 22.9±10.9 Gt/yr with an acceleration of 1.6±0.9 Gt/yr^2 from April 2002 to November 2015 (the common time-period with the MBM estimates). We use an ensemble of 128,000 GIA forward models to ensure the results are robust with respect to GIA uncertainty. Lastly, we focus on improving the monitoring and understanding of glacier dynamics by implementing a deep Convolutional Neural Network (CNN) to automatically delineate glacier calving fronts from Landsat imagery on the Greenland Ice Sheet. By training the network on Jakobshavn, Sverdrup, and Kangerlussuaq glaciers and testing it on Helheim glacier, we demonstrate that the performance of the network is comparable to that of a human investigator, with a mean CNN error of 1.97 pixels (96.3 meters) compared to a mean human error of 1.89 pixels (92.5 meters) on the same resolution images. Thus, we show that CNNs enable large-scale monitoring of glacier dynamics across the globe, which offers new possibilities for an improved understanding of the processes affecting the mass balance of glaciers. Ultimately, a better understanding of the ice sheets is crucial for a better assessment of the effects of a changing cryosphere and sea level rise around the globe.

Chapter 1

Introduction

1.1 Background

The cryosphere – the portion of the Earth System with frozen water – composes up to 35% of the world's surface [Marshall, 2011]. This vast sub-system includes the polar ice sheets, mountain glaciers, permafrost, snow cover, sea ice, lake and river ice, and even suspended ice crystals in the atmosphere. The ice sheets are the most prominent component of all the land ice. According to the official Glossary of Glacier Mass Balance and Related Terms [Cogley et al., 2011], an ice sheet is defined as *"An ice body that covers an area of continental size, generally defined as covering 50 000 km^2 or more"*. At present the Earth contains two ice sheets: The Greenland and Antarctic ice sheets. The Greenland ice sheet, covering an area of 1.7×10^6 km^2, contains 7.1 meters of sea level equivalent (the potential increase in sea level if the mass of the entire ice sheet was added to the oceans). The Antarctic ice sheet is much more massive with an area of 13.3×10^6 km^2 and enough ice to raise sea level by 56.2 meters [Marshall, 2011]. While ice sheets encompass the continental-scale mass of ice, individual glaciers are perennial bodies of ice that are massive enough to deform and flow as a

viscoplastic fluid under the force of gravity [Marshall, 2011]. Given the global significance of ice sheets and their large potential contribution to sea level rise, it is important to understand the processes that control the mass balance of glaciers across the ice sheets.

The Mass Balance (MB) of the ice sheets is governed by the mass influx on the surface through precipitation and out-fluxes as described below:

$$MB = SMB - D \tag{1.1}$$

SMB refers to the Surface Mass Balance of the glacier, which is the sum of all the fluxes on the surface of the ice. Formally, SMB is defined as:

$$SMB = snowfall + deposition - melt + refreezing - sublimation \tag{1.2}$$

(following Cuffey and Paterson [2010] where all deposition terms have been combined).

Secondly, D refers to ice discharge at the grounding line, which is the loss of ice mass due to the flow of glaciers. While discharge is not an out-flux for land-terminating glaciers, it is a significant component of the mass loss on the ice sheets (e.g. see Rignot et al. [2019]).

Not included in Equation 1.1 is melt at the base of the glacier due to friction and geothermal heat flux. This term is significantly smaller than surface mass balance and discharge and does not play an important role in the mass balance of ice sheets [Cuffey and Paterson, 2010].

The ice sheets have been losing mass at an accelerating rate in recent decades. The Antarctic ice sheet has been losing an average of 109±56 Gt/yr from 1992 to 2017, leading to a total of 7.6 ±3.9 millimetres of sea level rise [Shepherd et al., 2018]. The Greenland Ice Sheet lost mass at a rate of 286±20 Gt/yr from 2010 to 2018, almost 6 times more mass loss than the 1980s [Mouginot et al., 2019]. Velicogna et al. [2014] found accelerations of -10.6±3.7 and

-25.4±1.2 Gt/yr^2 for the Antarctic and Greenland ice sheets, respectively. Given the vast size of the ice sheets, the range of the processes affecting the mass balance, and the fast rate of change, it is essential to bring together observational and analytical techniques to better monitor and understand these changes across the ice sheets. There are three overarching approaches to evaluating the mass balance of the ice sheets: 1) Gravimetric: directly measure the change in gravity due to mass change; 2) Altimetry: measure the change in surface elevation to infer mass change; 3) Mass Budget: use measurements and models to quantify input and output mass fluxes. This dissertation focuses on the gravimetric and mass budget methods, which are explained below. Furthermore, new developments in computer vision and deep learning provide additional ways to analyze vast quantities of visual remote sensing data to better understand the dynamics of glaciers. This is discussion in the last section. Finally, we discuss the main objectives and the outline of the dissertation.

1.2 Gravity Recovery and Climate Experiment

The Gravity Recovery and Climate Experiment (GRACE) mission was launched in March 2002 as a collaboration between the German Space Agency (DLR) and the National Aeronautics and Space Administration (NASA) to provide monthly solutions of changes in the Earth's gravitational field [Tapley et al., 2019]. The GRACE mission provided the scientific community with direct observations of mass change, from which changes in ice sheets and glaciers, terrestrial water storage, ocean, and atmospheric dynamics could be inferred on a monthly time-scale. GRACE was decommissioned in October 2017 [Tapley et al., 2019]. However, with the successful launch of the GRACE Follow-On (GRACE-FO) mission in 2018, the monthly gravity solutions continue to provide insights into changes of the earth system [Tapley et al., 2019].

The GRACE mission was composed of a pair of twin satellites separated by a distance of

220±50 km [Tapley et al., 2019]. At an altitude of 500 km, each twin satellite was equipped with a microwave "K-band" ranging system for precise determination of the distance between the two satellites. In addition, each satellite had a GPS (Global Position System) receiver, altitude sensor, and accelerometer for non-gravitational forces on the surface [Tapley et al., 2004]. In addition to these components, the GRACE-FO satellites are also equipped with an experimental Laser Ranging Interferometer (LRI) that is 26 times more accurate than the k-band system for measuring the inter-satellite distance [Tapley et al., 2019]. The twin satellites experience gravitational anomalies by the change in the inter-satellite distance (the range-rate data), as they fly over mass anomalies. As the satellites approach a positive mass anomaly, the inter-satellite distance increases as the first satellite experiences a greater gravitational force along the direction of motion. As the satellites pass over the mass anomaly, the first satellite decelerations as it is pulled back by the mass anomaly while the second satellite speeds up towards the anomaly. Finally, once the satellites move passed the anomaly along the orbit, the inter-satellite distance returns to normal. Thus, the range-rate data can be used to produce monthly maps of the Earth's gravitational field as the satellites orbit around the planet.

The data processing is done through three primary centers: the Center for Space Research (CSR) in Austin, Texas, NASA's Jet Propulsion Laboratory (JPL), and the German Research Centre for Geosciences (GFZ). These centers process the range-rate and auxiliary data to provide monthly solutions at various levels of processing. Level-0 and Level-1A represent raw or minimally processed data, such that the raw Level-0 data can mostly be re-extracted from level-1A data. Level-1B (L1B) represents the processed range-rate data with proper time tags and all the auxiliary data required for further processing. This level of processing is not reversible for obtaining lower levels of data. Level-2 (L2) data provides the monthly geoid field in the form of spherical harmonics. In this dissertation we work with the spherical harmonic data to obtain regional estimates of mass balance.

The geoid, defined as an equipotential surface of the gravitational field corresponding to the mean sea level, is conveniently expressed in spherical coordinates using spherical harmonic sums [Wahr et al., 1998]:

$$N(\theta,\phi) = a\sum_{l=0}^{\inf}\sum_{m=0}^{l}\tilde{P}_{lm}\cos\theta[C_{lm}\cos(m\phi) + S_{lm}\sin(m\phi)] \tag{1.3}$$

where N is the geoid height, a is the radius of the Earth, θ is colatitude, ϕ, is longitude, and $\tilde{P}_{lm}$ are normalized Legendre polynomials (see sections 1.7-1.8 of Hofmann-Wellenhof and Moritz [2006]). C_{lm} and S_{lm} are the Stokes coefficients specifying the geometry of the geoid. The time-variable gravity field measured by GRACE / GRACE-FO is expressed as the change in the stokes coefficients (ΔC_{lm} and ΔS_{lm}) to derive the monthly change in the geoid.

Assuming most of the change in the gravity solutions are restricted to the surface of the Earth on a short time-scale (due to the transport of mass on surface through processes such as the transport of water), the corresponding change in mass density is given by [Wahr et al., 1998]:

$$\Delta\sigma(\theta,\phi) = \frac{a\rho_{avg}}{3}\sum_{l=0}^{\inf}\sum_{m=0}^{l}\frac{2l+1}{1+k_l}\tilde{P}_{lm}\cos\theta\,[\Delta C_{lm}\cos m\phi + \Delta S_{lm}\sin m\phi] \tag{1.4}$$

where ρ_{avg} is the average density of Earth and k_l is the Love number associated with the additional solid Earth deformation due to the surface loading.

Note that while Equation 1.4 has an infinite sum, due to the limited resolution of the satellites the harmonics are only provided up to degree (l) and order (m) 60. This roughly translates to

a spatial resolution of $\frac{20{,}000}{60}$ km $\approx$ 333 km [Swenson and Wahr, 2002]. This limitation leads to a smoothed spatial field when the surface density is directly obtained from the global Stokes coefficients. This smoothed and spatially-correlated field does not provide a true isolated regional mass balance estimate at each point. Regional estimates of mass change are obtained through several methods including averaging kernels (e.g. Velicogna and Wahr [2006]), forward modeling (e.g. Chen et al. [2011]), as well as mascon processing. Here we focus on the various mascon processing approaches.

The mascon approach for obtaining localized mass change estimates falls into two general categories: 1) simultaneous least-squares inversion in the spectral domain (from Level-2 data); 2) mascon inversion from range-rate (level-1 data). In the spherical harmonic approach, a set of locally-defined regions or mascons are converted to the spectral domain assuming uniform and unitary (1 unit) mass change. The mascons are simultanously regressed against the global GRACE harmonics to find the mass of each mascon with the following cost function:

$$\epsilon = \sum_{l,m} \left[\left(\Delta C_{l,m}(t) - \sum_i C^i_{l,m} M_i(t) \right)^2 + \left(\Delta S_{l,m}(t) - \sum_i S^i_{l,m} M_i(t) \right)^2 \right] \tag{1.5}$$

where the summation is over each mascon i with mass M_i. [Jacob et al., 2012].

Given the linearity of all the equations, the mass of mascon M_i can be related to the surface density field by

$$M_i(t) = \int \Delta\sigma(\theta, \phi, t) A_i(\theta, \phi) r^2 \sin(\theta) d\theta d\phi \tag{1.6}$$

Where A_i is the sensitivity kernel function, representing the mass being sampled by the mascon [Jacob et al., 2012]. This approach relies on the fact that the mascons can be shown to be orthogonal if the mass is distributed uniformly inside each mascon and zero outside.

In other words, for two mascons i and j, we have

$$\frac{1}{S_j}\int_{s_j} A_i(\theta,\phi)\sin(\theta)d\theta d\phi = \delta_{i,j}$$

Where S is the surface area of the mascon.

If the mass inside each mascon is not uniformly distributed, the kernels are not orthogonal and the mascons can be contaminated by mass elsewhere on the ice sheet. Therefore, the design of the mascons depends on a few important factors: firstly, the mascons should be placed such that the mass change is roughly uniform inside and zero outside of the mascons. Secondly, the size of the mascons depends on the signal-to-noise ratio in the data. Most of the noise in the data are contained within the higher degree terms [Wahr et al., 2006], which also contain the higher resolution spatial information. Therefore, the size of the mascons should strike a compromise between the desired degree of spatial resolution and the noisy higher degree harmonics.

While the harmonic approach provides more processing freedom to the user in terms of regional optimization of the processing, there are also mascon products calculated directly from the range-rate data from three different centers: the Center for Space Research (CSR), the Jet Propulsion Laboratory (JPL), and the Goddard Space Flight Center (GSFC) mascon solutions. JPL mascons use a weighted least-squares approach on a 3^o spherical cap grid with an a-priori covariance obtained from various observational and modeling outputs for land hydrology, oceans, inland seas, land ice, earthquakes and glacial isostatic adjustment [Watkins et al., 2015]. Additional processing such as the CRI (Coastal Resolution Improvement) filter and gain factors are also provided for reduction of leakage [Wiese et al., 2016]. The Goddard mascons, presented in Luthcke et al. [2013] are also derived from range-rate data in an iterative process with regional constraints. The oceanic, hydrological, and atmospheric constraints are obtained from forward modeling. The solution is provided on a

set of 1^o mascons. The fact that this is below the resolution of GRACE ($\approx$330 km) means that neighboring mascons are not fully separable and must be considered at a basin level in light of the associated covariance matrix. Similarly, the CSR mascons are provided on a 1^o caps. These solutions are regularized with only GRACE data itself in a 2-step time-variable regularization process [Save et al., 2016].

In addition to the processing of GRACE harmonics, there is the challenge of removing the component of mass change from the solid earth. While GRACE measures the total mass change in a given vertical cross section, we need to separate the surface ice mass change signal from those below. As ice sheets change mass over millennia and the surface load changes, the solid earth responds visco-elastically to the overhead mass change in a process called Glacial Isostatic Adjustment (GIA) [Peltier and Andrews, 1976]. The GIA response is calculated using forward models from the presumed history of ice loading, the viscoelastic properties of the Earth, and present-day measurement constrains, such as GPS uplift rates (e.g. see A et al. [2013]). In addition to global models, several regional models provide ice-sheet specific optimized regional models (e.g. Ivins et al. [2013] and Whitehouse et al. [2012] in Antarctica). The GIA response poses a particular challenge on the Antarctic Ice Sheet, where the GIA response has a comparable magnitude to that of ice mass loss. Using an ensemble of GIA models, Shepherd et al. [2018] estimated a mean GIA response of 54 Gt/yr with a standard deviation of 18 Gt/yr. An incomplete knowledge of ice history and processing of low degree harmonics pose challenges to an accurate GIA assessment [Shepherd et al., 2018]. Caron et al. [2018] have attempted to better quantify the uncertainty in GIA estimates by obtaining a full probability distribution from 128,000 forward model runs to capture the full covariance and the expectation value of the GIA response.

1.3 Mass Budget and Regional Climate Models

Another methodology for quantifying the mass balance of glaciers is to evaluate the total in and out fluxes (e.g. Rignot et al. [2008, 2011c, 2013, 2019]). As outlined in Equation 1.1, the mass balance is given by the surface mass balance (SMB) and discharge (D) terms. While in-situ measurements of SMB exist in small areas of the ice sheets (e.g. Van de Wal et al. [2012]), ice-sheet-wide observations of SMB are not available. However, regional climate models constrained by reanalysis products at the boundaries are able to simulate SMB at multi-kilometer scales across the ice sheets. Two such regional climate models are the Regional Atmospheric Climate MOdel (RACMO) and Modèle Atmosphérique Régional (MAR). RACMO, developed by the Royal Netherlands Meteorological Institute (KNMI) simulates Antarctic SMB with a resolution of 27 km, with an addition of a high-resolution 5.5km model for the Antarctic Peninsula [van Wessem et al., 2018]. The corresponding Greenland model is run at a resolution of 11 km [Noël et al., 2018]. RACMO uses the dynamics of the High Resolution Limited Area Model (HIRLAM) [Undén et al., 2002] and a multilayer snow model. The model is forced at the boundaries by the ERA-Interim reanalysis [Dee et al., 2011] (and ERA-40 [Uppala et al., 2005] before 1979 in the case of Greenland) [van Wessem et al., 2018, Noël et al., 2018]. MAR is also forced by ERA-Interim in Antarctica, with additional runs available forced by MERRA-2 (Modern-Era Retrospective Analysis for Research and Applications version 2) [Gelaro et al., 2017] and JRA-55 (Japanese 55-year Reanalysis) [Kobayashi et al., 2015]. The Antarctic run is provided at a resolution of 35 km [Agosta et al., 2019]. The Greenland model, forced by ERA-40 (1958-1978) and ERA-Interim (1979-), is provided on a 20 km resolution. MAR uses the SISVAT (Soil Ice Snow Vegetation Atmosphere Transfer) surface model [De Ridder and Gallée, 1998], which includes a multilayer energy balance model based on the CROCUS snow model [Brun et al., 1992, Fettweis, 2007, Agosta et al., 2019].

The second component of the mass budget comes from measurements of discharge. A refer-

ence flux is calculated from measurements of ice thickness and reference ice velocity. The flux is then scaled based on ice velocity measurements at each time-step to produce the discharge flux [Rignot et al., 2019]. Flux gates can also measure the discharge flux at the grounding line [Rignot and Kanagaratnam, 2006]. Subtracting the total discharge at the grounding line of the drainage basin of a glacier from the integrated SMB of the basin provides the total mass balance of the glacier at each time step. By bringing together modeled SMB products and discharge observations, the Mass Budget Method allows for a high-resolution mass balance calculation of individual glaciers across the Greenland [Mouginot et al., 2019] and Antarctic [Rignot et al., 2019] ice sheets.

1.4 Machine Learning in Cryospheric Remote Sensing

In addition to the aforementioned remote-sensing and modeling advancements in cryospheric research, the ever-increasing wealth of data demands new approaches in the analysis and interpretation of the data. For example, Landsat satellites have been gathering images of the Earth since the launch of Landsat-1 in July of 1972 with a repeat cycle of 16 to 18 days [Survey, 2015]. This visual imagery database provides an invaluable resource for a better understanding of the behavior and dynamics of glaciers across the globe. Furthermore, with the current advent of more numerous and higher resolution remote-sensing satellites such as ICESat-2 (laser altimetry) [Markus et al., 2017], Sentinel-1 (synthetic aperture radar) [Potin et al., 2018], Landsat-8 [Roy et al., 2014], and smaller scale CubeSat constellations [Gogineni et al., 2018], it is a challenge to fully utilize the ever-increasing stream of data for scientific purposes. Nevertheless, these finer scale observations provide unique information that is not available with the larger scale observations such as GRACE gravity data or basin-scale mass budget data. For example, high resolution images of glacier calving fronts provide valuable information about the location of the glacier front over time. As glaciers advance and

retreat over time, the precise mapping of the calving front highlights the accumulation and ablation processes acting on the glacier. Understanding the effect of ice-ocean interaction, a major driver of ice mass loss, utilizes such mapping information (e.g. Rignot et al. [2016]). Furthermore, the temporal resolution of the mapping information is crucial for a better understanding of glacier dynamics, such as understanding the seasonal dynamics of tide-water glaciers in Greenland [Wood et al., 2018]. However, much of this work relies on manual procedures in Graphical Information Systems (GIS), such as the delineation of glacier calving fronts from hundreds of remote-sensing products. The limited scalability of the current procedures, combined with the expanding wealth of remote-sensing data has posed a challenge for new approaches to monitoring and understanding cryospheric processes at higher temporal and spatial resolutions across many products.

Developments in machine learning and artificial intelligence have, for the first time, allowed us to match the scalability of data with that of interpretation. In particular, the utilization of neural networks in computer vision has produced remarkable success. Classification of images with neural networks has even been shown to surpass human performance in some cases [He et al., 2015]. Artificial neural networks, roughly inspired by their biological counterparts, are a connected network of nodes where each "neuron" gets a set of numerical inputs from the previous layer of neurons, and calculates a new output based on a learned threshold or bias and a given activation function. This is illustrated by a simple three layer network in Figure 1.1. The red node receives two inputs from the previous layer, x_1 and x_2, weighted by w_1 and w_2 respectively. Given a bias b, the node has an input value of $z = \sum_i (x_i w_i) + b$. Finally, an activation function produces the output of the unit given $f(z)$ [LeCun et al., 2015]. Various activation functions are used in neural networks, such as the Sigmoid, hyperbolic tangent [Karlik and Olgac, 2011], and Rectified Linear Units (ReLU) [Nair and Hinton, 2010]. The activation function applies nonlinear transformations to the outputs of the network at each layer such that an elaborate function can be learned by the network through the adjustments of the weights and biases using an optimization method such as stochastic gradient descent

[LeCun et al., 2015]. Many neural network architectures have been developed for a variety of tasks. Of particular importance to computer vision is the class of neural networks known as Convolutional Neural Networks (CNNs). These networks are composed of a series of kernels that are convolved across an image to extract features from different layers of the input data, combined with pooling layers that combine patches of the image into one, thereby course-graining the detected features and ensuring location-invariance of features within small patches [LeCun et al., 2015]. CNNs provide a way to extract features from remote-sensing products at a scale that is not achievable by human performance. With a stream of images of glaciers around the globe, such tools can help us quantify the position of the calving front and other desired quantities on a short temporal scale to better understand the seasonal or interannual processes that affect the dynamics of glaciers.

1.5 Objectives and Outline

This research focuses on the remote sensing of the ice sheets and refined observations and analyses to better assess regional mass balance and improve understanding of the governing processes. Specifically, the objective is to evaluate the regional mass balance of glaciers at basin and sub-basin scales, evaluate regional climate models and understand any disagreements, and examine glacier fronts at a high temporal resolution to better understand calving dynamics at seasonal or longer timescales across the ice sheets. To that end, the technical objectives are to 1) regionally optimize the GRACE mascon processing as described in section 1.2 based on the local characteristics to obtain meaningful basin and sub-basin estimates, 2) Evaluate corresponding sub-basin mass balance estimates with the Mass Budget method (section 1.3) with different regional climate models to examine SMB differences, 3) Utilize neural networks in the remote sensing of glaciers to examine glacier calving fronts at scale. In light of these objectives, this dissertation is divided into three chapters. Chapter 2 uses

regionally-optimized GRACE mascons to evaluate the mass balance of Totten and Moscow University glaciers in East Antarctica, and compare with independent estimates from the Mass Budget method using RACMO2.3 and MAR3.6.4 regional climate models. The full work can be found in Mohajerani et al. [2018].

Chapter 3 expands on the work presented in Chapter 2 by presenting regional mascon optimization for other key areas on the Antarctic ice sheet where the Mass Budget has higher uncertainty. Namely, we examine the mass balance of the Amery ice shelf basin in East Antarctica and the Getz ice shelf basin in West Antarctica. With an improved methodology, we examine potential biases in the regional climate models (RACMO2.3p1, RACMO2.3p2, and MAR3.6.4) in the Amery, Getz, and Totten/Moscow University basins. This research is currently submitted for publication.

Chapter 4 focuses on delineating the calving front of glaciers on the Greenland ice sheet using Convolutional Neural Networks (CNNs). Specifically, we focus on Jakobshavn, Sverdrup, Kangerlussuaq, and Helheim glaciers, where we show the delineations of the neural network are comparable to manual delineation by experts. The full report is accessible in Mohajerani et al. [2019b].

Finally, Chapter 5 provides a summary and conclusion of the presented work, the broader implications, and future work. Note that Chapters 2 to 4 are taken from the corresponding publications, with the permission of the publishers.

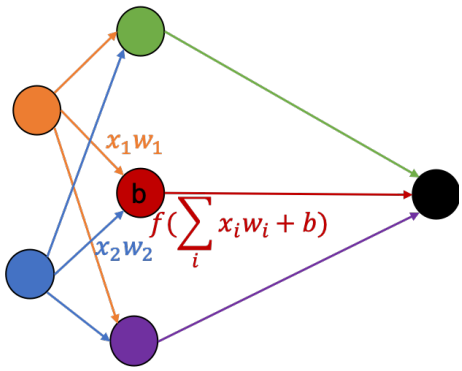

Figure 1.1: Simple representation of a three-layer neural network. The red node receives two weighted inputs and calculates an output based on a learned bias and and given activation function.

Chapter 2

Mass loss of Totten and Moscow University glaciers, East Antarctica, using regionally-optimized GRACE mascons

As Appears in:

Mohajerani, Yara, Isabella Velicogna, and Eric Rignot. "Mass Loss of Totten and Moscow University Glaciers, East Antarctica, Using Regionally Optimized GRACE Mascons." Geophysical Research Letters 45.14 (2018): 7010-7018. doi: 10.1029/2018GL078173.

Abstract

Totten and Moscow University glaciers, in the marine-based sector of East Antarctica, contain enough ice to raise sea level by 5 meters. Obtaining precise measurements of their mass balance is challenging owing to large area of the basins and the small mass balance signal compared to West Antarctic glaciers. Here, we employ a locally-optimized processing of GRACE harmonics to evaluate their mass balance at the sub-basin scale and compare the results with Mass Budget Method (MBM) estimates using regional atmospheric climate model version 2.3 (RACMO2.3) or Modèle Atmosphérique Régional version 3.6.4 (MAR3.6.4). The sub-basin mass loss estimate for April 2002 to November 2015 is 14.8±4.3 Gt/yr, which is weakly affected by glacial isostatic adjustment uncertainties (±1.4 Gt/yr). This result agrees with MBM/RACMO2.3 (15.8±2.0 Gt/yr), whereas MBM/MAR3.6.4 underestimates the loss (6.6±1.6 Gt/yr). For the entire drainage, the mass loss for April 2002 to August 2016 is 18.5±6.6 Gt/yr, or 15±4% of its ice flux. These results provide unequivocal evidence for mass loss in this East Antarctic sector.

Plain Language Summary

Totten and Moscow University glaciers in East Antarctica drain a marine-based sector that holds an ice volume equivalent to several meters of global sea level rise. Recent observations of warm water intrusion on the continental shelf suggest that the glaciers may be changing in response to ocean warming. Understanding this glacier evolution is therefore of global significance. Measurements are difficult to obtain in this region due to the shear size of the basins and small rate of mass loss compared to other parts of Antarctica. To resolve this problem and evaluate independent estimates, we present a new methodology to process Gravity Recovery and Climate Experiment satellite gravity data that is optimized at the

regional scale for these basins. Our results are in excellent agreement with independent estimates and provide unequivocal evidence that these glaciers have been losing mass rapidly for the past 15 years. We also compare different reconstructions of surface mass balance and determine that one model significantly underestimates the mass loss in this sector. A similar approach would be applicable to other parts of Antarctica to resolve residual uncertainties in its mass budget and contribution to sea level rise.

2.1 Introduction

The Antarctic Ice Sheet (AIS) has been losing mass at a mean rate of 67±44 Gt/yr for the time period January 2003 to December 2013, with an acceleration of 10.6±3.7 Gt/yr^2 [Velicogna et al., 2014]. Most of this mass loss originates in West Antarctica (WAIS) and the Antarctic Peninsula (APIS) [Rignot et al., 2008]. Shepherd et al. [2012] found that WAIS and APIS lost 65±26 and 20±14 Gt/yr between 1992 and 2011, while East Antarctica (EAIS) gained 14±43 Gt/yr. There are, however, large drainage sectors in East Antarctica that exhibit a significant mass loss and hold potential for major sea level rise. In particular, Totten Glacier has a sea level rise potential of 3.9 m [Li et al., 2015] versus 3.3 m for the entire marine sector of West Antarctica [Bamber et al., 2009]. Totten is the largest outlet glacier in East Antarctica [Li et al., 2016, Pritchard et al., 2009] in terms of its grounding line discharge of 71±3 Gt/yr between 2003 to 2008 [Rignot et al., 2013]. Li et al. [2016] reported a significant mass loss for this glacier and linked its temporal variability to changes in oceanic forcing from warm, modified, circumpolar deep water (mCDW) coming in contact with the glacier. The glacier has been thinning rapidly, up to 1.9 m/yr at low elevation between 2003 to 2007 [Pritchard et al., 2009]; however, a period of cold polynya water production that reduced intrusion of warm water beneath the ice shelf reduced thinning [Khazendar et al., 2013]. The nearby Moscow University Ice Shelf Glacier - or Moscow University - has

a grounding line flux of 52.3±1 Gt/yr [Rignot et al., 2013]. The glacier is marine based [Young et al., 2011] and contains 1.3 m sea level rise equivalent; however, evidence for ice thinning is less strong for Moscow University [Pritchard et al., 2009]. Actual ice shelf basal melt rates for the time period 2003-2008 are about half (4.7±0.8 m/yr) of those estimated for Totten (10.5±0.7 m/yr) [Rignot et al., 2013].

Recently, intrusion of warm (+0^{o}C to +0.5^{o}C), salty, mCDW was found at the entrance of the sub-ice-shelf cavity in front of Totten Glacier [Silvano et al., 2017]. This relatively warm mCDW is present year round and fuels intensified ice shelf melt rates of magnitudes almost comparable to those observed in the Amundsen Sea Embayment of West Antarctica. Oceanic wind stress upwells mCDW at the continental shelf break near the Totten ice tongue, modulating its melt rate with a 19-month lag period [Greene et al., 2017]. Spence et al. [2014] showed that the projected strengthening and poleward shift of southern hemispheric westerly winds under a more positive Southern Annular Mode (SAM) phase can induce significant warming of subsurface coastal waters, suggesting an acceleration in ice shelf melt in the future. Due to the vulnerability of these glaciers to enhanced mCDW intrusion in the future and its potential for considerable sea level rise, it is critical to evaluate, understand, and monitor the mass changes of these glaciers and ice shelves.

Gathering measurements in these two basins is difficult for a number of reasons. First, the glaciers have smaller rates of mass loss compared to their fast-moving counterparts in West Antarctica [Rignot et al., 2013], which reduces the signal-to-noise ratio when estimating mass balance. Second, the glaciers are difficult to access to airborne surveys and cover a large area, especially Totten Glacier (537,900 km^2 [Li et al., 2015] versus 221,600 km^2 for Moscow University). Third, there is a lack of reference velocity near the glacier fronts for ice motion measurements, so that reference velocities required for calibration of ice motion maps must be taken from the ice divides, hundreds of kilometers away inland, yielding long calibration baselines [Li et al., 2016]. Fourth, strong katabatic winds and pronounced gradi-

ents in snowfall accumulation along the coast compared to the rest of East Antarctica make measurements from satellites challenging because of rapidly changing surface conditions [Li et al., 2016]. It is therefore important to obtain and compare independent estimates of the mass balance to gain confidence in the results and reduce uncertainties.

Li et al. [2015] documented a 3-km grounding line retreat of Totten Glacier between 1996 and 2013 with InSAR (Interferometric Synthetic-Aperture Radar) data. Li et al. [2016] combined estimates of ice discharge with surface mass balance (SMB) data from the RACMO 2.3 regional atmospheric climate model [Van Wessem et al., 2014] to report a mass loss of 6.8±2.2 Gt/yr, with an acceleration of 0.55±0.27 Gt/yr^2 for the time period 1989 to 2015. The trend is dominated by the dynamic loss (73%), but the acceleration is almost entirely due to SMB (80%). The Mass Budget Method (MBM) study is limited by the precision of the SMB models in this region and by a time series of only 13 ice velocity measurements from 1989 to 2015.

These limitations are partly overcome by comparing the results with monthly gravity data from the Gravity Recovery and Climate Experiment (GRACE) satellite [Tapley et al., 2004], which is not affected by the uncertainty of SMB models and provides data on a monthly basis. GRACE estimates are provided at a coarse spatial resolution, however, due to the truncation of spherical harmonics at degree 60, or 333 km [Wahr et al., 1998]. This coarse resolution makes it difficult to derive basin-scale estimates of mass balance, especially if the change signal is small. A few studies have used GRACE data to study the Totten area. Chen et al. [2009] used a forward-modelling scheme to estimate the mass balance of Antarctica as the sum of nine uniform areas of large change plus the remaining area of the continent. For Wilkes Land, they found an ice loss rate of 13.4 Gt/yr for the period 2002 to 2009. More recently, Williams et al. [2014] used an AR1 autoregressive model to yield a mass change of only 0.52±0.98 Gt/yr with no significant acceleration near Totten Glacier

for the period March 2003 to July 2012. In contrast, Velicogna et al. [2014] used a uniform spherical cap least-squares fit method to estimate the mass loss of the larger domain of Totten/Moscow/Frost (TMF) sector at 17±4 Gt/yr, with an acceleration of 4.0±0.7 Gt/yr^2 for the period January 2003 to December 2013.

In this study, we employ an optimized regional spherical cap basis to recover a regional time-series at the sub-basin level in the Totten/Moscow area. The goal is to reduce the uncertainty of the mass balance estimates and compare them with the MBM to improve confidence in the results. Our methodology optimizes the signal retrieval over relatively small areas, where the mass loss signal is the strongest, and fully quantifies the errors, especially those associated with the leakage of the mascons. We compare MBM estimates using two SMB models to evaluate the SMB models using GRACE. We conclude on the mass balance of the Totten and Moscow University glaciers using these multiple estimates.

2.2 Data and Methodology

GRACE data: We use GRACE spherical harmonics of up to degree and order 60 provided in the RL05 solution from the Center for Space Research (CSR) at the University of Texas [Bettadpur, 2012]. Degree 1 harmonics, which are not measured in GRACE's center-of-mass frame, are calculated from the Ocean Model for Circulation and Tides (OMCT) that is already removed from the GRACE harmonics [Dobslaw et al., 2013] following Swenson et al. [2008]. In our calculation of degree 1, we destripe [Swenson and Wahr, 2006] and smooth the harmonics with a 300 km Gaussian smoothing filter (as described by Wahr et al. [1998]), apply pole-tide correction [Wahr et al., 2015], and subtract the Glacial Isostatic Adjustment (GIA) signal from three different models: 1) IJ05 [Ivins et al., 2013], 2) AW13 (A et al. [2013] combined with IJ05 in Antarctica) and 3) W12a [Whitehouse et al., 2012]. We use an ocean function that extends 300 km from the coast. We solve the geocenter iteratively,

starting from an initial estimate for ocean-land fluxes from Chen et al. [1999]. We replace the $C_{2,0}$ (degree 2, order 0) harmonic by monthly solutions obtained from satellite laser ranging (SLR) estimates [Cheng et al., 2013] both for the calculation of the geocenter term and for all subsequent calculations.

Spherical caps: To get regional estimates, we perform a simultaneous least-squares fit of the corrected spherical harmonics to spatially-defined mascons as in Jacob et al. [2012]. These spatially-defined regions form an orthogonal basis that allows us to transform the spherical harmonics into independent regional time-series. The key to obtaining regional time-series is to find an optimized basis for a given area. We use the spherical cap formalism outlined in Sutterley et al. [2014]. We assume that each cap has a uniform unitary mass distribution, which is converted into the harmonic domain and smoothed with a 250 km Gaussian filter [Wahr et al., 1998]. By simultaneously fitting the corrected GRACE harmonics to the spherical caps, we get a coefficient for each cap, which allows us to evaluate the regional time-series. In contrast to using uniform mascons, we optimize the size and position of the spherical caps for the Totten/Moscow drainage basin. The size of a spherical cap is a compromise between the desired spatial resolution and the minimization of leakage and measurement errors. The noisy higher degree harmonics tend to increase the measurement error as the size of the caps decreases. Where we have a large signal-to-noise ratio, e.g. in areas of large mass loss in the lower reaches of Totten Glacier, we select smaller caps since the signal will not be masked by higher noise levels. With variable sized caps, we minimize the ringing that results from the truncation of the spherical harmonics (e.g. Swenson and Wahr [2002]). To avoid the resulting leakage, both the size and position of the caps need to be optimized. To have truly orthogonal caps in the harmonic domain, the sensitivity kernel described in Jacob et al. [2012] needs to be 1 inside and 0 outside the cap. To optimize the spherical cap basis at a sub-basin level, we place smaller caps on regions of fast change, minimize the gap between the spherical caps, and position the caps to have more or less uniform change inside each cap. To do this, a 3-layer hexagonal grid is used to inscribe caps of diameters 2.7°, 2.9°,

and 3.2°. The sizes are experimentally determined to take advantage of the signal to noise ratio where there is large mass change while maintaining reasonable errors. The geometry of the caps is optimized to avoid leakage into or out of the Totten/Moscow glacier basin. The spherical cap configuration is shown in panel (a) in Figure 2.1.

We follow the procedure of Velicogna and Wahr [2013] to calculate the leakage error for a given area of interest. We divide a synthetic field spatially into individual mascons, convert them to harmonics, and perform a least-square regression with the spherical caps to see how much signal is recovered. We perform the test in two ways: 1) fit each individual synthetic mascon separately to see how much signal is recovered; and 2) fit all other mascons to see how much signal leaks into the mascon of interest. We take the larger value as our leakage error. For the synthetic field, we use SMB values from the RACMO2.3 regional climate model [Van Wessem et al., 2014], and dynamic losses linearly spread as a function of speed and thickness [Rignot et al., 2011b]. To quantify the land/ocean leakage, we scale the sea level fingerprint of the sub-region of interest [Hsu and Velicogna, 2017, Farrell and Clark, 1976] with our GRACE-derived mass change and assume a 100% error in the leakage as a conservative estimate. Note that the GRACE harmonics have atmospheric and oceanic components removed from them [Swenson et al., 2008], and as such the non-zero sensitivity kernel [Jacob et al., 2012] of the mascons over the ocean does not contribute significantly to our estimates. We quantify the ocean-to-land leakage by fitting the GRACE-derived ocean signal coefficients (representing ocean bottom pressure) to our mascons and assume 100% error in the signal [Velicogna and Wahr, 2013]. We also use monthly ocean bottom pressure from the Estimating the Circulation and Climate of the Ocean (ECCO) [Wunsch et al., 2009] model, convert them to harmonics of degree and order 60 and fit them to our Totten mascons. Taking the difference between the ECCO and GRACE-derived ocean leakages as an error estimate decreases the total error in mass loss by 0.1 Gt/yr. We use the largest of the two error estimates, i.e. we assume the leakage error is as large as the correction.

Mass Budget Method: To compare our estimates with independent data, we use the MBM estimates from Li et al. [2016] for Totten, where the total mass balance is SMB minus the grounding line ice flux. For Moscow University, we employ a similar approach, calculating mass fluxes from 1989 to present using ice motion measurements from various satellite data with ice thickness data from Operation IceBridge. We use SMB data from RACMO2.3 [Van Wessem et al., 2014] and MAR3.6.4 [Gallée et al., 2013] extending from January 1979 to December 2015. Cumulative SMB is calculated over the drainage area using a reference period of January 1979 to December 2008 [Shepherd et al., 2012]. Total mass is calculated as the difference between cumulative SMB and cumulative discharge. The choice of the reference period does not affect the MBM results because the same value is subtracted from both the anomalies in surface mass balance and discharge. SMB errors are calculated assuming a 6.1% error in monthly values as in [Li et al., 2016]. Ice discharge errors are calculated as fixed rates from the sum of percentage errors in thickness and speed, scaled by the long-term flux [Li et al., 2016]. The monthly discharge errors are 2.6 Gt/yr and 2.1 Gt/yr for Totten and Moscow University glaciers, respectively, which are added cumulatively in the time-series. The MBM time-series only extends to November 2015.

When comparing the MBM estimates to our sub-basin GRACE results, we integrate SMB values only within the area covered by the mascons of interest to have comparable quantities. Grounding line flux anomalies are calculated with respect to the mean discharge of the entire basin for the reference period. We assume that most of the areas outside of the sensitivity kernel are not contributing to dynamic thinning of the glacier, in accordance with altimetry studies which show ice thinning only at low elevation, along fast-moving portion of the glaciers with ICESat [Khazendar et al., 2013, Pritchard et al., 2009] and Cryosat-2 [McMillan et al., 2014]. We also calculate than the average ice velocity of the glaciers over the sub-basins of interest is about 14 times larger than for the rest of the basin.

2.3 Results

While the resolution and signal-to-noise ratio of GRACE data do not allow time-series to be extracted from single caps, the most optimal sensitivity kernels are found for the triple-cap configurations 1-6-7 and 1-5-7 (see cap numbers in Figure 2.1). Both of these configurations pick up signal from the nearby Moscow University as well, especially 1-6-7. By examining the sensitivity kernels with respect to the drainage basins, we conclude that while 1-5-7 is more concentrated on Totten itself, it picks up a fraction of the signal from Moscow University, which makes the results more difficult to interpret. Therefore, we pick 1-6-7 for the rest of the sub-basin analysis and consider both Totten and Moscow University glaciers together. The sensitivity kernel of this configuration superimposed on top of drainage Cp-D and ice velocity (see Rignot et al. [2011b], Rignot et al. [2017]) is shown in Fig 1b.

We compare the optimized GRACE time-series with the MBM estimates over the sub-region defined by our caps (Fig. 1b and 2a). The monthly GRACE error is 33 Gt for the three caps combined. The annual MBM error is 6 Gt/yr Li et al. [2016], which translates into a monthly error of 21 Gt. The annual MBM error does not change significantly with time during the study period. The AW13 and W12a time-series produce slightly more negative trends that IJ05, but the difference is within errors. The results range from 14.8±4.3 Gt/yr to 17.7±4.1Gt/yr for the period April 2002 to November 2015. More important, the GRACE time-series are in excellent agreement with the MBM time-series obtained with RACMO2.3 at 15.8±2 Gt/yr. The MBM time series using MAR3.6.4 shows a smaller trend of 6.6±2 Gt/yr (Table 2.1). Note that we include the autocorrelation of the residuals when calculating the regression error. The sub-basin estimates are focused in areas with the stronger signal, allowing for smaller mascons.

Farther inland, we experience more leakage from the surrounding areas and get a noisier signal. We compare the MBM trends for the entire drainage basins vs the sub-basin area

sampled by caps 1-6-7 to evaluate the proportion of the mass change that is sampled by our sub-basin configuration. Using RACMO2.3 and MAR3.6.4, we find that we recover about 81.0±2.6% and 70.7±4.4% of the Totten basin, respectively, and 68.7±3.1% and 64.1±6.0% of the Moscow University basin, respectively. The basin-wide estimates for the Totten and Moscow University glaciers are obtained by adding up mascons 1,2,4,6,7,129,130, and 131. As expected, this time-series has larger errors, with estimates ranging from 17.4±6.1 Gt/yr to 18.7±6.4 Gt/yr. The basin-wide MBM trend obtained from RACMO2.3 at 20.6±3 Gt/yr is in good agreement with the GRACE estimates, although the trend obtained from MAR3.6.4 (9.5±2 Gt/yr) is also within uncertainty for the AW13 and W12a GIA model estimates (Table 2.1 and Figure 2.3).

For the period April 2002 to August 2016, we consider a linear model based on the Akaike information criterion (AIC) Burnham and Anderson [2004] with annual and semi-annual components. We obtain a trend in mass loss of 18.5±6.6 Gt/yr using IJ05 GIA for the entire Totten and Moscow University basins. For the sub-basin, the trend is 14.6±4.1 Gt/yr. We take into account the autocorrelation of the residuals with an AR1 model for the residuals, which gives us an autocorrelation coefficient of 0.08±0.04. The error in the autocorrelation coefficient is found by a bootstrapping method where random Gaussian errors with a standard deviation equal to the satellite measurement error are introduced into the time-series and the spread in coefficient was found within 50 iterations. The trends and the associated errors obtained from the optimized spherical cap solutions for the sub-basin and basin-wide estimates are outlined in Table 2.1.

2.4 Discussion

Our results indicate a remarkable agreement at the 5% level between the optimized GRACE time-series using IJ05 GIA and the MBM time-series with RACMO2.3 at a sub-basin scale.

The trends for the period April 2002 to November 2015, as reported in Table 2.1, with all GIA models, are within error of the MBM trend obtained using RACMO2.3. The results obtained from AW13 and W12a in the Totten and Moscow University drainage basins are also in agreement, although slightly more negative than for the IJ05 time-series. While all estimates agree within error, IJ05 display the best agreement with the MBM estimates using RACMO2.3.

The MBM estimates obtained with MAR3.6.4 underestimate the mass loss in these two drainage basins, with the sub-basin trends falling outside of uncertainty bounds. Given that the same reference mean is subtracted from the surface mass balance and discharge time-series in the calculation of cumulative anomalies, we attribute the difference between the MBM time series to a low-bias in MBM/MAR3.6.4 cumulative ice loss in this region. Spatial differences in trend between the two SMB models (Figure 2.4) reveal that MAR3.6.4 shows less negative trends in cumulative surface mass balance close to the grounding line. The same conclusion may not apply to other basins.

The basin-wide estimates of mass change have a larger leakage error from the surrounding areas than the sub-basin estimates. The GIA uncertainty increases as we include more interior regions in the estimate. The IJ05 GIA error increases from 0.87 Gt/yr for the sub-basin estimate to 3.13 Gt/yr for the basin-wide estimate, or 360%. The drainage-basin estimates are still in agreement with the MBM estimates. For the common period between April 2002 to November 2015, the GRACE estimate is a mass loss of 18.6±6.4 Gt/yr using IJ05 GIA versus MBM estimates of 20.6±2.7 Gt/yr and 9.5±2.1 Gt/yr with RACMO2.3 and MAR3.6.4, respectively. While showing smaller losses over the entire drainage, MAR3.6.4 is within error of the AW13 and W12a GRACE time-series.

Few studies have evaluated SMB models in this part of Antarctica. Wang et al. [2016] used in-situ data to evaluate precipitation - evaporation/sublimation from global reanalyses and regional climate models including RACMO2.1 and RACMO2.3, but not MAR3.6.4. They

found that RACMO2.3 shows the best agreement with in-situ measurements over the whole ice-sheet and in particular over the coastal sector Cp-D of the Totten and Moscow University drainage basins, which provides independent support to our findings. Velicogna et al. [2014] reported a good agreement between GRACE and RACMO2.3 cumulative SMB anomalies in the larger Totten-Moscow-Frost area, but the study did not take ice discharge into account and did not evaluate other SMB models. Gallée et al. [2005] evaluated MAR along the Wilkes Land transect in the vicinity of the Totten and Moscow University drainage basins and found discrepancies with in-situ measurements in precipitation and wind transport at different locations.

The use of regionally-optimized variable spherical caps for the processing of GRACE harmonics allows us to reconcile up-to-date estimates of the mass balance of Totten and Moscow University glaciers. Our results suggest a state of negative mass balance, with multiple lines of evidence. With this approach, we evaluate the performance of SMB models and identify a bias in the long-term SMB values from MAR3.6.4. The agreement indirectly provides additional confidence to the MBM results of Li et al. [2016]. Our findings are weakly affected by the uncertainties in the GIA correction. Even for the basin-wide estimates where the GIA errors are larger, the GIA errors do not affect the agreement between GRACE and MBM estimates. We recommend that a similar approach be employed in other basins of Antarctica where the mass balance signal is small and not well constrained by observations. The approach also provides a pathway to evaluate and compare various SMB models.

Our study illustrates that even though the whole-basin estimates are most useful to inform us about the total contribution of each basin to sea level rise, the sub-basin analysis enables a more refined comparison, with lower uncertainties, of various estimates of the mass loss. A comparison at the sub-basin level hence provides more opportunities to interpret differences between models, here caused by a difference in the long-term average SMB between models.

The study demonstrates that the sub-basin approach with optimized spherical caps helps

evaluate mass balance over small areas, with low errors because we focus on the areas with the largest signal. This methodology could be applied to similarly small parts of the ice sheets. More broadly, our approach could be used in geophysics and hydrology, e.g. to evaluate ground water withdrawal more precisely over a small region. Data from the GRACE Follow-On (FO) [Flechtner et al., 2014] mission will likely improve the quality of sub-basin estimates due to the expected lower noise levels of GRACE-FO than with GRACE.

2.5 Conclusions

We use a set of regionally optimized spherical caps to evaluate the mass balance of the Totten and Moscow University glaciers, East Antarctica using GRACE harmonics at the sub-basin and entire basin scales. The spherical cap basis is designed from the signal to noise ratio and the geometry of mass change to extract regional time series with the lowest error. We find a good agreement with the MBM estimates using the RACMO2.3 SMB model, independent of the GIA corrections, whereas the MAR3.6.4 results yield an underestimation of the mass loss in the sub-basin region. MAR3.6.4 is within error for the whole basin with W12a and AW13 GIA corrections, but not with IJ05. For the entire Totten and Moscow University basins, the trend is 18.5±6.6 Gt/yr using IJ05 for the period April 2002 to September 2016. Our results provide reduced uncertainties and higher confidence that the Totten/Moscow sector of East Antarctica has been losing mass relatively rapidly in the last 15 years. We recommend that a similar sub-basin approach using optimized spherical caps be used over other parts of Antarctica where independent mass balance methods must be compared or in Greenland at the regional scale.

Acknowledgments

This work was performed at the UCI and JPL-Caltech. It was supported by the NASA's GRACE and GRACE-FO, Cryosphere, Terrestrial Hydrology, and NSLC programs. Velocity and ice thickness data are available at the National Snow and Ice Data Center (NSIDC), Boulder, CO, as part of the NASA Operation IceBridge project and of MEaSUREs. MAR surface mass balance data can be accessed at `ftp://ftp.climato.be/fettweis/`. CSR RL05 GRACE harmonics are available at `http://www2.csr.utexas.edu/grace/RL05.html`. Data presented in this paper are publicly available at `https://www.ess.uci.edu/~velicogna/totten_moscow_timeseries.php`.

Table 2.1: GRACE trends and corresponding errors obtained for the Totten/Moscow University glaciers and comparison with the MBM estimates at the sub-basin and whole-basin scales. Leakage Error refers only to the mascon-to-mascon leakage error quantified by a synthetic field on land, while Ocean Leakage refers to the full ocean/land leakage determined from GRACE GAD coefficients. GRACE = Gravity Recovery and Climate Experiment; RACMO2.3 = regional atmospheric climate model version 2.3; MBM = mass budget method.

	Trend $[Gt/yr]$	Total Error $[Gt/yr]$	Leakage Error $[Gt/yr]$	Regression Error $[Gt/yr]$	Ocean Leakage $[Gt/yr]$	GIA Error $[Gt/yr]$
Sub-Basin Estimates						
04/2002 - 08/2016						
GRACE (IJ05)	-14.6	4.1	2.9	2.5	0.9	0.9
GRACE (AW13)	-17.2	4.0	2.8	2.5	0.9	0.8
GRACE (W12a)	-17.5	3.9	2.8	2.5	0.9	0.8
04/2002 - 11/2015						
GRACE (IJ05)	-14.8	4.3	3.0	2.7	1.0	0.9
GRACE (AW13)	-17.5	4.2	2.9	2.7	1.0	0.8
GRACE (W12a)	-17.7	4.1	2.8	2.7	1.0	0.8
MBM (MAR3.6.4)	-6.6	1.6				
MBM (RACMO2.3)	-15.8	2.0				
Whole-Basin Estimates						
04/2002 - 08/2016						
GRACE (IJ05)	-18.5	6.6	5.2	2.4	0.5	3.1
GRACE (AW13)	-17.6	6.3	5.0	2.4	0.5	2.8
GRACE (W12a)	-17.3	6.3	4.9	2.4	0.5	3.1
04/2002 - 11/2015						
GRACE (IJ05)	-18.6	6.8	5.3	2.7	0.4	3.1
GRACE (AW13)	-17.7	6.4	5.1	2.7	0.4	2.8
GRACE (W12a)	-17.4	6.4	4.9	2.7	0.4	3.1
MBM (MAR3.6.4)	-9.5	2.1				
MBM (RACMO2.3)	-20.6	2.7				

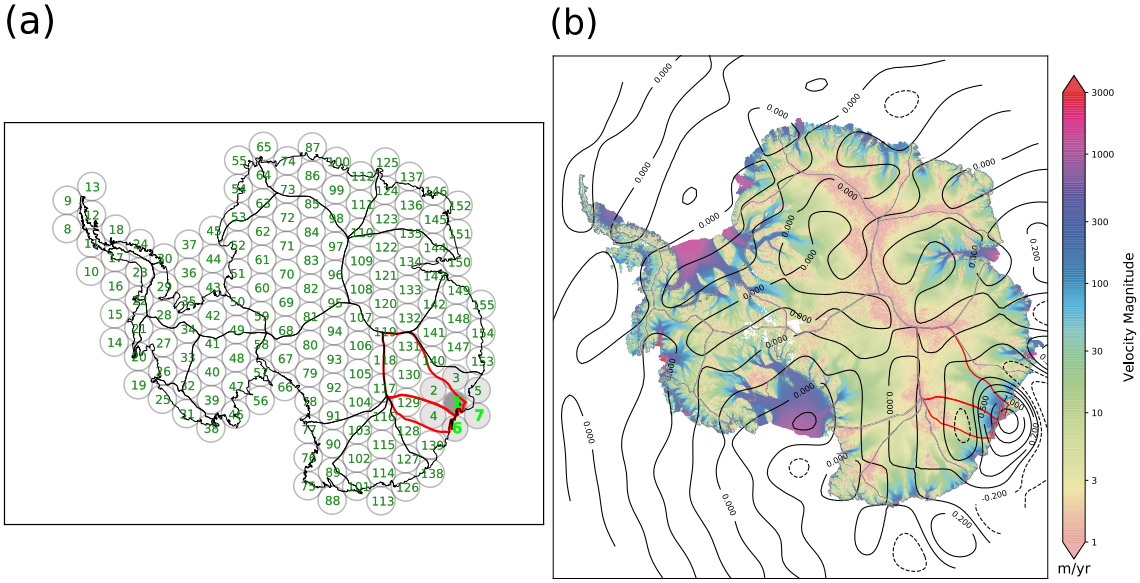

Figure 2.1: **a)** Spherical cap basis used to derive sub-basin regional estimates of the mass balance of Totten and Moscow University glaciers, East Antarctica using GRACE data. Caps are inscribed in a 3-layer hexagonal grid with diameters 2.7° (dark grey), 2.9° (light grey), and 3.2° (white). Black lines show Antarctic drainage basins (see Rignot et al. [2011b]) Red lines show the Totten and Moscow University glacier basins. The caps used for the sub-basin estimates are labelled with bold bright green numbers. **b)** Sensitivity kernel for configuration 1-6-7 superimposed on ice velocity [Rignot et al., 2011b, Mouginot et al., 2012, Rignot et al., 2017]. Grey lines show the major Antarctic drainage basins as in *a*. Black lines show the contour levels of the sensitivity kernel. The zero-contour lines displays small fluctuations in the kernel throughout the ice sheet which result in minimal leakage. EAIS = East Antarctica; GRACE = Gravity Recovery and Climate Experiment.

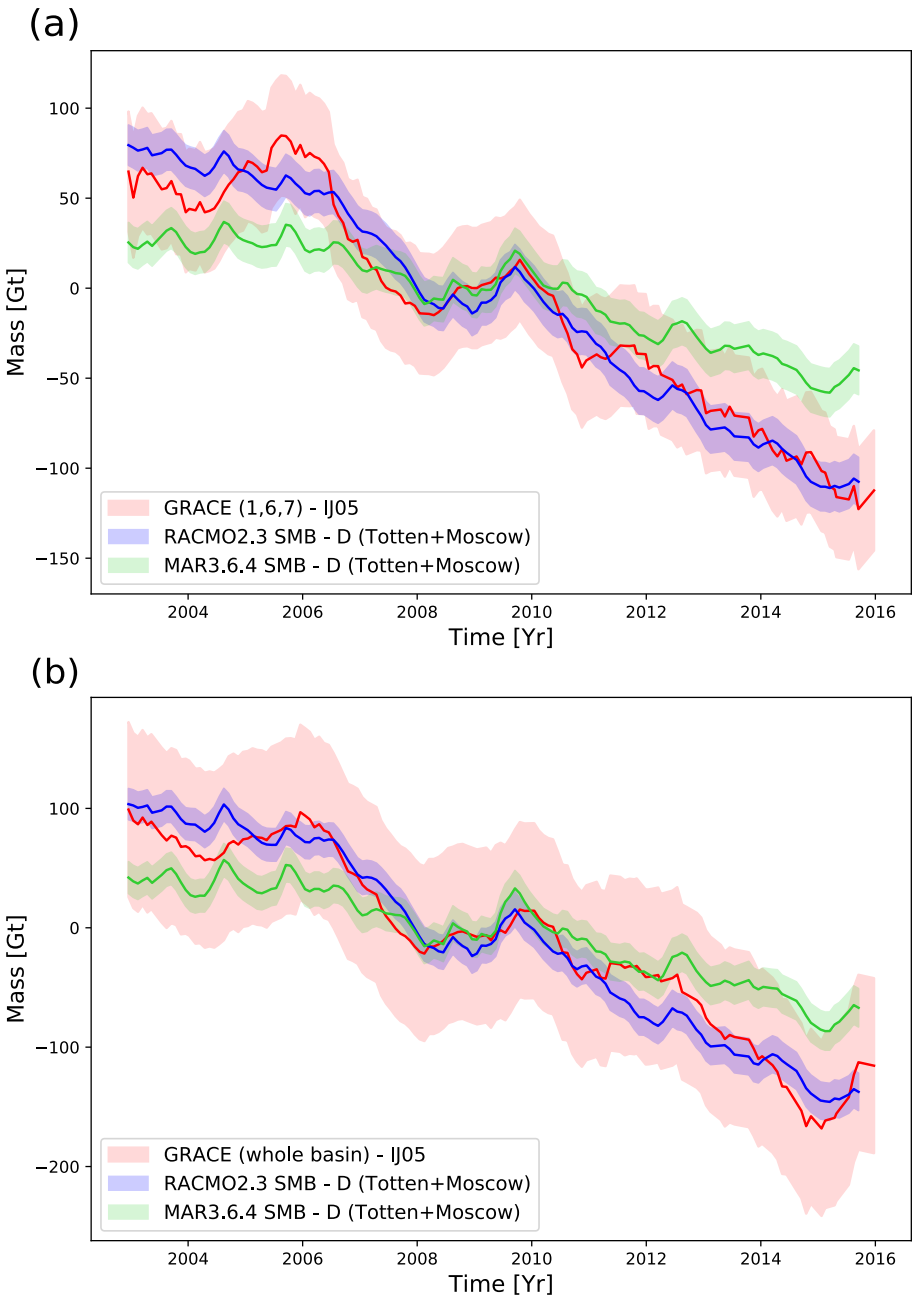

Figure 2.2: Optimized GRACE time-series of the mass (in gigatons = 10^{12} kg) of the Totten and Moscow University glaciers, East Antarctica using IJ05 GIA correction (red) compared with ice discharge subtracted from surface mass balance estimates from RACMO2.3 (blue) and MAR3.6.4 (green) for the **(a)** sub-basin and **(b)** whole-basin configurations. GRACE = Gravity Recovery and Climate Experiment; RACMO2.3 = regional atmospheric climate model version 2.3; GIA = glacial isostatic adjustment.

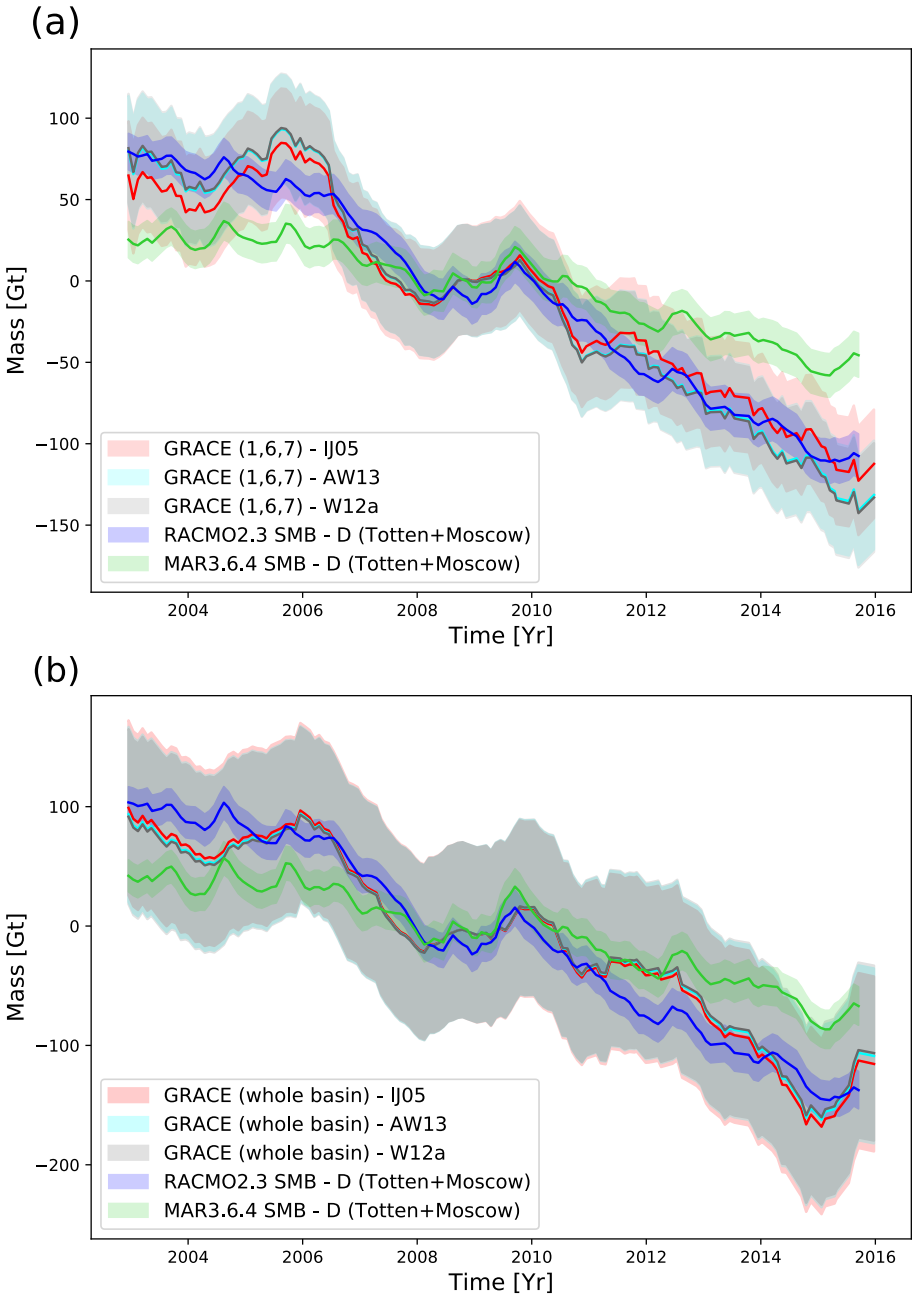

Figure 2.3: Optimized GRACE time-series of the mass (in gigatons = 10^{12} kg) of the Totten and Moscow University glaciers, East Antarctica using IJ05 (red), AW13 (aqua) and W12a (gray) GIA corrections compared with ice discharge subtracted from surface mass balance estimates from RACMO2.3 (blue) and MAR3.6.4 (green) for the **(a)** sub-basin and **(b)** whole-basin configurations.

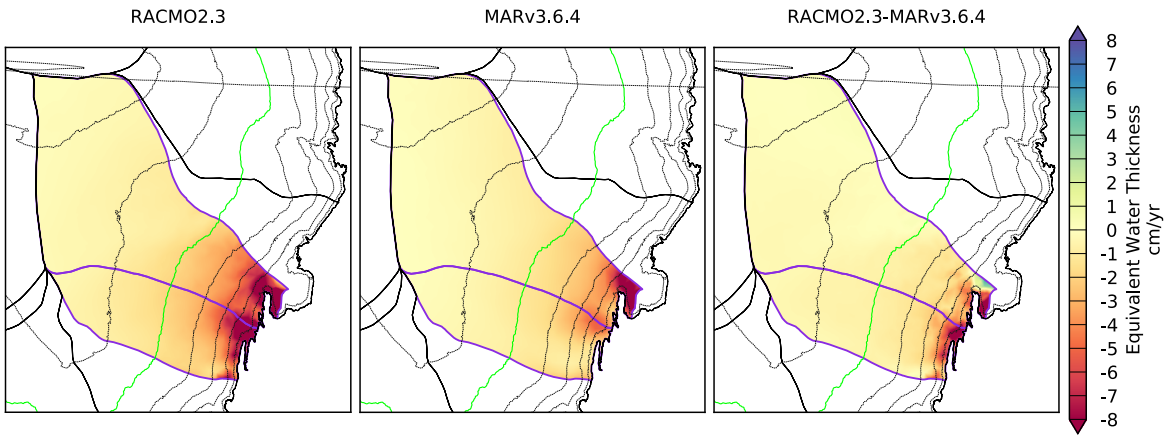

Figure 2.4: Trend in cumulative surface mass balance for RACMO2.3 *(left)*, MAR3.6.4 *(middle)*, and the difference between the two *(right)* from April 2002 to the end of 2015. Basin lines for Totten and Moscow University glaciers are drawn in purple. Elevation contours with 500 m intervals are drawn in black, with the bright green line representing the 2500 m contour. Note trends are negative because cumulative surface mass balance is decreasing over the time period.

Chapter 3

Evaluation of Regional Climate Models using Regionally-Optimized GRACE Mascons in the Amery and Getz ice shelves basins, Antarctica

As Appears in:

Mohajerani, Yara, Isabella Velicogna, and Eric Rignot. "Evaluation of Regional Climate Models using Regionally-Optimized GRACE Mascons in the Amery and Getz ice shelves basins, Antarctica." Geophysical Research Letters. Accepted. doi: 10.1029/2019GL084665.

Abstract

We develop regionally-optimized GRACE solutions to evaluate the mass balance of the drainage basins of Amery Ice Shelf, East Antarctica and Getz Ice Shelf, West Antarctica. We find that the Amery region is near-balance, while the Getz region is rapidly losing mass. We compare the results with the Mass Budget Method (MBM) combining ice discharge along the periphery with surface mass balance derived from three regional climate models: 1) Regional Atmospheric Climate Model (RACMO) 2.3p1 and 2) 2.3p2, and 3) Modèle Atmosphérique Régional 3.6.41. For Amery, MBM/RACMO2.3p1 agrees with GRACE while MBM/RACMO2.3p2 and MBM/MAR3.6.41 suggest a positive mass balance. For Getz, all estimates agree with a mass loss and the GRACE results are robust to uncertainties in Glacial Isostatic Adjustment (GIA) derived from an ensemble 128,000 forward models. Over the period 04/2002-11/2015, the mass loss of the Getz drainage basin is 22.9±10.9 Gt/yr with an acceleration of 1.6±0.9 Gt/yr^2.

Plain Language Summary

We use a regional optimization methodology for processing data from the Gravity Recovery and Climate Experiment (GRACE) to evaluate the ice mass change of the drainage basins of two major ice shelves in Antarctica and evaluate the performance of Regional Climate Models (RCMs). The Getz Ice Shelf basin in West Antarctica has shown previous disagreements between various mass balance estimates and is influenced by heterogenous conditions that make it vulnerable and challenging to study. We find this region to be in a state of accelerating mass loss. Furthermore, all three examined RCMs are in good agreement with GRACE in this region. The Amery Ice Shelf in East Antarctica is the third largest Antarctic ice shelf with a basin that has enough ice to raise sea level by 7.8 meters, but has presented

challenges in previous mass balance efforts. We find the mass in this drainage basin is not changing significantly. Furthermore, only one out of the three examined RCMs agrees with GRACE observations in this region. These results suggest that the RCMs may need to be revisited in some regions of the ice sheet.

3.1 Introduction

The Antarctic ice sheet has been losing mass at an average rate of 109±56 Gt/yr from 1992 to 2017, equivalent to 7.6±3.9 mm of sea level rise [Shepherd et al., 2018]. During that time period, the mass loss has been accelerating [Velicogna et al., 2014, Rignot et al., 2019]. The evaluation of ice sheet mass balance has been primarily achieved using a combination of three techniques: 1. gravimetric estimates from the GRACE (Gravity Recovery and Climate Experiment) mission [Velicogna et al., 2014, Sasgen et al., 2013, Velicogna and Wahr, 2006]; 2. volume changes estimated from a series of altimeter measurements [Pritchard et al., 2012, McMillan et al., 2014, Sutterley et al., 2018]; and 3. Mass Budget Method (MBM) combining ice discharge along the periphery with Surface Mass Balance (SMB) reconstructed by regional climate models (RCMs) in the interior [Rignot et al., 2008, 2019]. While there is reasonable agreement between these large-scale estimates in West Antarctica [Shepherd et al., 2018, 2012], differences exist in East Antarctica. For instance, Shepherd et al. [2018] finds a standard deviation of 37 Gt/yr across the various mass balance estimates for East Antarctica. Moreover, regional differences between mass balance estimates have not been fully evaluated around Antarctica. Differences in RCMs affect not only the confidence on mass budget and altimetry estimates, with the latter due to firn compaction models forced by RCMs [Shepherd et al., 2012], but also impact the estimation of the partitioning in mass loss between SMB processes and ice dynamics for all techniques.

In a prior study, Mohajerani et al. [2018] used a regional optimization approach for GRACE

to calculate the mass balance of Totten and Moscow University glaciers at the basin and sub-basin scales and evaluate different RCMs. Here, we extend the methodology to two major drainage systems in Antarctica. First, we examine the drainage basin feeding into the Amery Ice Shelf, which includes three major glaciers: Fisher, Lambert, Mellor, and two large sectors on the flanks of Amery Ice Shelf: MacRobertson Land and American HighLand. Amery is the third largest ice shelf in area in Antarctica [Pittard et al., 2017]. Here we are interested in the mass balance of the drainage basin of the Amery Ice Shelf, which holds enough ice to raise sea level by 7.8 m [Rignot et al., 2019]. At present, the basin appears to be in balance based on the mass budget method [Rignot et al., 2019]. This region has presented challenges in past studies caused by differences in the estimation of the position of the grounding line. While some studies place it north of the 35 km Minimum Ice Shelf Width (MISW) [Winkelmann et al., 2012, Golledge et al., 2015], others placing it to the south [DeConto and Pollard, 2016]. Such differences result in major uncertainties in the mass balance of the Amery drainage basin.

Second is the drainage basin of the Getz Ice Shelf, which, according to the MBM, tripled its mass loss in 2017 compared to the 1979-2013 average, from 5 Gt/yr to 16.5 Gt/yr, for a cumulative contribution of 1 mm to sea level rise from 1979 to 2017 [Rignot et al., 2019]. Most of the glaciers feeding into Getz Ice Shelf have no name and are labeled using a latitude-longitude convention [Rignot et al., 2019]. The ice shelf, which has a strong effect on the mass balance of the drainage basin due to its buttressing effect [Dupont and Alley, 2005], is located at a critical position in the Pacific-Antarctic coastline and strongly affected by decadal Pacific Oscillations [Jacobs et al., 2013]. Spatial heterogeneity due to different oceanic regimes to the west and east of the ice self, as well as the complex bathymetry of the region make the analysis of the ice shelf evolution difficult [Jacobs et al., 2013], which in turns introduces uncertainty in the long-term mass balance of the drainage basin. In addition, previous assessments of the mass balance of the drainage basin have suggested major disagreements between GRACE and MBM estimates. For example, Sasgen et al.

[2010] found that the GRACE estimate for the Getz Ice Shelf and Pine Island Glacier basins were 26 Gt/yr lower than the MBM estimate. This discrepancy could not be accounted for by the choice of the Glacial Isostatic Adjustment (GIA), or leakage from the atmosphere, ocean, or changes in other basins. The authors attributed it to an anomalous mass gain that took place during the GRACE period (August 2002 - August 2008) that was not included in their MBM estimate from 1980-2004, or possible errors in ice thickness along the grounding line. More recently, Chuter et al. [2017] used ice thickness values derived from Cryosat-2 to reassess the mass budget of Getz and deduced a near mass balance of 5±17 Gt/yr for 2006 to 2008. This estimate is within one standard deviation of prior radar altimetry estimates [Shepherd et al., 2012] but far more positive than prior estimates. The authors attributed this difference to a 9 m positive bias in elevation near the grounding line in the ERS-1 digital elevation model [Griggs and Bamber, 2011]. The most recent MBM estimates from this area are however based on actual thickness data, not on hydrostatic equilibrium [Rignot et al., 2019]. In this study, we compare the mass balance estimates from GRACE and MBM using various RCMs to establish a greater level of confidence in the results, evaluate different RCMs, and resolve uncertainties from prior studies. We conclude on the mass loss of these major sectors and on the evaluation of RCMs.

3.2 Data and Methodology

We use three RCMs: 1) Regional Atmospheric Climate Model version 2.3p1 (RACMO2.3p1) [Van Wessem et al., 2014], 2) version 2.3p2 (RACMO2.3p2) [van Wessem et al., 2018], and 3) Modèle Atmosphérique Régional version 3.6.41 (MAR3.6.41) [Agosta et al., 2019]. RACMO2, developed by the Institute for Marine and Atmospheric Research Utrecht (IMAU) at Utrecht University, uses the physics package of the Integrated Forecast System (IFS) of the European Centre for Medium-Range Weather Forecasts (ECMWF) along with the

HIRLAM (High Resolution Limited Area Model) [Undén et al., 2002] dynamics to model SMB [Van Wessem et al., 2014] at 27 km resolution. RACMO2.3p2 provides several updates to part 1, including improved topography, precipitation, and snow properties [van Wessem et al., 2018]. RACMO2.3p1 is available from 1979 to 2015. RACMO2.3p2 is available from 1979 to 2016. MAR3.6.41 is a coupled surface-atmosphere regional climate model that uses the SISVAT surface scheme (Soil Ice Snow Vegetation Atmosphere Transfer) [De Ridder and Gallée, 1998], which uses the CROCUS snow model [Brun et al., 1992]. The model estimates SMB at a spatial resolution of 35 km for 1979 to 2017 [Agosta et al., 2019]. We use the version of the model forced by the ECMWF ERA-Interim reanalysis [Dee et al., 2011] at the boundary to be consistent with RACMO2 [Agosta et al., 2019, Van Wessem et al., 2014]. While the choice of the forcing reanalysis product introduces additional uncertainty, here we are interested in how the RCM parameterizations and processes diverge under the same forcing at the boundary.

To calculate MBM with each RCM, we interpolate the SMB fields to a 1km×1km polar stereographic grid and integrate the monthly values within each basin. Ice discharge is from Rignot et al. [2019] with the following errors: 3.6 Gt/yr for Amery and 4.8 Gt/yr for Getz. The regional SMB uncertainty is also from Rignot et al. [2019]. The SMB and discharge time-series are added up cumulatively, and the difference of the cumulative time-series provides the total mass budget. By subtracting total cumulative discharge from SMB, we eliminate the reliance on calculating anomalies with respect to a chosen reference period, i.e. the calculation of total mass budget numbers does not depend on the choice of a reference period. Only the SMB and discharge anomalies depend on a reference period, not the total mass budget. Finally, a rate-of-change time-series is calculated by using a 36-month sliding window as described in the Supporting Information.

For each region, we get gravimetric estimates from GRACE [Tapley et al., 2004] for 2002 to 2017. We use RL06 Level-2 spherical harmonic coefficients from the Center for Space

Research (CSR) at the University of Texas [Bettadpur, 2018] for the period April 2002 to August 2016. The $C_{2,0}$ coefficients, representing the oblateness of the geoid, are replaced with Satellite Laser Ranging coefficients [Cheng et al., 2013]. Furthermore, in order to recover degree-1 terms representing geocenter translations not measured by GRACE in the gravitational frame of reference, we follow the methodology of the improved geocenter solution by Sutterley and Velicogna [2019], using the same corrections applied to the GRACE harmonics used in the spherical cap mascon calculation, outlined below, for consistency. The Sutterley and Velicogna [2019] solution uses an iterative method to calculate geocenter terms with the effects of self-attraction and loading. The Max-Planck-Institute for Meteorology Ocean Model (MPIOM) [Jungclaus et al., 2013] harmonics provided as part of the RL06 data release are used in combination with the GRACE mass change coefficients on land to iteratively solve for geocenter terms. The GRACE coefficients are de-striped following Swenson and Wahr [2006], smoothed with a 300-km radius Gaussian smoothing kernel [Wahr et al., 1998], and corrected with the A et al. [2013] GIA model for the geocenter calculation.

To ensure that our results are robust with respect to the GIA correction, we use the GIA statistics provided by Caron et al. [2018], which uses regional constraints and variations of ice history and earth structure through 128,000 forward modeling runs to provide a probability distribution function from which the expectation value of present-day GIA and the full covariance matrix associated with the errors are derived. Using a probability distribution function as opposed to a single GIA product allows us to assess the robustness of our results with regards to the GIA correction. We assess the GIA error using the full covariance matrix following Wahr et al. [2006]. The GIA probability distribution samples a wide range of upper and lower mantle viscosities, lithosphere thicknesses, and ice history through separate scaling factors for Antarctic, Greenland, Laurentide, Cordilleran, and Fennoscandian ice sheets. The resulting covariance matrix from the Bayesian treatment of the ensemble of forward models provides larger uncertainty bounds than previous reports [Caron et al., 2018], allowing a conservative estimate of the role of GIA in the GRACE estimate.

To produce regionally-optimized estimates of mass balance from Level-2 GRACE harmonics we use the least-squares mascon approach, which uses variable-sized spherical caps described in Mohajerani et al. [2018]. This procedure generates a set of regionally configured spherical caps based on the characteristics of the local mass change to calculate localized mass balance estimates from the GRACE harmonics. The caps are organized to sample roughly uniform distributions of mass. The design allows the sum of the designated mascons to capture the mass change only within the area of interest with minimal leakage from outside regions that exhibit significant mass change. A smaller size allows each cap to sample a more uniform region and refine the spatial extent of the area being sampled. However, smaller caps are more heavily influenced by noisier higher degree (shorter wavelength) harmonics [Wahr et al., 2006]. Therefore, a higher mass change signal in the area of interest allows the use of slightly smaller caps without being dominated by noise. GRACE stokes coefficients are regressed against these regionally defined spherical caps with uniform and unitary mass using a simultaneous least-squares fit to calculate weights for each mascon [Jacob et al., 2012, Velicogna et al., 2014, Sutterley et al., 2014]. For the areas of interest, multi-layer hexagonal grids with different resolutions are used to create the spherical caps. In the Amery region, the caps range from 2.7° to 3.2° in diameter. Our study area focuses on the sub-basin region spanning the Fisher, Lambert, Mellor, American HighLand, and MacRobertson Land basins. The basins are defined according to [Rignot et al., 2019]. The sampled area is shown by caps 1,5,7 in the inset of Figure 3.1a. In the Getz region, the diameters range from 2.6° to 3.0°. Our study region is the drainage basin of the Getz Ice Shelf, and also covers some of the smaller neighboring regions of Hull, Land, Frostman, Lord, Shuman, Anandakrishnan, and Jackson-Perkins. The sampled area is shown by caps 1 and 2 in the inset of Figure 3.1b. The SMB under the kernel from these regions and the corresponding grounding line discharge are also included in our MBM estimate for the Getz region. The total discharge error for the region is 4.9 Gt/yr by adding regional errors from Rignot et al. [2019] in quadrature.

The sensitivity kernel of the mascon configuration [Jacob et al., 2012] shows that the signal

is being captured by the mascons of interest in each configuration (Figure 3.1). Ideally, the kernel should have a value of 1 over the regions of interest and 0 elsewhere. The configurations focus on the areas of high ice velocity within each basin, or highest mass loss, with minimal uncertainty. In each region, the sensitivity kernel captures the areas of highest change and has minimal leakage elsewhere. Furthermore, by showing where the signal is being sampled, the kernel in Figure 3.1 illustrates that there are no effects from the small gaps between the spherical caps due to the tails of the truncated harmonics extending beyond the exact boundaries of the caps [Swenson and Wahr, 2002]. While most of the ringing is diverted to the ocean where the mass change signal is smaller, there are small variations of the kernel around the zero contour throughout the ice sheet, yet both the land/ocean leakage and the leakage from other basins are fully quantified, as outlined below.

The land/ocean leakage is calculated in two ways. First, the sea level fingerprint of the region of interest [Hsu and Velicogna, 2017] is scaled by the total mass change derived from GRACE. This calculation produces an estimate of the contribution from land to ocean, which is used to adjust the mass loss trend. We assume a conservative error of 100% in the error budget for this correction. In addition, we take into account the contribution of the ocean signal that leaks into the mascons of interest. While the sensitivity kernels in Figure 3.1 have ringing over the ocean, the atmospheric and oceanic components are removed from the GRACE GSM harmonics and therefore there is minimal signal in these areas. As a conservative estimate, we use the total ocean signal provided by the GRACE ocean (GAD) harmonics, which correspond to the MPIOM ocean model [Jungclaus et al., 2013] to calculate the ocean leakage error. This is accomplished by fitting the GAD coefficients to the mascons of interest and calculating the trend and acceleration of this leakage signal. The mascon-to-mascon leakage on the ice sheet is taken into account in the error budget. We use a synthetic mass budget field derived from modeled SMB and linearly-distributed dynamic loss as a function of ice thickness and speed following Rignot et al. [2011b]. The synthetic field is divided up between the spherical caps for each configuration and converted to harmonics.

The leakage is calculated by fitting the synthetic harmonics derived from each spherical cap to the mascons and quantifying the recovered signal for each cap. The leakage is calculated using two distinct measures: 1) "island leakage", which refers to how much signal leaks *outward* from a mascon of interest to other mascons, and 2) "hole leakage", which refers to how much signal leaks *inward* from other regions to the mascon of interest. This is similar to the leakage calculation in Mohajerani et al. [2018] with a few important updates: instead of taking the maximum value between the "island" and "hole" leakages as the total leakage, we calculate the difference between the two. This approach produces a better assessment of the overall effect of leakage in the regions of interest. While taking the differences reduces the leakage value in some cases, it may also increase it if the two leakage solutions have opposite signs. The other change in the leakage calculation is to use an updated synthetic field with discharge values from Rignot et al. [2019] and RACMO2.3 p1 and p2 SMB values. The total mass budget synthetic field is calculated by spreading the total discharge value in each basin as a function of the flux density calculated from ice speed and ice thickness. The ice speed is obtained from the MEaSUREs ice velocity data [Rignot et al., 2017] and ice thickness is from Bedmap2 [Fretwell et al., 2013]. We use the total mass budget as the synthetic field instead of taking the maximum leakage obtained from SMB-only and MBM fields, which provides a more accurate leakage estimate with a more realistic synthetic field.

The interpolated SMB values are integrated within the kernel to produce analogous estimates to the GRACE measurements. We use a threshold of 5% in how much signal is captured by the kernel to construct polygons around the regions of interest for the integration. In other words, anything that is captured by GRACE at the 0.95 level will be present in the MBM integration. This threshold reduces the effect of small fluctuations near zero in the kernel field. However, because the mascons are designed around the areas of high mass change, the low values of the kernel are in regions of smaller change and thus the value of the threshold does not have a significant impact on the results.

3.3 Results

Figure 3.1 shows the time-series of mass change, dM/dt, of the regionally-optimized GRACE solutions and the corresponding mascon configuration and sensitivity kernels, and the MBM time-series derived from RACMO2.3p1, RACMO2.3p2, and MAR3.6.41 for Amery and Getz. The GRACE trend errors are calculated using the leakage, regression, GIA, and ocean leakage errors as described in the previous section. The corresponding errors for the MBM time-series are calculated from the regression error combined with the SMB and discharge errors outlined in the previous section. The full breakdown of the trend errors is in Table 3.1. For each region, we calculate a trend and acceleration according to the Bayesian Information Criterion (BIC) [Burnham and Anderson, 2004]. For Amery, the GRACE estimate indicates near balance, with a linear trend of 1.8±5.0 Gt/yr. The MBM estimate using RACMO2.3p1 agrees with the GRACE estimate within -0.4±2.7 Gt/yr. While the GRACE and MBM/RACMO2.3p1 estimates are statistically in near-balance, the MBM/RACMO2.3p2 and MBM/MAR3.6.41 exhibit statistically significant positive trends. Table 3.1 lists all trends for the common period of April 2002 to November 2015.

In contrast to Amery, none of the RCMs show a bias with respect to GRACE in the Getz region. As shown in panel (b) of Figure 3.1, the GRACE and MBM time-series are in excellent agreement. As outlined in Table 3.1 the GRACE estimate yields a loss of 22.9±10.9 Gt/yr. The GRACE errors are larger in this area as a result of a larger leakage error. The leakage error poses a special challenge in this small sub-basin region given that it is adjacent to the highest mass loss of the entire ice sheet recorded in the Amundsen Sea Embayment sector of West Antarctica [Velicogna et al., 2014]. The corresponding MBM mass loss estimates are 23.7±6.2 Gt/yr, 23.8±6.3 Gt/yr, and 25.4±6.3 Gt/yr for MAR3.6.41, RACMO2.3p1, and RACMO2.3p2 models, respectively, which are in excellent agreement with GRACE. The close agreement between estimates provide confidence in the mass balance assessment using these independent methods. This area also exhibits an acceleration in

mass loss. Table 3.1 outlines the acceleration and corresponding error for regions where a quadratic regression model is applicable. This is analogous to Table 3.1, excluding the GIA errors, which do not affect the acceleration since the GIA correction is a constant signal. We find an acceleration in mass loss of 1.6±0.9 Gt/yr^2 with GRACE, in agreement with the acceleration of 2.0±0.2 Gt/yr^2 from MBM.

3.4 Discussion

Our regionally-optimized GRACE estimates indicate that the Amery region is near balance, which confirms Rignot et al. [2019] using the MBM/RACMO2.3p1. This is also in agreement with previous in-situ measurements. Wen et al. [2007] used a combination of remote-sensing and in-situ data to find a near-balance mass budget of -2.6±6.5 Gt/yr for Lambert, Mellor, and Fisher glaciers. Similarly, Wen et al. [2014] found these glaciers to be in balance within 2.9±3.6 Gt/yr by combining SMB from RACMO2.1 with discharge derived from interferometric synthetic-aperture radar (InSAR)-derived ice velocity and BEDMAP [Lythe and Vaughan, 2001] and PCMEGA (Prince Charles Mountains Expedition of Germany and Australia) [Damm, 2007] derived ice thickness, which is in agreement with MBM/RACMO2.3p1. In contrast, Yu et al. [2010] found a significantly more positive trend of 22.9±4.4 Gt/yr for the grounded portion of the Amery Ice Shelf system by utilizing ICESat and InSAR with a refined grounding line position derived from SAR and MODIS data. However, our findings suggest that this result overestimates mass gain in the region, which may reflect the quality of the SMB model in Vaughan et al. [1999]. The RACMO model used by Wen et al. [2014] has lower accumulation levels in the Lambert region compared to that in Vaughan et al. [1999].

In the Getz area, GRACE yields a mass loss of 22.9±10.9 Gt/yr and acceleration of 1.6±0.9 Gt/yr^2, within errors of the mass loss of 16.5 Gt/yr in 2017 from Rignot et al. [2019]. Our

estimate agrees with radar altimetry results from McMillan et al. [2014] (22±3Gt/yr for 2010-2013) and GRACE from King et al. [2012] (23±3Gt/yr for the larger drainage basin in 2002-2010). Previous MBM estimates using ice thickness from Cryosat-2 [Chuter et al., 2017] however yielded a positive trend of 5±17Gt/yr, which does not agree with GRACE despite the large uncertainty bound. Our MBM trends, all in excellent agreement with GRACE, do not confirm this positive estimate, which implies that the Cryosat-2 derived thicknesses were probably too low, which is probably a result of uncertainties in firn depth correction. Similarly, the gravimetric estimate of Bouman et al. [2014] yields a significantly larger loss of 55±9 Gt/yr from November 2009 to June 2012 by combining GRACE with GOCE (Gravity Field and Steady-State Ocean Circulation Explorer) [Visser et al., 2002]. The agreement between our independent GRACE and MBM estimates suggest that this earlier estimate of the mass loss is too high. Furthermore, with the regionally-optimized mascon approach, we successfully isolated the mass balance of the Getz drainage basin with a mascon-to-mascon leakage error that is only 45% of the total signal (Table 3.1). Considering the proximity of this region to the high mass change signal of Amundsen Sea Sector glaciers, we conclude that this demonstrates the practicality of our approach at the sub-basin scale in Antarctica.

In the Amery region, we find that MBM/RACMO2.3p1 is in agreement with GRACE, while MBM/RACMO2.3p2 and MBM/MAR3.6.41 produce trends that are too positive. This result is consistent with those of Mohajerani et al. [2018] on Totten and Moscow University glaciers in East Antarctica (Figure A1). Given that all mass budget estimates in a given region share the same discharge values, the differences must be attributed to the SMB models. As outlined in Section 3.2, the cumulative time-series are calculated by integrating the total monthly SMB and discharge values through time. As a result, different trends in the MBM time-series must be attributed to either disagreeing temporal variability or differences in mean SMB across models. The monthly SMB time-series do not exhibit statistically significant trends in any of the regions. However, there are considerable differences in the mean magnitude of monthly SMB time-series, as outlined in Table A1 Larger monthly magnitudes

lead to faster cumulative growth compared to the cumulative discharge time-series, resulting in a more positive MBM time-series. It is important to emphasize that this result does not depend on a reference period since the mass balance is simply the difference between absolute SMB and absolute discharge.

In the Amery region, where MBM/RACMO2.3p2 and MBM/MAR3.6.41 do not agree with GRACE, the mean SMB values appear to be more than 10 Gt/yr larger compared to RACMO2.3p1, yielding a more positive MBM trend consistent with Table 3.1. In the Getz area, the mean SMB values are in better agreement across all models, consistent with the agreement between MBM estimates and GRACE in Figure 3.1 and Table 3.1. Given that the monthly SMB time-series do not exhibit significant trends and the discharge values are the same across the MBM estimates, we conclude that the differences in mean SMB account for most of the disagreement between various MBM estimates. This conclusion enables us to perform a simple adjustment of the SMB time-series with the ratio of mean magnitude of RACMO2.3p1 to that of each model during the reference period, given that MBM/RACMO2.3p1 has the best agreement with GRACE. Figure A2 shows the adjusted time-series for Amery, where the mean SMB from RACMO2.3p2 and MAR3.6.41 are lowered by 87.9%, and 87.1% respectively.

The modifications brought to RACMO2.3 version p2 compared to p1 made the coastline of East Antarctica drier and the interior regions wetter. Our assessment suggests that the model modifications may need to be revisited in light of our multi-sensor assessment, at least in the regions examined herein. In contrast, the impact of the model upgrade is negligible in the examined portions of West Antarctica, where the multi-sensor results agree within errors. Importantly, our results increase confidence in the large mass loss observed in the Getz Ice Shelf sector of West Antarctica and its acceleration in mass loss. We posit that this sector is strongly affected by enhanced intrusion of warm circumpolar deep water (CDW) on the continental shelf and beneath the ice shelf, which melts the ice shelf and glaciers, allows

the glacier grounding lines to retreat, speed up the ice flow, which contributes to sea level rise. In contrast, the Amery region is far from the sources of warm CDW and its unique geometry provides buttressing on three sides of the ice shelf. The drainage basin appears to be in a state of mass balance.

3.5 Conclusions

We quantify the mass balance of the drainage basins of two major regions of Antarctica, the Amery Ice Shelf in East Antarctica, and the Getz Ice Shelf in West Antarctica, using regionally-optimized GRACE mascons with minimal leakage. We compare the GRACE results with the Mass Budget Method (MBM) estimates using three different RCM output products. The Amery basin is in a state of mass balance, in agreement with MBM/RACMO2.3p1, but not with higher previous estimates of Yu et al. [2010]. Furthermore, we find MBM/RACMO2.3p2 and MBM/MAR3.6.41 produce significant positive trends of 8.8±2.9 and 9.4±2.7 Gt/yr, respectively. These differences are attributed to the magnitude of the mean monthly SMB values. Over Getz, we report a significant mass loss of 22.9±10.9 Gt/yr, in agreement with all MBM estimates. These estimates do not confirm positive trends derived with Cryosat-2 [Chuter et al., 2017] and more negative trends from other gravimetric results [Bouman et al., 2014]. The Getz region exhibits an accelerating loss at 1.6±0.9 Gt/yr^2, hence contributing to sea level rise at an accelerated pace. Overall, the regionally-optimized GRACE solutions provide an independent evaluation of the RCMs. Documenting and understanding the sources of these differences provides valuable insights about model performance that will subsequently help improve RCMs and remove residual uncertainties in the mass budget of Antarctica.

Acknowledgments

This work was performed at the University of California Irvine and at the Caltech Jet Propulsion Laboratory under a contract with the National Aeronautics and Space Administration Cryosphere Science Program. The Level-2 GRACE harmonics used in this study can be accessed on the Physical Oceanography Distributed Active Archive Center (PO.DAAC) at https://podaac-tools.jpl.nasa.gov/drive/files/GeodeticsGravity/grace/L2/CSR/RL06. MAR surface mass balance is available at ftp://ftp.climato.be/fettweis/. RACMO data is provided by the Institute for Marine and Atmospheric Research (IMAU) at Utrecht University at https://www.projects.science.uu.nl/iceclimate/publications/data/2018/index.php and https://doi.pangaea.de/10.1594/PANGAEA.896940. The data presented in this study is publicly accessible at https://www.ess.uci.edu/~velicogna/amery-getz.php and archived on Figshare according to the Enabling FAIR data guidelines at https://doi.org/10.6084/m9.figshare.9917210.

Table 3.1: Trends and accelerations and associated errors for the Amery and Getz drainage basins, Antarctica, from April 2002 to November 2015 (shifted to mid-month values to match GRACE). For each drainage basin the results obtained from GRACE corrected with Caron et al. [2018] GIA model from the expectation of a probability distribution from 128,000 forward models, and the Mass Budget Method (MBM) estimates obtained from RACMO2.3p1, RACMO2.3p2, and MAR3.6.41 are shown. The leakage between mascons is estimated from a synthetic field, while the ocean leakage is obtained from the GRACE coefficients representing ocean-only changes (GAD coefficients).

	Trend / Acc.	Total Error	Leakage Error	Regression Error	Ocean Leakage	GIA Error
Trend$[Gt/yr]$						
Amery						
GRACE	1.77	5.04	2.36	1.55	-0.73	4.11
MBM/MAR3.6.41	9.45	2.72				
MBM/RACMO2.3p1	-0.39	2.65				
MBM/RACMO2.3p2	8.85	2.88				
Getz						
GRACE	-22.91	10.91	10.28	1.44	0.56	3.21
MBM/MAR3.6.41	-23.64	6.19				
MBM/RACMO2.3p1	-23.84	6.27				
MBM/RACMO2.3p2	-25.35	6.28				
Acceleration$[Gt/yr^2]$						
Getz						
GRACE	-1.57	0.88	0.25	0.82	0.04	–
MBM/MAR3.6.41	-1.56	0.21				
MBM/RACMO2.3p1	-2.01	0.19				
MBM/RACMO2.3p2	-1.77	0.24				

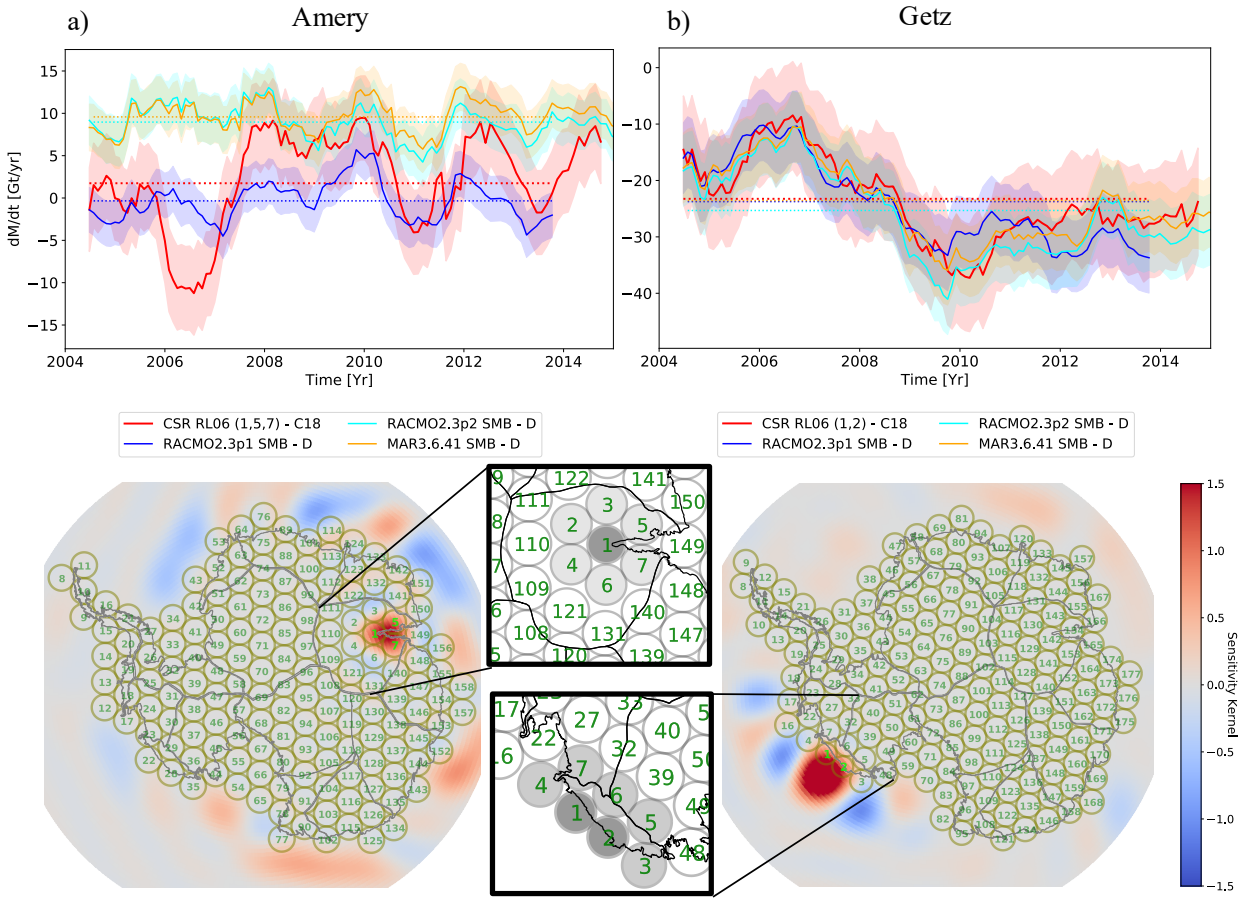

Figure 3.1: The rate of mass change time-series (dM/dt) in gigatons per year (10^{12} kg per year) obtained from a 36-month sliding window for **(a)** Amery and **(b)** Getz drainage basins, Antarctica, comparing the regionally optimized GRACE time-series (red) with the Mass Budget Method (MBM) estimate using RACMO2.3p1 (blue), RACMO2.3p2 (cyan), and MAR3.6.41 (orange). The dotted lines represent the mean trend during the common period. The corresponding mascon configurations and sensitivity kernels are shown below each time-series. The spherical caps are shown in gray circles, with the corresponding numerical labels in green. The caps used for the mass balance estimate are labelled in bright green. The insets show zoomed-in views of the caps of interest, with the lighter colors corresponding to increasing diameter — Amery: 2.7° (black), 2.9° (gray), and 3.2° (white); Getz: 2.6° (black), 2.8° (gray), and 3.0° (white).

Chapter 4

Detection of Glacier Calving Margins with Convolutional Neural Networks: A Case Study

As appears in:

Mohajerani, Y.; Wood, M.; Velicogna, I.; Rignot, E. "Detection of Glacier Calving Margins with Convolutional Neural Networks: A Case Study." Remote Sensing 11.1 (2019): 74. doi: 10.3390/rs11010074.

Abstract

The continuous and precise mapping of glacier calving fronts is essential for monitoring and understanding rapid glacier changes in Antarctica and Greenland, which have the potential for significant sea level rise within the current century. This effort has been mostly restricted to the slow and painstaking manual digitalization of the calving front positions in thousands of satellite imagery products. Here, we have developed a machine learning toolkit to automatically detect glacier calving front margins in satellite imagery. The toolkit is based on semantic image segmentation using Convolutional Neural Networks (CNN) with a modified U-Net architecture to isolate the calving fronts from satellite images after having been trained with a dataset of images and their corresponding manually-determined calving fronts. As a case study we train our neural network on a varied set of Landsat images with lowered resolutions from Jakobshavn, Sverdrup, and Kangerlussuaq glaciers, Greenland and test the results on images from Helheim glacier, Greenland to evaluate the performance of the approach. The neural network is able to identify the calving front in new images with a mean deviation of 96.3 m from the true fronts, equivalent to 1.97 pixels on average, while the corresponding error for manually-determined fronts on the same resolution images is 92.5 m (1.89 pixels). We find that the trained neural network significantly outperforms common edge detection techniques, and can be used to continuously map out calving-ice fronts with a variety of data products.

4.1 Introduction

In recent decades, tidewater glaciers discharging ice from the Greenland Ice Sheet have been thinning, speeding up and retreating inland [Howat et al., 2005, Moon and Joughin, 2008, Seale et al., 2011, Bjørk et al., 2012, Murray et al., 2015, Wood et al., 2018]. The position of

glacier ice fronts reflects a delicate balance of advection and ablation processes [Rignot et al., 2016] and hence is an important proxy for the impacts of regional changes in climate and ocean state on the mass balance in the Greenland Ice Sheet. To assess records of ice front retreat over time, ice front positions are typically manually digitized from aerial imagery Bjørk et al. [2012] or satellite imagery [Moon and Joughin, 2008, Murray et al., 2015] using Geographic Information System (GIS) software. Since the launch of Landsat 5 in 1984, the Landsat fleet has captured images of the Greenland Ice Sheet with a repeat cycle of 16 days. However, because the manual ice front digitization process requires a considerable time investment, most current records of calving front retreat are limited to only a few ice front positions per glacier per year, if any. This shortage of data poses a challenge to seasonal analyses of calving glaciers (e.g., [Schild and Hamilton, 2013, Motyka et al., 2017, Catania et al., 2018, Fried et al., 2018]), yet seasonal factors may be critical to understanding the pattern of long term retreat of Greenland's glaciers [Moon et al., 2015] or to understand for instance the level above which a glacier may be pushed out of balance compared to its state of seasonal, natural variability [Wood et al., 2018]. In effect, an automated system to rapidly delineate calving front positions would provide a foundation for understanding regional changes on the periphery of the ice sheet over the past several decades, especially with the emergence of a new generation of satellites with high data volume, a high number of acquisitions and higher resolution (e.g., [Wu et al., 2017, Roy et al., 2014, Potin et al., 2018, Markus et al., 2017]).

Detecting glacier calving fronts in images falls under a more general category of problems that deal with image segmentation. Generally, image segmentation techniques focus on either dividing an image into different regions (e.g., clustering, classification, region extraction) or finding the boundaries between regions (i.e., detection of discontinuities, edge detection). A detailed overview of these categories and techniques is given by [Fu and Mui, 1981]. Various techniques have been developed in the past for this class of problems. One of the most prominent of these analytical techniques is the Sobel filter, which uses gradients with a given

threshold to detect edges [Sobel, 1990]. Other approaches include the "Scale-Space" technique, which, first developed by Witkin et al. [1987], detects the desired feature at a coarser scale and tracks it continuously at a higher resolution. This approach was further improved by Perona and Malik [1990] by using an anisotropic diffusion process to keep the spatial accuracy of the features and detect edges. Applying these techniques to geophysical images such as ice-covered fjords and geologic formations is challenging due to the noisy nature of the data, variable atmospheric conditions (particularly clouds) and temporal changes on the ground. Seale et al. [2011] analyzed the evolution of calving fronts for 32 glaciers in Greenland using a Sobel filter as well as a brightness profiling technique applied to MODIS data. While achieving reasonable results below the resolution of MODIS (0.25 km), this approach relies on the proper selection of subregions around the calving front and heavy use of quality assurance and post-removal of anomalies. Furthermore, analytical techniques relying on brightness gradients in images are dependent on the particular nature of the data. For example, the same gradient thresholds may not be applicable to other instruments and spectral bands. They would also not be applicable to other data types such as radar interferometry (see Massonnet and Feigl [1998]). Finally, while this process provides an approximation of overall glacier retreat, it does not yield a digitized-front product which can be used by the glaciological community.

An alternative approach for overcoming these problems is the use of neural networks (see LeCun et al. [2015]) that can be trained on any data type to detect glacier fronts. Image segmentation techniques have improved rapidly in recent years due to the progress in deep learning and semantic image segmentation with Convolutional Neural Networks (CNNs) (e.g., see Krizhevsky et al. [2012]). Large neural networks with thousands or millions of parameters have allowed much more accurate classification and segmentation of images. In fact, deep neural networks with rectified activation units have already surpassed human performance in some visual recognition tasks (see He et al. [2015]).

The issue with such deep neural networks for image segmentation is the need for very large training datasets where the desired features (in this case calving fronts) have already been determined for thousands of images. For many fields of research the shortage of vast training data limits the use of such tools. However, a recent deep neural network architecture developed for biomedical image segmentation, U-Net [Ronneberger et al., 2015], has been shown to provide highly accurate image segmentation with minimal training data through the use of data augmentation in a deep convolutional neural network. Here we develop a modified version of the U-Net architecture that can identify and extract glacier calving fronts from optical satellite imagery. We discuss our results for a set of glaciers on the Greenland ice sheet. We compare our trained network with the Sobel filter. We conclude on the application of CNN technology to the detection of ice sheet calving margins.

4.2 Materials and Methods

We detect and reconstruct glacier calving fronts from Landsat imagery with the use of an image segmentation technique that relies on a deep convolutional neural network using a modified U-Net architecture [Ronneberger et al., 2015]. The methodology is divided into three overarching areas:

1. Discussion of raw satellite images, production of training data, and pre-processing of images before training

2. Semantic image segmentation and the architecture of the neural network

3. Reconstruction of new calving fronts on new data and the post-processing of the outputs of the neural network

Figure 4.1 summarizes the steps required to pre-process the data, train the network, make pre-

dictions, and get the glacier front positions after post-processing. Each of these steps are discussed in the following sections.

4.2.1 Data and Pre-Processing

We retrieve Level 1 Landsat Data from the USGS Earth Explorer portal for Landsat 5, Landsat 7, and Landsat 8. Calving fronts must be visually discernible in the images in order to be delineated. We mainly rely on L1TP products, but we do use some L1GT/L1GS products as we found the geo-referencing to be sufficient for our purposes. For Landsat 5, we utilize the "green" band (0.52–0.60 μm, where ice boundaries appear clearly) with a resolution of 30 m, while for Landsat 7 and 8 we utilize the "panchromatic" band (0.52–0.90 μm and 0.503–0.676 μm respectively) with a resolution of 15 m. We utilize images from 8 September 1985 to 26 July 2016 for Helheim glacier, 12 July 1994 to 20 October 2002 for Jakobshavn glacier, 3 October 1985 to 5 August 2016 for Kangerlussuaq glacier, and 29 May 1985 to 4 August 2015 for Sverdrup glacier. Furthermore, the seasonal distribution of the images is depicted in Figure B2.1. The scenes are delivered in the UTM projection corresponding to their longitude and latitude to maintain linear and areal distances. We crop the images to the region around the glacier ice front with a buffer of 300 m, an area we define using ice fronts that have previously been digitized manually. SLC-off images may also be used as long as these subset areas of interest are within the unaffected portions of the images.

In order to make it easier for the Neural Network (NN) to detect glacier fronts, we perform a series of pre-processing steps on the input images. Firstly, the cropped input images are mapped onto a rotated uniform grid (200×300 pixels) using cubic interpolation and oriented such that the glacier ice flow is in the y-direction for consistency, in order to improve the performance of the NN across a variety of images. Note that the size of the input images

are fixed in the neural network during training. Training the network on different fjord orientations through the use of additional rotation angles would significantly increase training time. Because the total retreat distance varies between glaciers, the scale of the 200×300 pixel images will also vary. In effect, the resolution of the image subsets are different for each glacier and the approach described herein does not operate on the native resolution of the Landsat products, but rather provides a benchmark for evaluating the performance of different neural network configurations compared to the analytical filter and manual results. The lower resolution images reduce computational resource and training time requirements for our case study. The pixel resolution varies per fjord based on the span of the retreat distance of each glacier over time. The pixel resolutions of the training data are as follows: 61.4 m for Sverdrup, 57.7 m for Kangerlussuaq, and 88.1 m for Jakobshavn. The pixel resolution of the test images on Helheim glacier is 49.0 m. Note that the test data has a slightly higher resolution than the training data, allowing us to test the performance of the NN across resolutions. The location of each fjord and the frames of the input images are shown in Figure B2.2. The corresponding calving front targets, hereinafter referred to as "labels", are manually determined on the original Landsat images and rasterized as single-pixel-thick lines for maximal spatial precision. We also further crop the input images to a size of 150×240 pixels with the aim of improving the training time while keeping all the calving fronts within the image frame. Note that this additional cropping is only for faster training and does not have to be applied to the test data. In addition, the architecture of the NN requires the dimensions to be divisible by the number of pooling steps described in the next section. With three pooling layers, the images are padded to be divisible by 8 (see Figure 4.2), resulting in 152×240 images.

Furthermore, we apply a series of alterations to the images to make the input more suitable for training the neural network. After a series of experiments with high-pass and low-pass filters, changes of contrast, and application of preliminary edge-detection algorithms, we find the following pre-processing steps provide datasets with consistent and interpretable

features for training of the NN, which lead to the best delineation results provided that the same steps are applied to the test data: First, we normalize the image contrasts such that the darkest and lightest points in every image are black and white, respectively. Next we equalize the gray-scale intensities to create a uniform distribution, followed by smoothing and edge-enhancement of the images using the `SMOOTH` and `EDGE ENHANCE` operations of the Python Image Library `http://www.pythonware.com/products/pil/`.

4.2.2 Semantic Image Segmentation

We develop a Convolutional Neural Network (CNN) [Rawat and Wang, 2017] with a U-Net architecture [Ronneberger et al., 2015] with custom sample weights for the segmentation of glacier fronts. U-Net has been very successful for semantic segmentation of biomedical images. It is built based on the architecture of Fully Convolutional Networks (FCN) [Long et al., 2015]. The challenge in semantic segmentation is resolving desired features ("what") and their contextual location ("where"). The idea of FCN is to combine fine, detailed features with coarse, contextual information. U-Net is a modification of such an architecture, which can be conceptualized as having two main components: (1) A "down" component that uses convolutional layers to detect desired features in images in progressively smaller layers with higher numbers of filters or "feature channels", and (2) An "up" component that has up-sampling layers to convey contextual information to higher resolution layers and reconstruct output images through convolutional layers. These components are labelled in the architecture of our neural network depicted in Figure 4.2. Convolutional layers consist of a series of kernels that are convolved across the input, mapping each group of pixels into single values in a new layer. These kernels act as filters that map out particular features from the image (such as features associated with glacier fronts). See LeCun et al. [2015] for a discussion of convolutional neural networks. Convolutions are represented by red, purple, or gray arrows, as discussed in the following paragraph. During the "down" component, pooling

layers are applied to downsample the output of each set of convolutional layers [LeCun et al., 2015]. Pooling is represented by blue arrows in the figure. This dimensionality reduction is a way of introducing location-invariance by combining similar features and coarsening the output of the convolutional kernels. In our neural network we use 2×2 max-pooling layers, which take the maximum value between each group of 4 pixels, resulting in location invariance within local batches and faster convergence of the network [Nagi et al., 2011]. In the second stage, the images are upsampled by doubling the rows and columns of the previous layer by repeating the rows and columns (represented by cyan arrows) and concatenated with the last convolutional layer with the same dimensions as the upsampled image (yellow arrows). Thus, the detailed global features in the last convolutional layer are combined with the contextual information of the previous layer. This combined upsampled layer is then fed to convolutional layers, as before. The reconstructed image by the last convolutional layer will have the same size as the input images and contain the desired segmented features.

The architecture of our neural network is depicted in Figure 4.2. Our network is composed of 29 total layers, with 3 downsampling steps and 4 sets of convolutional layers going from 32 to 256 feature channels and the corresponding upsampling steps. We apply 3×3 convolutional layers with padding (such that the output of each convolutional layer has the same image size as the input) and a step size ("stride") of 1 as the kernel moves across the image. We use Rectified Linear Units (ReLU) [Nair and Hinton, 2010] as our non-linear activation function, which has been shown to be very successful in convolutional neural networks [LeCun et al., 2015]. In order to apply regularization and avoid over-fitting to training data, we use Dropout layers [Srivastava et al., 2014] between convolutional layers with an elimination fraction of 0.2. This randomly drops some units at each iteration from the neural network in order to minimize over-fitting and excessive reliance on individual units. We find that increasing the dropout fraction significantly increases the "noise" (number of false-positives) in our results. The successive operations of 3×3 ReLU convolutions$\rightarrow$Dropout with 0.2 elimination fraction $\rightarrow$ 3×3 ReLU convolutions are depicted by single red ar-

rows in Figure 4.2 for succinct graphical representation. Our downsampling is performed by 2×2 MaxPooling layers with no padding and strides of 2, which are represented by blue arrows. Therefore, at every step the height and width of the layer is reduced by half while the number of convolutional kernels or bands (also known as feature channels) doubles. The same convolution→dropout→convolution architecture (red arrows) is used in the upsampling stage, where the number of feature channels is halved in each iteration. The 2×2 upsampling is done by repeating the rows and columns of the previous layer (cyan arrow), and concatenating the resulting matrix with the corresponding higher-resolution layer (yellow arrow). We get performance improvements by also adding a final 3×3 ReLU convolution to go from the final 32 channels to 3 (represented by a purple arrow), followed by a convolutional layer with a Sigmoid activation function (gray arrow) to get the final reconstructed image. The reconstructed image is flattened into a 36,480 $\times 1$ vector for the implementation of pixel-by-pixel sample weights during training, discussed below, which is represented by a black arrow in the final layer in Figure 4.2. The architecture of the network is also summarized in Table B1.

We use a binary cross-entropy loss function (see Mannor et al. [2005]) with custom sample weights for each input image. Note that images of glacier fronts pose a severe class imbalance problem, since the vast majority of pixels are not calving fronts. As a result, the NN learns to obtain high accuracy by simply classifying every pixel as not being part of the calving front. To avoid this false-negative classification artifact, we develop custom sample weights such that for every training example the pixels containing calving fronts have much higher penalties in the loss function if misidentified. In order to have an equal contribution from each class of pixels, the weight is determined as the average ratio of the number of non-boundary pixels to pixels including glacier front boundaries, which is 241.15 in our training set with 123 input images with dimensions 152×240. Note that while the weight is distributed individually for each training instance based on the position of the calving front, the value of the weight reflects the class imbalance of the training data in its entirety and is a constant

value for all pixels located on calving fronts. We also take advantage of data augmentation by mirroring the horizontal orientation of glaciers (i.e., flipping the images from left to right) to provide different fjord geometries and inverting the grayscale intensities to mimic different shadows. However, we get accurate results even without the use of augmentation, which speeds up the training process (discussed in the next section).

4.2.3 Post-Processing

To retrieve the geo-located ice front position from the output of the NN, we restore the padding and cropping of the images to the original 200 x 300 pixel size and identify the ocean/glacier area using pre-defined boundaries which delineate the fjord walls. These were obtained by digitizing the fjord boundaries in the same manner as the digitized "true labels". Note that these lines correspond only to the lateral boundaries of the fjords (i.e., independent of the calving front positions) and therefore only need to be defined once per glacier and may be used for all additional fronts obtained via the NN. We iterate through pairs of pixels on the fjord boundaries to find a least-cost path through the array, where the weights of each "step" are given by the output of the NN. A 500 m buffer is used from the fjord walls. The extracted path of pixels with the least weight is identified as the ice front, and converted to the geographical coordinates of the original clipped Landsat scene used to generate the subset. The geographical coordinates are stored as both raster data and shapefiles which may be used in Geographic Information System (GIS) software.

4.3 Results

We train the neural network on a set of 123 preprocessed 152×240 input images from Jakobshavn, Sverdrup, and Kangerlussuaq glaciers. Note that while this may seem like a limited

number of training instances, one of the advantages of the utilized network architecture used in this study is its ability to perform well with an extremely limited set of training data. In fact, the U-Net architecture used by Ronneberger et al. [2015] used a training set that consisted of 30 512×512 pixel images. Training success with few training images is in part enabled by data augmentation, which plays an important role in reducing our output errors, as discussed below. We leave aside 10% of the images chosen randomly during training for cross-validation. The validation dataset is used to prevent overfitting. The training is halted when the validation loss starts to increase as a result of overfitting. In addition, in order to test the ability of the neural network to predict calving fronts beyond the training set for different glacier geometries, we test the trained network on images of Helheim glacier, whose geometry is unknown to the NN during training. Note that this test dataset is in addition to the cross-validation data used during training. We minimize the custom-weighted binary cross-entropy loss function discussed in Section 2 using the Adam optimizer [Kingma and Ba, 2014] with batches of 10 images at a time. Furthermore, we use a variable learning rate, which is reduced by half after every 5 epochs without any improvements to the accuracy. We test the performance of a variety of NN configurations (discussed in the next section) and find that training the NN described in Figure 4.2 with horizontal mirroring augmentation with batches sizes of 10 leads to excellent agreement between the "generated" and "true" fronts. Training the network for 54 epochs leads to an accuracy of 92.4% in the training set and 93.6% in the validation set, after which the validation loss starts to increase as a result of over-fitting. Figure 4.3 shows the result of the NN network on a particularly noisy test image.

Panel (a) shows the pre-processed input image. Note that we pick this example as an instance of an image that can mislead analytical edge detection filters, but the reported results and errors are drawn from the complete test dataset. The raw output of the NN is shown in Panel (b). It is evident that the neural network is able to extract the calving front from the input image. Figure 4.3 also compares the output of the NN to the Sobel filter, a common

analytic edge detection algorithm that has been used in previous studies (e.g., see Seale et al. [2011]). It is clear from Panel (c) that the Sobel filter is very sensitive to noise and identifies many gradients in the texture of the glacier, the icebergs, and the surrounding topography as calving boundaries, which could lead to a false identification of the position of the calving front. Panel (d) shows the extracted fronts in post-processing (as discussed in Section 2.3). Note that we have also included a manually-determined front in addition to the "true" front. While the true front has also been determined manually on the original high resolution (i.e., uninterpolated) geocoded data, the "manual" comparison in Figure 4.3 refers to hand-drawn fronts on the pre-processed lower resolution rasterized images that are also used for the NN and Sobel processing for an equal comparison of the performances. The neural network performs remarkably well compared with the true boundary. However it is evident that the Sobel filter is not able to extract the calving front as accurately as the NN. Furthermore, the performance of the neural network appears to be comparable to manually-determined front. Results for other test images are provided in the Supplementary Material (Figure B3.1–10).

While Panels (a)–(d) of Figure 4.3 showcase the output of one image, Panels (e) and (f) show the error analysis obtained from the complete set of test images for the NN, Sobel filter, and manual results. We quantify the errors by breaking the extracted calving fronts of Helheim glacier (which was not used during training) into 1000 smaller line segments and calculating the mean difference between the corresponding segments of the generated and true fronts. Figure 4.3 shows the distribution of the differences for the NN (e) the Sobel filter (f), and manual results (g). We calculate the total error in the glacier fronts as the mean deviation between all 10,000 line segments in the outputted and true glacier front boundaries. The NN has a mean difference of 96.3 m, equivalent to 1.97 pixels, which is more than 8 times smaller than that of the Sobel filter. The manual output has a mean error of 92.5 m (1.89 pixels), only slightly below the error of the NN. Considering line segments only from the 8 scenes were the Sobel filter is able to successfully delineate the calving front, the errors are 85.3 m

(1.74 pixels), 193.0 m (3.94 pixels), and 89.1 m (1.82 pixels) for the NN, Sobel, and manual approaches, respectively. Most of the error in the NN output is attributed to the edges of the calving front, as can be seen in the Supplementary Material. Furthermore, it appears that the Sobel errors have a multimodal distribution. In other words, when the Sobel filter identifies the correct gradient as the calving front, it is in good agreement with the NN results. However, the filter can be easily mislead by other gradients in the image, resulting in a complete mis-identification and large errors for some images, leading to additional peaks in the histogram and larger overall errors. However, even when only the successful Sobel cases are compared, the NN mean error is less than half of that of the Sobel. The manual error histogram shows a more narrow distribution of errors, similar to the NN. The results from the NN, Sobel filter, and the manual technique for individual test images, along with the corresponding errors, can be viewed in the Supplementary Material.

Note that the errors are dependent on the resolution of the input images. As noted before, the resolution of our inputs are less than that of the native Landsat images in order to account for the possible span of ice fronts while minimizing image sizes and training time. However, the errors could be improved further by increasing the resolution and the areal extent of the input images, requiring more computational resources and increased training time. Thus, our benchmark analysis shown above is conducted on the same glacier to limit the influence of resolution and image size on the performance comparison of NN configurations and analytical filter and manual results. We performed the training with the interpolated images on an Intel 2.9 GHz CPU node with 5 Gigabytes of allotted memory. The training took 2 m and 17 s per epoch, resulting in just over two hours of training in total. More computational resources, in particular the use of Graphical Processing Units (GPUs), could result in significant improvements to the training time.

4.4 Discussion

Images of glacier calving fronts are inherently noisy, with a variety of surfaces and boundaries. Therefore, the application of analytical edge detection schemes such as the Sobel filter [Sobel, 1990] results in many false-positive predictions, where any sharp gradients on the surface of the glacier, icebergs, valley walls, and surrounding topography are likely to labeled as glacier calving fronts. In contrast, a convolutional neural network is able to learn the desired features in the images in order to correctly identify the calving front and mostly ignore other boundaries and sharp gradients. As discussed in Figure 4.3, the glacier fronts extracted from the output of the NN are in very close agreement to the true front and have similar errors as manually-determined fronts on the same resolution. The analytical filter, however, appears to be very sensitive to noise. It returns noisy images of sharp gradients from which the calving front cannot be correctly extracted in some cases. While customized analytical edge-detection schemes may be able to achieve reasonable results (see Seale et al. [2011]), they often rely on dataset-specific parameterizations and thresholds that are not readily applicable to various imagery solutions. The application of neural networks, on the other hand, does not require analytical customization for different datasets. The NN can be trained on any imagery product with the proper training labels. The applicability of NNs for the detection of calving fronts goes beyond optical imagery, and can be potentially applied to other forms of data such as radar, which will be explored in future studies.

The proper configuration and training of the NN can have a significant effect on the accuracy of the generated calving fronts. Figure 4.4 showcases various alterations to the NN on the same image used in Figure 4.3. Panels (a)–(c) use the architecture of the NN shown in Figure 4.2 without any data augmentation (a), horizontally mirroring the images (b), and horizontally mirroring and inverting the colors of the images (c) during training. We find that data augmentation results in more continuous calving fronts while generally reducing the "noise" (number of false-positives). However, color inversion does not seem to contribute

further to the performance of the network. In fact, while horizontal mirroring produces a mean deviation error of 96 m, the addition of inversion increases the error to 138 m. Furthermore, note that data augmentation increases the training time by several fold, depending on the number of alterations. Adding color inversion augmentation increases the training time per epoch from 137 to 217 seconds. As a result, it is desirable to use minimal augmentation while maintaining a low error. Therefore, we restrict the augmentation to horizontal mirroring. Furthermore, Panel (d) shows the effect of increasing the width of the glacier front lines in the training labels from 1 pixel to 3 pixels. While the mean error increases due to the loss of spatial precision, it is interesting to note that the noise, or number of false-positives, also decreases noticeably. This may be a result of the smaller class imbalance and weight ratio in the loss function (which decreases from 241.15 to 82.22), reducing the relative cost for a false classification of the calving fronts compared to background pixels. Therefore, if more pronounced calving front lines with minimal noise are required in post-processing, thicker labels may be desired.

We also find that the number of batches used during training has a significant effect on the results. We use batch sizes of 10 in the chosen NN. On the one hand, using larger batch sizes increases the noise in the output of the neural network, significantly decreasing the accuracy metric in the validation dataset. On the other hand, while using smaller batch sizes reduces the background noise, it also decreases the accuracy, with the mean error changing from 107 m (10 batches) to 152 m (3 batches), as shown in Panel (e). However, smaller batch sizes might be desirable if fewer false-negatives (at the cost of less continuous calving fronts) are required. Note that while smaller batch sizes increase training time per epoch, fewer iterations are required before overfitting in validation loss becomes evident.

Lastly, we also examine the effect of the depth and size of the neural network on the test results. While increasing the depth leads to smaller errors compared to increasing the width or the number of units in each layer (not shown), there are no improvements with respect

to the 29-layer NN, as shown in Panel (f). This may be due to the limited availability of training data for a deeper NN. The 37-layer NN (with one more downsample/upsamppling step compared to Figure 4.2) shows a more noisy output with a mean error of 112 m, slightly larger than the mean error of the corresponding 29-layer output in Panel (a). Note that the same relationship is true with the addition of augmentation. However, in the case of a larger and more varied training dataset, a deeper NN could potentially lead to further improvements.

4.5 Conclusions

We have used a Convolutional Neural Network (CNN) with a U-Net architecture [Ronneberger et al., 2015] to automatically detect glacier calving fronts in images obtained from Landsat 5 ("green" band) and Landsat 7 and 8 ("panchromatic" band). After exploring different network architectures and training and augmentation configurations, we find remarkable agreements between the true hand-drawn calving fronts and those obtained by a 29-layer deep neural network with 3×3 ReLU convolutional layers [Nair and Hinton, 2010], regularization with 0.2 Dropout layers [Srivastava et al., 2014], 2×2 downsamplinig (MaxPooling [Nagi et al., 2011]) and upsampling layers, a sample-weighted loss function based on the ratio of calving-front vs. non-calving-front pixels, and the utilization of data augmentation. We test the performance of the network not only on new images in the validation dataset, but also on an entirely new glacier with higher spatial resolution to test the effect of different fjord geometries and spatial resolutions on the trained network. After training the NN on Jakobshavn, Sverdrup, and Kangerlussuaq glaciers, we test it on Helheim glacier and obtain a mean deviation error of 96.3 m, equivalent to 1.97 pixels on average, which is comparable to the mean error of 92.5 m obtained from hand-drawn results on the same resolution. As a comparison, the Sobel filter [Sobel, 1990], a commonly used analytical edge-

detection method (e.g., see Seale et al. [2011]) results in a mean error of 836.3 m on the same dataset. Comparing only the successful cases of the Sobel filter, the errors are 85.3 m (1.74 pixels), 193.0 m (3.94 pixels), and 89.1 m (1.82 pixels) for the NN, Sobel, and manual techniques, respectively.

The success of the neural network (NN) in automatically detecting calving fronts, along with the need for a relatively small training set and short training times, makes this approach highly desirable for the continuous monitoring of numerous glaciers around the globe with the ever-growing wealth of remote-sensing data. The use of more spectral bands from various satellites can potentially improve the performance of the NN in the future. Furthermore, unlike analytical edge-detection techniques, the use of neural networks is not limited to optical imagery and can potentially be extended to many data forms such as radar. Therefore, the use of convolutional neural networks in the detection of calving fronts can be a widely applicable and powerful approach for future studies in order to monitor the retreat of numerous glaciers in real time.

Acknowledgments

This work was performed at the University of California, Irvine. Landsat data can be accessed at `https://earthexplorer.usgs.gov`. The neural network and the trained weights presented in this paper can be accessed at `https://github.com/yaramohajerani/FrontLearning`.

Supplementary: The architecture of the NN, the seasonal distribution and locations and frames of the training and testing images, and the generated fronts and the associated errors from the NN, Sobel filter, and manual results for sample test images of Helheim Glacier can be found in Appendix A.

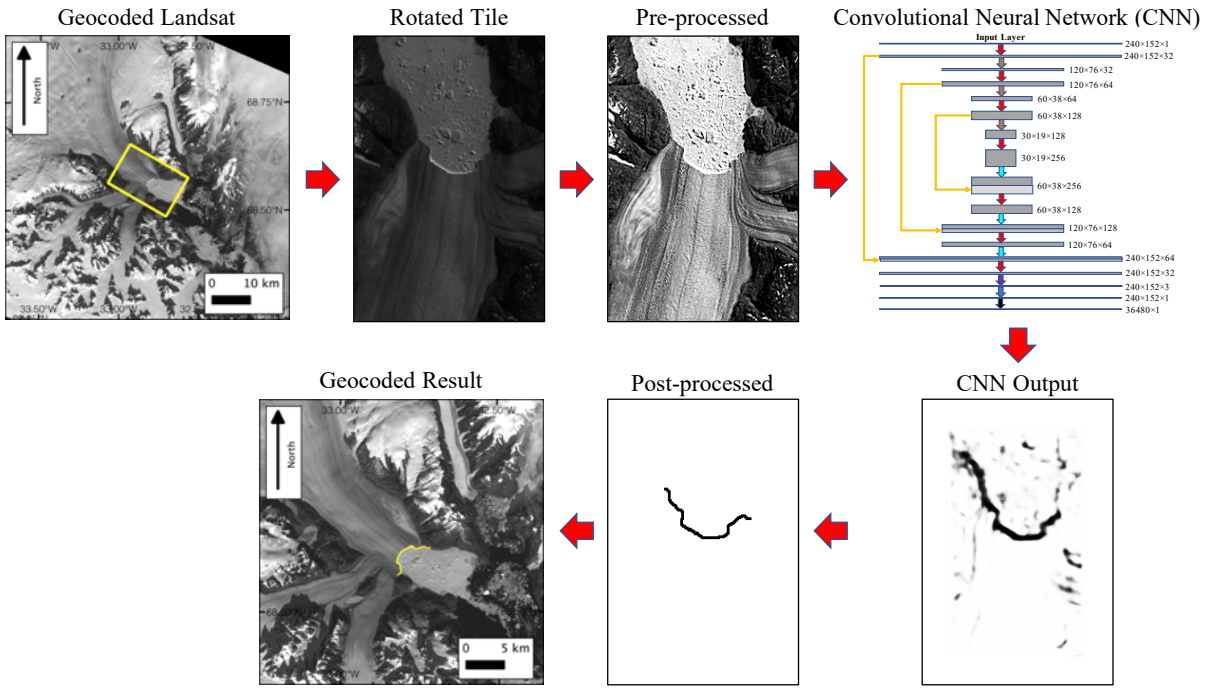

Figure 4.1: The outline of our methodology: Geocoded Landsat images are trimmed and rotated so that glacier flow is in the y-direction. The images are pre-processed and fed into to a Convolutional Neural Network (CNN) for training (refer to Figure 4.2 for a zoomed- in version of the CNN panel). The CNN is used to predict new calving front positions, which are post-processed and converted back to geocoded images.

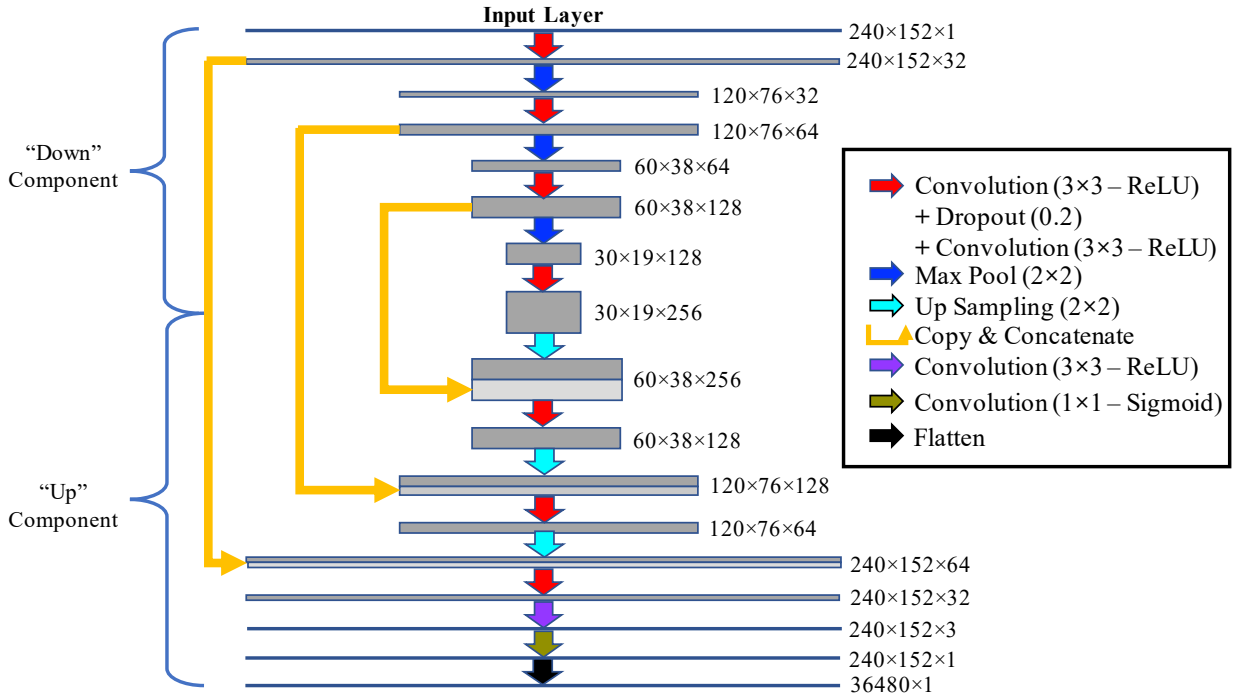

Figure 4.2: Architecture of the neural network. The length and width of each layer correspond to the pixel dimensions and the number of feature channels (bands) respectively. Convolutional and pooling kernel sizes and upsampling dimensions indicated in parentheses (e.g., 3×3 for convolutional layers and 2×2 for pooling). Dropout ratio indicated in parentheses (0.2). The activation function is also stated for convolutional layers (ReLU=REctified Linear Unit, and Sigmoid)

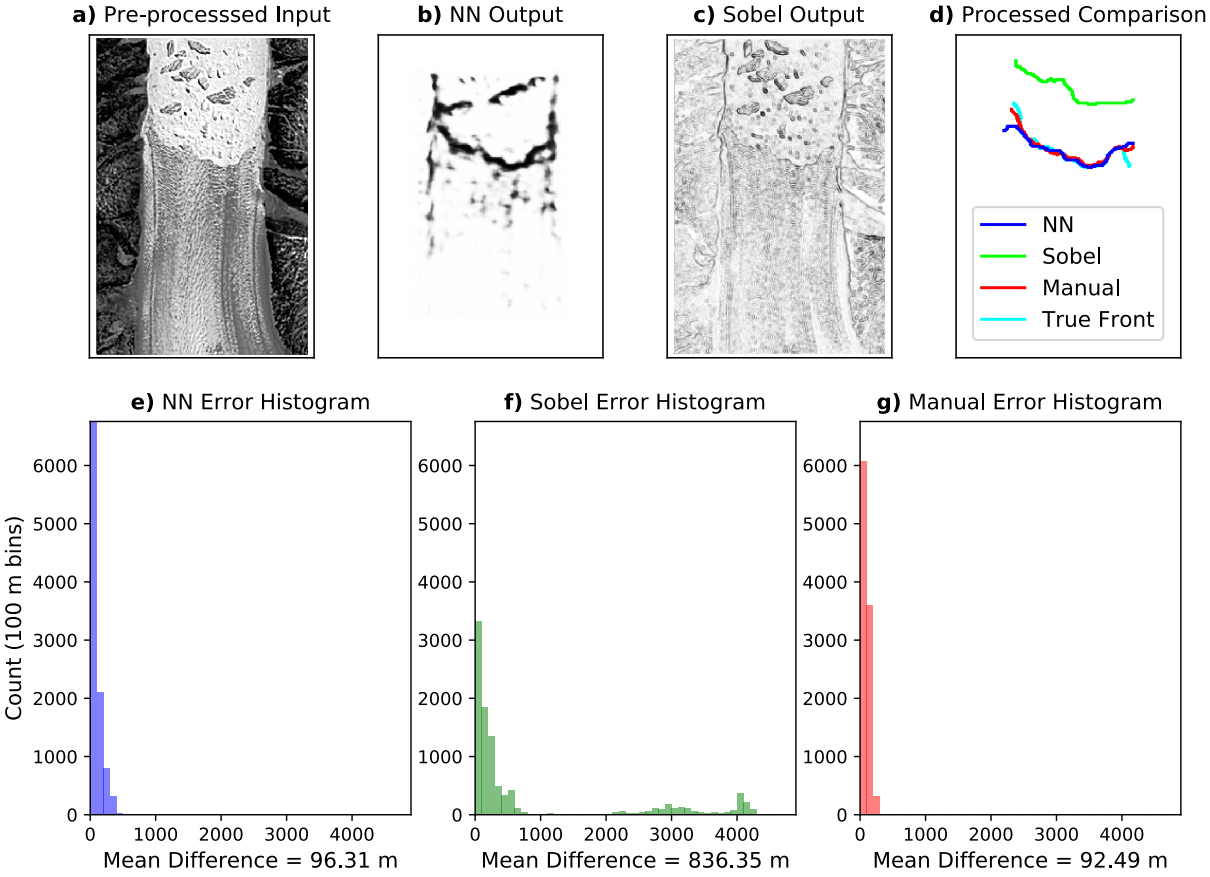

Figure 4.3: The output of the neural network shown for a sample test image of Helheim Glacier from Landsat 5. The pre-processed input image is shown in Panel (**a**). Panels (**b**,**c**) show the raw outputs of the neural network and the Sobel filter, respectively. Panel (**d**) depicts the corresponding extracted calving fronts compared to the true front, with the addition of the manually-determined front on the same resolution rasterized image used for the NN and Sobel filter. Note that the output of the NN shows remarkable agreement with the true front. Panels (**e**–**g**) show the distribution of differences between the generated and true fronts across *all* test images, with the corresponding mean differences with the true fronts for the NN, Sobel, and manual results, respectively. The NN difference of 96.3 m corresponds to 1.97 pixels. Considering only the 8 of 10 cases where the Sobel filter correctly identifies the calving front, the mean differences for the NN, Sobel, and manual techniques are 85.3 m (1.74 pixels), 193.0 m (3.94 pixels), and 89.1 m (1.82 pixels), respectively.

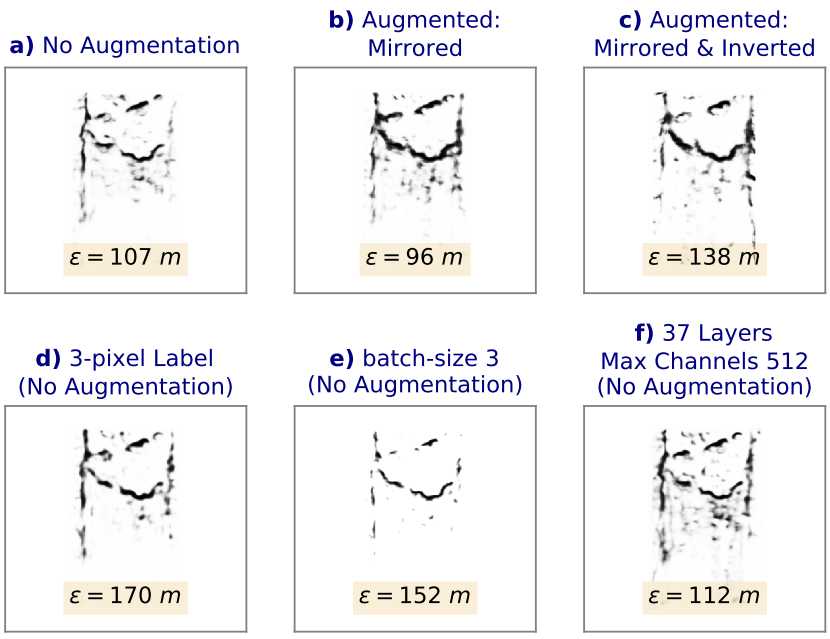

Figure 4.4: A comparison of raw outputs for various architecture and training configurations of the NN (**a**–**f**). ε represents the mean deviation from the true front for each case. Note the best results presented in the Results section correspond to Panel (b).

Chapter 5

Conclusions

The research presented in this dissertation focuses on improving regional mass balance estimates on the ice sheets and our understanding of the underlying processes using GRACE gravimetric remote sensing, evaluation of regional climate models using the Mass Budget Method, and the application of deep learning in satellite imagery products for the delineation of glacier calving fronts. Section 5.1 provides a summary of the results presented in chapters 2 to 4. Lastly, Section 5.2 discusses some of the implications and future directions of this work.

5.1 Summary of Results

The content of this dissertation can be divided into two overarching themes. Chapters 2 and 3 discuss the development of regionally-optimized spherical caps for the evaluation of basin and sub-basin mass balance from GRACE time-variable gravity data. In addition to the discussion of mass balance and the underlying processes in multiple Antarctic basins, these results help evaluate regional climate models and analyze the sources of discrepancies

between them. The second overarching theme is the application of deep convolutional neural networks for the analysis of the glacier calving fronts, as presented in Chapter 4. Each of these is summarized below.

In the first study, presented in Chapter 2, we illustrate a novel methodology for processing time-variable gravity data from the Gravity Recovery and Climate Experiment (GRACE) to improve regional mass balance estimates. The spherical cap methodology developed in Farrell [1972], and implemented in Velicogna et al. [2014] and Sutterley et al. [2014] as uniform caps, has been extended to locally-optimized variable-sized caps designed based on the regional geophysical signal to minimize leakage. The size, configuration geometry and placement of the caps is optimized such that each mascon samples a roughly uniform mass distribution, with the size reflecting the signal-to-noise ratio to avoid dominance of noisy higher-degree harmonics in smaller caps. Chapter 2 focuses on sub-basin and basin-wide mass balance estimates of the Totten and Moscow University glaciers. Together these two basins have 5 meters of sea level rise potential. In addition, their placement in the marine-sector of East Antarctica with a bed that's situated below sea-level [Young et al., 2011] makes them particularly important to understand and monitor.

We find a combined mass loss rate of 18.5±6.6 Gt/yr for Totten and Moscow University glaciers from April 2002 to August 2016 using the IJ05 R2 GIA model [Ivins et al., 2013]. The results are weakly affected by the choice of the GIA model. We also compute the mass budget using the grounding line discharge [Li et al., 2016] and SMB from two regional climate models: RACMO2.3 (p1) and MAR3.6.4. We show that MBM/RACMO2.3 is in excellent agreement with GRACE at a sub-basin scale, while MBM/MAR3.6.4 shows a less negative trend. These results confirm the state of mass loss in this part of the East Antarctic Ice Sheet, and suggest the need for further analysis of regional climate models.

This work is expanded on in Chapter 3, where regionally-optimized mascons are developed for the drainage basins of the Getz and Amery ice shelves. The Getz drainage basin in

West Antarctica is buttressed by an ice shelf with heterogenous influences and complex bathymetry that make it difficult to model and study [Jacobs et al., 2013]. Furthermore, this region has shown discrepancies between previous GRACE and Mass Budget estimates (e.g. Sasgen et al. [2010]). We show that with locally-optimized mascons that minimize leakage from nearby areas, the GRACE estimate is actually in excellent agreement with the Mass Budget estimates obtained from any of the regional climate models (RACMO2.3p1 [Van Wessem et al., 2014], RACMO2.3p2 [van Wessem et al., 2018], and MAR3.6.41 [Agosta et al., 2019]). We found a mass loss rate of 22.9±10.9 Gt/yr with an acceleration of 1.6±0.9 Gt/yr^2 for this region using GRACE with GIA correction from the expectation value of a set of 128,000 forward models for a comprehensive error analysis [Caron et al., 2018]. Previous estimates have produced a large range of inconsistent estimates in this region from 5±17 Gt/yr [Chuter et al., 2017] to -55±9 Gt/yr [Bouman et al., 2014]. Our regional GRACE estimate, in agreement with the Mass Budget Method, provides improved insight into the state of this drainage basin. Moreover, given the proximity of the Getz drainage basin to the high mass change signal of Amundsen Sea Sector glaciers, the agreement between GRACE and MBM illustrates that our regional optimization method can indeed be implemented on most locations across the ice sheets.

The Amery Ice Shelf drainage basin in East Antarctica has different characteristics. The ice shelf buttresses the drainage basin on 3 sides, and it appears to be in balance [Rignot et al., 2019]. Our gravimetric results confirm that the Amery basin is indeed in balance. This increases confidence that previous studies indicating a positive mass balance [Yu et al., 2010] overestimate the mass gain, which is attributed to the SMB model [Wen et al., 2014]. Indeed, we find that while MBM/RACMO2.3p1 is in agreement with GRACE, MBM/RACMO2.3p2 and MBM/MAR3.6.41 show positive trends as a result of the larger mean monthly magnitudes of RACMO2.3p2 and MAR3.6.41. The differences arise as a result of more than 10 Gt/yr difference in the mean monthly SMB values, as opposed to differences in SMB variability or trend. We show that the results for Totten and Moscow University glaciers in

Chapter 2 also exhibit these differences in East Antarctica due to mean SMB magnitude differences. By adjusting the SMB mean magnitude of each model by that of RACMO2.3p1, all MBM estimates fall into agreement with GRACE. This suggests that new developments in RACMO in East Antarctica may need to be revisited in the regions discussed here, while the same effect has not been detected in West Antarctica.

In the second portion of this dissertation, we showcase the implementation of deep convolutional neural networks (CNN) to delineate glacier calving fronts in Chapter 4. A modified U-Net architecture [Ronneberger et al., 2015] is developed to automatically delineate glacier calving fronts from Landsat imagery. The best results are obtained with a 29-layer CNN using custom sample weights (based on the proportion of calving front to non-front pixels). Furthermore, the results are significantly improved using additional augmentation where each image is horizontally mirrored to increase the variability and number of training samples. The CNN is trained on 123 images of Jakobshavn, Sverdrup, and Kangerlussuaq glaciers from Landsat 5, 7 and 8 ("green" band for the former and "panchromatic" band for the latter two). The trained network is tested on images of Greenland's Helheim glacier to test the ability of the network to perform on new sites. Remarkably, the performance of the neural network is comparable to the manual performance of human investigators. The CNN shows a mean deviation of 1.97 pixels between the recovered fronts and the true fronts (equivalent to 96.3 meters on the modified images of Helheim glacier with lowered resolution), while the manual human results have a corresponding mean deviation of 1.89 pixels (92.5 meters). These results show the potential for large-scale and automated delineation of the calving fronts of glaciers worldwide with properly trained convolutional neural networks. The implications and future directions of the research presented throughout this dissertation are discussed in the next section.

5.2 Implications and Future Work

The results presented in this dissertation enable an improved understanding of the mass balance of the ice sheets and the underlying processes at a regional level. Changes in the ice sheets have significant implications across the globe. Kopp et al. [2017] projected a median sea level rise value of 146 cm by the year 2100 under Representative Concentration Pathway (RCP) 8.5. However, there remains significant uncertainty in such estimates, with the 17–83 percentile range spanning 109 to 209 cm of sea level rise [Kopp et al., 2017]. The more recent Intergovernmental Panel on Climate Change (IPCC) Special Report on the Ocean and Cryosphere in a Changing Climate (SROCC) projected a median sea level rise value of 84 cm by 2100 relative to 1986–2005 under RCP 8.5, with a 17–83 percentile range ("likely range") of 61 to 110 cm [Oppenheimer et al., 2019]. Such differences and uncertainties, largely driven by the ice sheets, have important ramifications for millions of people living in low-lying coastal areas. The median projection for sea level rise by 2100 by Kopp et al. [2017] is expected to displace 153 million people around the globe in the absence of any mitigation strategies. Economic losses due to flooding are expected to increase from US$6 billion per year globally in 2005 to more than US$1 trillion by 2050 without any protective measures [Hallegatte et al., 2013]. Furthermore, sea level rise is expected to disproportionately affect less privileged people around the world. For example, 46% of the population of Bangladesh, 77% of the population of Suriname, and 88% of the population of the Bahamas are currently located in low elevation coastal zones, making them particularly vulnerable to the effects of sea level rise [McGranahan et al., 2007]. Thus, better understanding and monitoring of the ice sheets are of global importance. Careful regional assessments of mass balance, evaluation of model outputs, and continuous and wide-spread monitoring of glacier calving dynamics allow the scientific community to gain a better understanding of how the ice sheets respond to a changing climate. While we have taken several steps in this direction, future work remains, as outlined below.

The regional optimization methodology for GRACE harmonics has only been applied to a few regions on the Antarctic ice sheet in this dissertation. However, as illustrated by the success of the mascons on the Getz Ice Shelf basin in proximity to the large signal of Amundsen Sea Sector glaciers, this approach is applicable to most regions across the ice sheets. There is need for future work to design regionally-optimized mascon configurations for other regions to further assess the issue of larger monthly SMB magnitudes in East Antarctica in RACMO2.3p2 and MAR3.6.41, as well as the agreement of all MBM estimates with GRACE in West Antarctica. Similar estimates in Greenland are also invaluable for assessing regional climate models and GRACE on that ice sheet. Some preliminary work has shown excellent agreement between GRACE and extended MBM estimates in Greenland as well as West Antarctic sectors with large dynamic loss. In addition, these evaluations provide an excellent benchmark for evaluating the new GRACE Follow-On (FO) gravimetric data on the ice sheets.

The GRACE-FO mission was launched on May 22 2018 from the Vandenberg Air Force Base after the conclusion of the GRACE mission in October 2017 [Tapley et al., 2019]. Similar to the original GRACE satellite pair, GRACE-FO contains a microwave ranging system for measuring the inter-satellite distance, from which the time variable gravity field is obtained. However, GRACE-FO also includes a Laser Ranging Interferometer (LRI) system that allows a 26-fold improvement in inter-satellite distance measurement [Tapley et al., 2019]. While numerous factors, such as dealiasing models, affect the gravity product [Wiese et al., 2009], the LRI instrument may contribute to lower noise levels in GRACE FO data. Future work is needed to assess the size and configuration of regional mascon designs based on the noise level of the harmonics. It is important to emphasize this does not change the spatial resolution of the GRACE FO data, which is still limited to around 330 km (harmonics truncated at degree 60).

In addition, it is important for future work to assess the continuity of the gravimetric record

between GRACE and GRACE FO missions. Independent Mass Budget estimates presented in this dissertation can be particularly helpful in bridging the gap between the missions (June 2017 to June 2018). Preliminary analyses have not shown any biases between the two missions, with both being in agreement with regional MBM estimates. However, future work remains to carefully assess the continuity of the record across the ice sheets, analyze noise levels, and bridge the gap in the mass balance record between the two missions. For example, one of the accelerometers on the GRACE pair had to be shut down after August 2016, requiring an accelerometer transplant solution [Bandikova et al., 2019]. These months at the end of the GRACE mission exhibit significantly higher noise levels. An accelerometer transplant solution has also been implemented for GRACE-FO due to technical problems that led to one of the accelerometers being turned off. Analysis of the effects of these solutions, differences between GRACE and GRACE FO noise levels, impacts on ice sheet mass balance, and verification against independent mass balance estimates are crucial in future studies for a continuous and robust assessment of ice sheet mass balance.

Another valuable approach for the continual assessment of mass balance from independent observations is the recent launch of ICESat-2 (Ice, Cloud, and land Elevation Satellite-2) and the onboard Advanced Topographic Laser Altimeter System (ATLAS) instrument. ICESat-2 was launched in September of 2018 [Smith et al., 2019], led by NASA's Goddard Space Flight Center (GSFC) [Martino et al., 2019]. As opposed to its predecessor ICESat with a single laser beam [Schutz et al., 2005], ICESat-2 carries an array of six beams with a photon-counting sensor, recording the return time of individual photons. In addition, the design of three pairs of beams separated by 3.3 km allows the measurement of slopes on the surface of the ice [Smith et al., 2019]. This mission provides the opportunity for future studies to evaluate the mass balance of the ice sheets at a much finer resolution. While altimetry-driven mass balance estimates are dependent on firn density models for volume to mass conversion (see Shepherd et al. [2012, 2018]), they still provide a valuable opportunity for the inter-comparison of independent estimates in future studies. In addition, the different

natures of the gravimetry and altimetry data allows future studies to combine the data in unique ways to create higher-resolution hybrid solutions. Joint inversions of gravimetry, altimetry, and GPS data have been attempted in previous studies such as Martín-Español et al. [2016] and Engels et al. [2018]. However, ICESat-2 and GRACE-FO missions provide unique opportunities to combine the data either at the normal-equation level or at a post-processing level for improved regional estimates, taking advantage of the temporal and spatial characteristics of each mission.

It is also important for future studies to delve deeper into the differences between regional climate models that lead to varying agreement levels with gravimetric data. In Chapters 2 and 3 we showed that the Mass Budget estimates derived from RACMO2.3p2 and MAR3.6.41 SMB show more positive trends than those of RACMO2.3p1 and GRACE in the drainage basins of the Amery Ice Shelf and Totten and Moscow University glaciers in East Antarctica. The differences in magnitude between RACMO2.3p1 and RACMO2.3p2 are mostly attributed to wetter conditions in the interior and drier conditions on the coastline of East Antarctica in RACMO2.3p2 [Mohajerani et al., 2019a, van Wessem et al., 2018]. It is important for future investigations to explore differences in model physics and parameterization to improve the representation of surface mass balance that better match observations.

There is also significant need for future investigations to improve and build on the neural network approach for the delineation of calving fronts described in Chapter 4. Our investigation was a case-study with Landsat images of four glaciers with lowered resolutions. There is a need for future investigations to use more elaborate computational resources to train larger samples of high resolution images on many more glaciers and test the network along the Greenland and Antarctic ice sheets. Recent studies have made such attempts, including the use of a similar U-Net architecture with TerraSAR-X products [Zhang et al., 2019]. These Synthetic Aperture Radar (SAR) products have a much higher resolution of 3.3 to 3.5 meters. However, Zhang et al. [2019] only trained and tested the data on Jakobshavn Isbræ

and found an uncertainty of 38 meters. A more recent study by Baumhoer et al. [2019] used a similar U-Net architecture to delineate calving fronts on four training sites and four test sites around Antarctica using Sentinel-1 radar imagery and the Antarctic TanDEM-X digital elevation model. They found slightly larger delineation errors of 108 meters or 2.69 pixels compared to our study. Future studies are needed to test and improve the out-of-sample performance of these neural networks, and incorporate multiple data sources from visual and radar remote sensing products for a continuous and reliable delineation of calving front positions across the globe.

Furthermore, the use of machine learning can be extended to analyze other important aspects of the ice sheets. In addition to calving fronts, the determination of the grounding line, the boundary between the grounded and floating portions of a glacier [Cogley et al., 2011], is both crucial and challenging for a better assessment of the behavior of marine-terminating glaciers. The position of the grounding line is needed to determine the mass budget of glaciers and their contribution to sea level rise (e.g. Rignot et al. [2019]). Moreover, the dynamics of the grounding line are crucial to understanding and assessing the stability of glaciers and the role of Marine Ice Sheet Instability (MISI) in the long-term evolution of the ice sheets [Schoof, 2007]. Determining the position of the grounding line from observations has traditionally been done by the manual examination Differential Interferometric Synthetic Aperture Radar (DInSAR) [Rignot et al., 2011a]. This is done by differencing interferograms and manually delineating the grounding line in a labor-intensive process. Future investigations can extend the methodology of our study to interferometric data to delineate grounding lines in an automated fashion at a large scale. However, the different nature of this data poses challenges that may require different neural network architectures or training schemes. The desired features in the interferometric data can be much subtler, making it unclear whether convolutional kernels can successfully extract the desired boundary. It may be necessary to use a combination of machine learning and analytical techniques to overcome these difficulties. A recent study showcases the ability of convolutional neural networks to detect

continuous slow deformations in the solid Earth from interferograms [Anantrasirichai et al., 2019]. The authors remark that while there is potential utility in this approach, further developments may be needed for the wide applicability of convolutional neural networks in InSAR data. Additional challenges may also be posed by the less steady changes in glacier dynamics and the delineation of grounding lines. Future investigations are needed to identify and solve such challenges. These advancements will allow comprehensive monitoring of groundling lines across the ice sheets, not only allowing an improved assessment of present mass balance, but also future contributions to global sea level rise by a better understanding of the dynamics at grounding lines.

More generally, we are currently on the cusp of a big data revolution in remote sensing that will shift the bottleneck in understanding of glaciological processes from limited observations to limited analysis and interpretation of the large amount of data collected around the world. In addition to the aforementioned new missions such as ICESat-2 and GRACE-FO, numerous satellite imagery missions across the electromagnetic spectrum such as the WorldView [Anderson and Marchisio, 2012] and Landsat [Roy et al., 2014] series, Sentinel-2 [Drusch et al., 2012], commercial constellations such as RapidEye [Tyc et al., 2005] and SkySat [Murthy et al., 2014], and other small CubeSat operations [Wu et al., 2017] will provide a wealth of observational data. At the same time, developments in machine learning and artificial intelligence (AI) open up a range of new possibilities to take advantage of this data to lower uncertainties and improve our understanding of glaciological processes. In addition to feature recognition, such as delineation of calving fronts and grounding lines, deep learning techniques can be used to derive highly complex, nonlinear relationships that would not be easily found through traditional analytical approaches. For example, there is significant uncertainty in sea level projections due to calving dynamics and potential instability of tall ice cliffs ($\sim$1 km thickness with more than 90 m above water) without the support of buttressing ice shelves, referred to as Marine Ice Cliff Instability (MICI) [DeConto and Pollard, 2016, Bassis and Walker, 2011]. By considering ice cliff instability

and hydrofracturing, DeConto and Pollard [2016] predicted more than a meter of sea level rise by the end of the century from Antarctica alone. More recent studies have pointed out large uncertainties in MICI, emphasizing the lack of observational evidence [Edwards et al., 2019]. Continuous and global monitoring of all glaciers across the globe with machine learning techniques and the wealth of remote sensing data allows future investigations to dramatically increase observational constraints on the dynamics of glaciers. Furthermore, we aim to take advantage of deep learning to determine key variables relevant to calving dynamics in future studies. By using numerous characteristics such as strain rate, cliff height, and stress field for all glaciers on the Greenland and Antarctic ice sheets as inputs to a deep neural network and hind-casting observed calving events, not only can we determine the most important controllers of calving, but also determine nonlinear relationships that are not easily accessible through an analytical approach. New developments such as Layer-wise Relevance Propagation (LRP) [Montavon et al., 2019] allow us to peek into the neural network and learn potentially useful relationships between the variables. Such analyses have great potential for future studies to expand our understanding of glacier dynamics and processes controlling the long-term evolution and mass balance of the ice sheets.

All in all, there are still large uncertainties in the global and regional contribution of the ice sheets to future sea level rise, and significant work remains to reduce uncertainties, improve understanding, and assess the effects of the ice sheets in the 21st century. The new generation of remote-sensing missions such as GRACE-FO and ICESat-2 provide the opportunity to continue reducing mass balance uncertainty at all scales, evaluate regional climate models, and improve our understanding of processes. Improved real-time observational assessments at a large scale aided by novel approaches in machine learning and big data have the potential to significantly improve our understanding of processes governing ice sheet mass balance and potential instabilities. These multi-faceted approaches provide a rich and exciting arena for glaciological research in the years to come, the results of which are crucial for the adaptability and well-being of millions of people around the world.

Bibliography

G. A, J. Wahr, and S. Zhong. Computations of the viscoelastic response of a 3-d compressible earth to surface loading: an application to glacial isostatic adjustment in antarctica and canada. *Geophysical Journal International*, 192(2):557–572, 2013.

C. Agosta, C. Amory, C. Kittel, A. Orsi, V. Favier, H. Gallée, M. R. Broeke, J. Lenaerts, J. M. v. Wessem, W. J. v. d. Berg, et al. Estimation of the antarctic surface mass balance using the regional climate model mar (1979–2015) and identification of dominant processes. *The Cryosphere*, 13(1):281–296, 2019.

N. Anantrasirichai, J. Biggs, F. Albino, and D. Bull. The application of convolutional neural networks to detect slow, sustained deformation in insar timeseries. *Geophysical Research Letters*, 2019.

N. T. Anderson and G. B. Marchisio. Worldview-2 and the evolution of the digitalglobe remote sensing satellite constellation: introductory paper for the special session on worldview-2. In *Algorithms and Technologies for Multispectral, Hyperspectral, and Ultraspectral Imagery XVIII*, volume 8390, page 83900L. International Society for Optics and Photonics, 2012.

J. L. Bamber, R. E. Riva, B. L. Vermeersen, and A. M. LeBrocq. Reassessment of the potential sea-level rise from a collapse of the west antarctic ice sheet. *Science*, 324(5929): 901–903, 2009.

T. Bandikova, C. McCullough, G. L. Kruizinga, H. Save, and B. Christophe. Grace accelerometer data transplant. *Advances in Space Research*, 2019.

J. Bassis and C. Walker. Upper and lower limits on the stability of calving glaciers from the yield strength envelope of ice. *Proceedings of the Royal Society A: Mathematical, Physical and Engineering Sciences*, 468(2140):913–931, 2011.

C. A. Baumhoer, A. J. Dietz, C. Kneisel, and C. Kuenzer. Automated extraction of antarctic glacier and ice shelf fronts from sentinel-1 imagery using deep learning. *Remote Sensing*, 11(21):2529, 2019.

S. Bettadpur. Gravity recovery and climate experiment utcsr level-2 processing standards document. *University of Texas at Austin, GRACE Doc*, 327742:16, 2012.

S. Bettadpur. Gravity recovery and climate experiment utcsr level-2 processing standards document for level-2 product release 0006. *University of Texas at Austin, GRACE Doc*, 327742:16, 2018.

A. A. Bjørk, K. H. Kjær, N. J. Korsgaard, S. A. Khan, K. K. Kjeldsen, C. S. Andresen, J. E. Box, N. K. Larsen, and S. Funder. An aerial view of 80 years of climate-related glacier fluctuations in southeast greenland. *Nature Geoscience*, 5(6):427, 2012.

J. Bouman, M. Fuchs, E. v. Ivins, W. Wal, E. Schrama, P. Visser, and M. Horwath. Antarctic outlet glacier mass change resolved at basin scale from satellite gravity gradiometry. *Geophysical Research Letters*, 41(16):5919–5926, 2014.

E. Brun, P. David, M. Sudul, and G. Brunot. A numerical model to simulate snow-cover stratigraphy for operational avalanche forecasting. *Journal of Glaciology*, 38(128):13–22, 1992.

K. P. Burnham and D. R. Anderson. Multimodel inference: understanding aic and bic in model selection. *Sociological methods & research*, 33(2):261–304, 2004.

L. Caron, E. Ivins, E. Larour, S. Adhikari, J. Nilsson, and G. Blewitt. Gia model statistics for grace hydrology, cryosphere, and ocean science. *Geophysical Research Letters*, 45(5): 2203–2212, 2018.

G. Catania, L. Stearns, D. Sutherland, M. Fried, T. Bartholomaus, M. Morlighem, E. Shroyer, and J. Nash. Geometric controls on tidewater glacier retreat in central western greenland. *Journal of Geophysical Research: Earth Surface*, 123(8):2024–2038, 2018.

J. Chen, C. Wilson, R. Eanes, and R. Nerem. Geophysical interpretation of observed geocenter variations. *Journal of Geophysical Research: Solid Earth*, 104(B2):2683–2690, 1999.

J. Chen, C. Wilson, D. Blankenship, and B. Tapley. Accelerated antarctic ice loss from satellite gravity measurements. *Nature Geoscience*, 2(12):859–862, 2009.

J. Chen, C. R. Wilson, and B. D. Tapley. Interannual variability of greenland ice losses from satellite gravimetry. *Journal of Geophysical Research: Solid Earth*, 116(B7), 2011.

M. Cheng, B. D. Tapley, and J. C. Ries. Deceleration in the earth's oblateness. *Journal of Geophysical Research: Solid Earth*, 118(2):740–747, 2013.

S. Chuter, A. Martín-Español, B. Wouters, and J. L. Bamber. Mass balance reassessment of glaciers draining into the abbot and getz ice shelves of west antarctica. *Geophysical Research Letters*, 44(14):7328–7337, 2017.

J. G. Cogley, R. Hock, L. Rasmussen, A. Arendt, A. Bauder, R. Braithwaite, P. Jansson, G. Kaser, M. Möller, L. Nicholson, et al. Glossary of glacier mass balance and related terms, ihp-vii technical documents in hydrology no. 86, iacs contribution no. 2, 2011.

K. M. Cuffey and W. S. B. Paterson. *The physics of glaciers*. Academic Press, 2010.

V. Damm. A subglacial topographic model of the southern drainage area of the lambert glacier/amery ice shelf system-results of an airborne ice thickness survey south of the prince charles mountains. *Terra Antartica*, 14(1/2):85, 2007.

K. De Ridder and H. Gallée. Land surface–induced regional climate change in southern israel. *Journal of applied meteorology*, 37(11):1470–1485, 1998.

R. M. DeConto and D. Pollard. Contribution of antarctica to past and future sea-level rise. *Nature*, 531(7596):591, 2016.

D. P. Dee, S. Uppala, A. Simmons, P. Berrisford, P. Poli, S. Kobayashi, U. Andrae, M. Balmaseda, G. Balsamo, d. P. Bauer, et al. The era-interim reanalysis: Configuration and performance of the data assimilation system. *Quarterly Journal of the royal meteorological society*, 137(656):553–597, 2011.

H. Dobslaw, F. Flechtner, I. Bergmann-Wolf, C. Dahle, R. Dill, S. Esselborn, I. Sasgen, and M. Thomas. Simulating high-frequency atmosphere-ocean mass variability for dealiasing of satellite gravity observations: Aod1b rl05. *Journal of Geophysical Research: Oceans*, 118(7):3704–3711, 2013.

M. Drusch, U. Del Bello, S. Carlier, O. Colin, V. Fernandez, F. Gascon, B. Hoersch, C. Isola, P. Laberinti, P. Martimort, et al. Sentinel-2: Esa's optical high-resolution mission for gmes operational services. *Remote sensing of Environment*, 120:25–36, 2012.

T. Dupont and R. B. Alley. Assessment of the importance of ice-shelf buttressing to ice-sheet flow. *Geophysical Research Letters*, 32(4), 2005.

T. L. Edwards, M. A. Brandon, G. Durand, N. R. Edwards, N. R. Golledge, P. B. Holden, I. J. Nias, A. J. Payne, C. Ritz, and A. Wernecke. Revisiting antarctic ice loss due to marine ice-cliff instability. *Nature*, 566(7742):58, 2019.

O. Engels, B. Gunter, R. Riva, and R. Klees. Separating geophysical signals using grace and high-resolution data: A case study in antarctica. *Geophysical Research Letters*, 45(22): 12–340, 2018.

W. Farrell. Deformation of the earth by surface loads. *Reviews of Geophysics*, 10(3):761–797, 1972.

W. Farrell and J. A. Clark. On postglacial sea level. *Geophysical Journal International*, 46 (3):647–667, 1976.

X. Fettweis. Reconstruction of the 1979-2006 greenland ice sheet surface mass balance using the regional climate model mar. *The Cryosphere Discussions*, 1(1):123–168, 2007.

F. Flechtner, P. Morton, M. Watkins, and F. Webb. Status of the grace follow-on mission. in u. marti (ed.). In *Gravity, Geoid and Height Systems, Proceed. IAG Symp.*, volume 141, pages 117–121. Berlin: Springer, 2014.

P. Fretwell, H. D. Pritchard, D. G. Vaughan, J. L. Bamber, N. Barrand, R. Bell, C. Bianchi, R. Bingham, D. D. Blankenship, G. Casassa, et al. Bedmap2: improved ice bed, surface and thickness datasets for antarctica. *The Cryosphere*, 7:375–393, 2013.

M. Fried, G. Catania, L. Stearns, D. Sutherland, T. Bartholomaus, E. Shroyer, and J. Nash. Reconciling drivers of seasonal terminus advance and retreat at 13 central west greenland tidewater glaciers. *Journal of Geophysical Research: Earth Surface*, 123(7):1590–1607, 2018.

K.-S. Fu and J. Mui. A survey on image segmentation. *Pattern recognition*, 13(1):3–16, 1981.

H. Gallée, V. Peyaud, and I. Goodwin. Simulation of the net snow accumulation along the wilkes land transect, antarctica, with a regional climate model. *Annals of glaciology*, 41 (1):17–22, 2005.

H. Gallée, A. Trouvilliez, C. Agosta, C. Genthon, V. Favier, and F. Naaim-Bouvet. Transport of snow by the wind: a comparison between observations in adélie land, antarctica, and simulations made with the regional climate model mar. *Boundary-layer meteorology*, pages 1–15, 2013.

R. Gelaro, W. McCarty, M. J. Suárez, R. Todling, A. Molod, L. Takacs, C. A. Randles, A. Darmenov, M. G. Bosilovich, R. Reichle, et al. The modern-era retrospective analysis for research and applications, version 2 (merra-2). *Journal of Climate*, 30(14):5419–5454, 2017.

P. Gogineni, C. R. Simpson, J.-B. Yan, C. R. O'Neill, R. Sood, S. Z. Gurbuz, and A. C. Gurbuz. A cubesat train for radar sounding and imaging of antarctic ice sheet. In *IGARSS 2018-2018 IEEE International Geoscience and Remote Sensing Symposium*, pages 4138–4141. IEEE, 2018.

N. R. Golledge, D. E. Kowalewski, T. R. Naish, R. H. Levy, C. J. Fogwill, and E. G. Gasson. The multi-millennial antarctic commitment to future sea-level rise. *Nature*, 526(7573):421, 2015.

C. A. Greene, D. D. Blankenship, D. E. Gwyther, A. Silvano, and E. van Wijk. Wind causes totten ice shelf melt and acceleration. *Science Advances*, 3(11):e1701681, 2017.

J. A. Griggs and J. Bamber. Antarctic ice-shelf thickness from satellite radar altimetry. *Journal of Glaciology*, 57(203):485–498, 2011.

S. Hallegatte, C. Green, R. J. Nicholls, and J. Corfee-Morlot. Future flood losses in major coastal cities. *Nature climate change*, 3(9):802, 2013.

K. He, X. Zhang, S. Ren, and J. Sun. Delving deep into rectifiers: Surpassing human-level performance on imagenet classification. In *Proceedings of the IEEE international conference on computer vision*, pages 1026–1034, 2015.

B. Hofmann-Wellenhof and H. Moritz. *Physical geodesy*. Springer Science & Business Media, 2006.

I. M. Howat, I. Joughin, S. Tulaczyk, and S. Gogineni. Rapid retreat and acceleration of helheim glacier, east greenland. *Geophysical Research Letters*, 32(22), 2005.

C.-W. Hsu and I. Velicogna. Detection of sea level fingerprints derived from grace gravity data. *Geophysical Research Letters*, 44(17):8953–8961, 2017.

E. R. Ivins, T. S. James, J. Wahr, O. Schrama, J. Ernst, F. W. Landerer, and K. M. Simon. Antarctic contribution to sea level rise observed by grace with improved gia correction. *Journal of Geophysical Research: Solid Earth*, 118(6):3126–3141, 2013.

T. Jacob, J. Wahr, W. T. Pfeffer, and S. Swenson. Recent contributions of glaciers and ice caps to sea level rise. *Nature*, 482(7386):514–518, 2012.

S. Jacobs, C. Giulivi, P. Dutrieux, E. Rignot, F. Nitsche, and J. Mouginot. Getz ice shelf melting response to changes in ocean forcing. *Journal of Geophysical Research: Oceans*, 118(9):4152–4168, 2013.

J. Jungclaus, N. Fischer, H. Haak, K. Lohmann, J. Marotzke, D. Matei, U. Mikolajewicz, D. Notz, and J. Von Storch. Characteristics of the ocean simulations in the max planck institute ocean model (mpiom) the ocean component of the mpi-earth system model. *Journal of Advances in Modeling Earth Systems*, 5(2):422–446, 2013.

B. Karlik and A. V. Olgac. Performance analysis of various activation functions in generalized mlp architectures of neural networks. *International Journal of Artificial Intelligence and Expert Systems*, 1(4):111–122, 2011.

A. Khazendar, M. Schodlok, I. Fenty, S. Ligtenberg, E. Rignot, and M. Van den Broeke. Observed thinning of totten glacier is linked to coastal polynya variability. *Nature communications*, 4, 2013.

M. A. King, R. J. Bingham, P. Moore, P. L. Whitehouse, M. J. Bentley, and G. A. Milne. Lower satellite-gravimetry estimates of antarctic sea-level contribution. *Nature*, 491(7425): 586, 2012.

D. P. Kingma and J. Ba. Adam: A method for stochastic optimization. *arXiv preprint arXiv:1412.6980*, 2014.

S. Kobayashi, Y. Ota, Y. Harada, A. Ebita, M. Moriya, H. Onoda, K. Onogi, H. Kamahori, C. Kobayashi, H. Endo, et al. The jra-55 reanalysis: General specifications and basic characteristics. *Journal of the Meteorological Society of Japan. Ser. II*, 93(1):5–48, 2015.

R. E. Kopp, R. M. DeConto, D. A. Bader, C. C. Hay, R. M. Horton, S. Kulp, M. Oppenheimer, D. Pollard, and B. H. Strauss. Evolving understanding of antarctic ice-sheet physics and ambiguity in probabilistic sea-level projections. *Earth's Future*, 5(12):1217–1233, 2017.

A. Krizhevsky, I. Sutskever, and G. E. Hinton. Imagenet classification with deep convolutional neural networks. In *Advances in neural information processing systems*, pages 1097–1105, 2012.

Y. LeCun, Y. Bengio, and G. Hinton. Deep learning. *nature*, 521(7553):436, 2015.

X. Li, E. Rignot, M. Morlighem, J. Mouginot, and B. Scheuchl. Grounding line retreat of totten glacier, east antarctica, 1996 to 2013. *Geophysical Research Letters*, 42(19): 8049–8056, 2015.

X. Li, E. Rignot, J. Mouginot, and B. Scheuchl. Ice flow dynamics and mass loss of totten glacier, east antarctica, from 1989 to 2015. *Geophysical Research Letters*, 43(12):6366–6373, 2016.

J. Long, E. Shelhamer, and T. Darrell. Fully convolutional networks for semantic segmentation. In *Proceedings of the IEEE conference on computer vision and pattern recognition*, pages 3431–3440, 2015.

S. B. Luthcke, T. Sabaka, B. Loomis, A. Arendt, J. McCarthy, and J. Camp. Antarctica, greenland and gulf of alaska land-ice evolution from an iterated grace global mascon solution. *Journal of Glaciology*, 59(216):613–631, 2013.

M. B. Lythe and D. G. Vaughan. Bedmap: A new ice thickness and subglacial topographic model of antarctica. *Journal of Geophysical Research: Solid Earth*, 106(B6):11335–11351, 2001.

S. Mannor, D. Peleg, and R. Rubinstein. The cross entropy method for classification. In *Proceedings of the 22nd international conference on Machine learning*, pages 561–568. ACM, 2005.

T. Markus, T. Neumann, A. Martino, W. Abdalati, K. Brunt, B. Csatho, S. Farrell, H. Fricker, A. Gardner, D. Harding, et al. The ice, cloud, and land elevation satellite-2 (icesat-2): science requirements, concept, and implementation. *Remote sensing of environment*, 190:260–273, 2017.

S. J. Marshall. *The cryosphere*. Princeton University Press, 2011.

A. Martín-Español, A. Zammit-Mangion, P. J. Clarke, T. Flament, V. Helm, M. A. King, S. B. Luthcke, E. Petrie, F. Rémy, N. Schön, et al. Spatial and temporal antarctic ice sheet mass trends, glacio-isostatic adjustment, and surface processes from a joint inversion of satellite altimeter, gravity, and gps data. *Journal of Geophysical Research: Earth Surface*, 121(2):182–200, 2016.

A. J. Martino, T. A. Neumann, N. T. Kurtz, and D. McLennan. Icesat-2 mission overview and early performance. In *Sensors, Systems, and Next-Generation Satellites XXIII*, volume 11151, page 111510C. International Society for Optics and Photonics, 2019.

D. Massonnet and K. L. Feigl. Radar interferometry and its application to changes in the earth's surface. *Reviews of geophysics*, 36(4):441–500, 1998.

G. McGranahan, D. Balk, and B. Anderson. The rising tide: assessing the risks of climate change and human settlements in low elevation coastal zones. *Environment and urbanization*, 19(1):17–37, 2007.

M. McMillan, A. Shepherd, A. Sundal, K. Briggs, A. Muir, A. Ridout, A. Hogg, and D. Wingham. Increased ice losses from antarctica detected by cryosat-2. *Geophysical Research Letters*, 41(11):3899–3905, 2014.

Y. Mohajerani, I. Velicogna, and E. Rignot. Mass loss of totten and moscow university glaciers, east antarctica, using regionally optimized grace mascons. *Geophysical Research Letters*, 45(14):7010–7018, 2018.

Y. Mohajerani, I. Velicogna, and E. Rignot. Evaluation of regional climate models using regionally-optimized grace mascons in the amery and getz ice shelves basins, antarctica. *Accepted. Geophysical Research Letters*, 2019a. doi: 10.1029/2019GL084665.

Y. Mohajerani, M. Wood, I. Velicogna, and E. Rignot. Detection of glacier calving margins with convolutional neural networks: A case study. *Remote Sensing*, 11(1):74, 2019b.

G. Montavon, A. Binder, S. Lapuschkin, W. Samek, and K.-R. Müller. *Layer-Wise Relevance Propagation: An Overview*, pages 193–209. Springer International Publishing, Cham, 2019. ISBN 978-3-030-28954-6. doi: 10.1007/978-3-030-28954-6_10.

T. Moon and I. Joughin. Changes in ice front position on greenland's outlet glaciers from 1992 to 2007. *Journal of Geophysical Research: Earth Surface*, 113(F2), 2008.

T. Moon, I. Joughin, and B. Smith. Seasonal to multiyear variability of glacier surface velocity, terminus position, and sea ice/ice mélange in northwest greenland. *Journal of Geophysical Research: Earth Surface*, 120(5):818–833, 2015.

R. J. Motyka, R. Cassotto, M. Truffer, K. K. Kjeldsen, D. Van As, N. J. Korsgaard, M. Fahnestock, I. Howat, P. L. Langen, J. Mortensen, et al. Asynchronous behavior of outlet glaciers feeding godthåbsfjord (nuup kangerlua) and the triggering of narsap sermia's retreat in sw greenland. *Journal of Glaciology*, 63(238):288–308, 2017.

J. Mouginot, B. Scheuchl, and E. Rignot. Mapping of ice motion in antarctica using synthetic-aperture radar data. *Remote Sensing*, 4(9):2753–2767, 2012.

J. Mouginot, E. Rignot, A. A. Bjørk, M. van den Broeke, R. Millan, M. Morlighem, B. Noël, B. Scheuchl, and M. Wood. Forty-six years of greenland ice sheet mass balance from 1972 to 2018. *Proceedings of the National Academy of Sciences*, 116(19):9239–9244, 2019.

T. Murray, K. Scharrer, N. Selmes, A. Booth, T. James, S. Bevan, J. Bradley, S. Cook, L. C. Llana, Y. Drocourt, et al. Extensive retreat of greenland tidewater glaciers, 2000–2010. *Arctic, antarctic, and alpine research*, 47(3):427–447, 2015.

K. Murthy, M. Shearn, B. D. Smiley, A. H. Chau, J. Levine, and M. D. Robinson. Skysat-1: very high-resolution imagery from a small satellite. In *Sensors, Systems, and Next-Generation Satellites XVIII*, volume 9241, page 92411E. International Society for Optics and Photonics, 2014.

J. Nagi, F. Ducatelle, G. A. Di Caro, D. Cireşan, U. Meier, A. Giusti, F. Nagi, J. Schmidhuber, and L. M. Gambardella. Max-pooling convolutional neural networks for vision-based hand gesture recognition. In *Signal and Image Processing Applications (ICSIPA), 2011 IEEE International Conference on*, pages 342–347. IEEE, 2011.

V. Nair and G. E. Hinton. Rectified linear units improve restricted boltzmann machines. In *Proceedings of the 27th international conference on machine learning (ICML-10)*, pages 807–814, 2010.

B. Noël, W. J. van de Berg, V. Wessem, J. Melchior, E. Van Meijgaard, D. Van As, J. Lenaerts, S. Lhermitte, P. K. Munneke, C. Smeets, et al. Modelling the climate and surface mass balance of polar ice sheets using racmo2-part 1: Greenland (1958-2016). *Cryosphere*, 12(3):811–831, 2018.

M. Oppenheimer, B. Glavovic, J. Hinkel, R. van de Wal, A. K. Magnan, A. Abd-Elgawad, R. Cai, M. Cifuentes-Jara, R. M. Deconto, T. Ghosh, J. Hay, F. Isla, B. Marzeion, B. Meyssignac, and Z. Sebesvari. Sea level rise and implications for low lying islands, coasts and communities. *Special Report: The Ocean and Cryosphere in a Changing Climate (final draft)*, Chapter 4, 2019. URL `https://www.ipcc.ch/report/srocc/`.

W. R. Peltier and J. T. Andrews. Glacial-isostatic adjustment—i. the forward problem. *Geophysical Journal International*, 46(3):605–646, 1976.

P. Perona and J. Malik. Scale-space and edge detection using anisotropic diffusion. *IEEE Transactions on pattern analysis and machine intelligence*, 12(7):629–639, 1990.

M. Pittard, B. Galton-Fenzi, C. Watson, and J. Roberts. Future sea level change from antarctica's lambert-amery glacial system. *Geophysical Research Letters*, 44(14):7347–7355, 2017.

P. Potin, B. Rosich, N. Miranda, and P. Grimont. Sentinel-1a/-1b mission status. In *EUSAR 2018; 12th European Conference on Synthetic Aperture Radar*, pages 1–5. VDE, 2018.

H. Pritchard, S. Ligtenberg, H. Fricker, D. Vaughan, M. Van den Broeke, and L. Padman. Antarctic ice-sheet loss driven by basal melting of ice shelves. *Nature*, 484(7395):502–505, 2012.

H. D. Pritchard, R. J. Arthern, D. G. Vaughan, and L. A. Edwards. Extensive dynamic thinning on the margins of the greenland and antarctic ice sheets. *Nature*, 461(7266): 971–975, 2009.

W. Rawat and Z. Wang. Deep convolutional neural networks for image classification: A comprehensive review. *Neural computation*, 29(9):2352–2449, 2017.

E. Rignot and P. Kanagaratnam. Changes in the velocity structure of the greenland ice sheet. *Science*, 311(5763):986–990, 2006.

E. Rignot, J. L. Bamber, M. R. Van Den Broeke, C. Davis, Y. Li, W. J. Van De Berg, and E. Van Meijgaard. Recent antarctic ice mass loss from radar interferometry and regional climate modelling. *Nature geoscience*, 1(2):106–110, 2008.

E. Rignot, J. Mouginot, and B. Scheuchl. Antarctic grounding line mapping from differential satellite radar interferometry. *Geophysical Research Letters*, 38(10), 2011a.

E. Rignot, J. Mouginot, and B. Scheuchl. Ice flow of the antarctic ice sheet. *Science*, 333 (6048):1427–1430, 2011b.

E. Rignot, I. Velicogna, M. Van den Broeke, A. Monaghan, and J. Lenaerts. Acceleration of the contribution of the greenland and antarctic ice sheets to sea level rise. *Geophysical Research Letters*, 38(5), 2011c.

E. Rignot, S. Jacobs, J. Mouginot, and B. Scheuchl. Ice-shelf melting around antarctica. *Science*, 341(6143):266–270, 2013.

E. Rignot, Y. Xu, D. Menemenlis, J. Mouginot, B. Scheuchl, X. Li, M. Morlighem, H. Seroussi, M. v. den Broeke, I. Fenty, et al. Modeling of ocean-induced ice melt rates of five west greenland glaciers over the past two decades. *Geophysical Research Letters*, 43 (12):6374–6382, 2016.

E. Rignot, J. Mouginot, and B. Scheuchl. Measures insar-based antarctica ice velocity map, version 2. boulder, colorado usa. nasa national snow and ice data center distributed active archive center, 2017.

E. Rignot, J. Mouginot, B. Scheuchl, M. van den Broeke, M. J. van Wessem, and M. Morlighem. Four decades of antarctic ice sheet mass balance from 1979–2017. *Proceedings of the National Academy of Sciences*, 116(4):1095–1103, 2019.

O. Ronneberger, P. Fischer, and T. Brox. U-net: Convolutional networks for biomedical image segmentation. In *International Conference on Medical image computing and computer-assisted intervention*, pages 234–241. Springer, 2015.

D. P. Roy, M. Wulder, T. R. Loveland, C. Woodcock, R. Allen, M. Anderson, D. Helder, J. Irons, D. Johnson, R. Kennedy, et al. Landsat-8: Science and product vision for terrestrial global change research. *Remote sensing of Environment*, 145:154–172, 2014.

I. Sasgen, Z. Martinec, and J. Bamber. Combined grace and insar estimate of west antarctic ice mass loss. *Journal of Geophysical Research: Earth Surface*, 115(F4), 2010.

I. Sasgen, H. Konrad, E. Ivins, M. Van den Broeke, J. Bamber, Z. Martinec, and V. Klemann. Antarctic ice-mass balance 2003 to 2012: regional reanalysis of grace satellite gravimetry measurements with improved estimate of glacial-isostatic adjustment based on gps uplift rates. *The Cryosphere*, 7:1499–1512, 2013.

H. Save, S. Bettadpur, and B. D. Tapley. High-resolution csr grace rl05 mascons. *Journal of Geophysical Research: Solid Earth*, 121(10):7547–7569, 2016.

K. M. Schild and G. S. Hamilton. Seasonal variations of outlet glacier terminus position in greenland. *Journal of Glaciology*, 59(216):759–770, 2013.

C. Schoof. Ice sheet grounding line dynamics: Steady states, stability, and hysteresis. *Journal of Geophysical Research: Earth Surface*, 112(F3), 2007.

B. E. Schutz, H. Zwally, C. Shuman, D. Hancock, and J. DiMarzio. Overview of the icesat mission. *Geophysical Research Letters*, 32(21), 2005.

A. Seale, P. Christoffersen, R. I. Mugford, and M. O'Leary. Ocean forcing of the greenland ice sheet: Calving fronts and patterns of retreat identified by automatic satellite monitoring of eastern outlet glaciers. *Journal of Geophysical Research: Earth Surface*, 116(F3), 2011.

A. Shepherd, E. R. Ivins, A. Geruo, V. R. Barletta, M. J. Bentley, S. Bettadpur, K. H. Briggs, D. H. Bromwich, R. Forsberg, N. Galin, et al. A reconciled estimate of ice-sheet mass balance. *Science*, 338(6111):1183–1189, 2012.

A. Shepherd, E. Ivins, E. Rignot, B. Smith, M. Van Den Broeke, I. Velicogna, P. Whitehouse, K. Briggs, I. Joughin, G. Krinner, et al. Mass balance of the antarctic ice sheet from 1992 to 2017. *Nature*, 558:219–222, 2018.

A. Silvano, S. R. Rintoul, B. Peña-Molino, and G. D. Williams. Distribution of water masses and meltwater on the continental shelf near the totten and moscow university ice shelves. *Journal of Geophysical Research: Oceans*, 122(3):2050–2068, 2017.

B. Smith, H. A. Fricker, N. Holschuh, A. S. Gardner, S. Adusumilli, K. M. Brunt, B. Csatho, K. Harbeck, A. Huth, T. Neumann, et al. Land ice height-retrieval algorithm for nasa's icesat-2 photon-counting laser altimeter. *Remote Sensing of Environment*, page 111352, 2019.

I. Sobel. An isotropic 3× 3 image gradient operator. *Machine vision for three-dimensional scenes*, pages 376–379, 1990.

P. Spence, S. M. Griffies, M. H. England, A. M. Hogg, O. A. Saenko, and N. C. Jourdain. Rapid subsurface warming and circulation changes of antarctic coastal waters by poleward shifting winds. *Geophysical Research Letters*, 41(13):4601–4610, 2014.

N. Srivastava, G. Hinton, A. Krizhevsky, I. Sutskever, and R. Salakhutdinov. Dropout: a simple way to prevent neural networks from overfitting. *The Journal of Machine Learning Research*, 15(1):1929–1958, 2014.

U. S. G. Survey. Landsat—earth observation satellites. *U.S. Geological Survey Fact Sheet*, pages 2015–3081, 2015. URL `http://dx.doi.org/10.3133/fs20153081`.

T. C. Sutterley and I. Velicogna. Improved estimates of geocenter variability from time-variable gravity and ocean model outputs. *Remote Sensing*, 11(18):2108, 2019.

T. C. Sutterley, I. Velicogna, B. Csatho, M. van den Broeke, S. Rezvan-Behbahani, and G. Babonis. Evaluating greenland glacial isostatic adjustment corrections using grace, altimetry and surface mass balance data. *Environmental Research Letters*, 9(1):014004, 2014.

T. C. Sutterley, I. Velicogna, X. Fettweis, E. Rignot, B. Noël, and M. van den Broeke. Evaluation of reconstructions of snow/ice melt in greenland by regional atmospheric climate models using laser altimetry data. *Geophysical Research Letters*, 45(16):8324–8333, 2018.

S. Swenson and J. Wahr. Methods for inferring regional surface-mass anomalies from gravity recovery and climate experiment (grace) measurements of time-variable gravity. *Journal of Geophysical Research: Solid Earth*, 107(B9), 2002.

S. Swenson and J. Wahr. Post-processing removal of correlated errors in grace data. *Geophysical Research Letters*, 33(8), 2006.

S. Swenson, D. Chambers, and J. Wahr. Estimating geocenter variations from a combination of grace and ocean model output. *Journal of Geophysical Research: Solid Earth (1978–2012)*, 113(B8), 2008.

B. D. Tapley, S. Bettadpur, M. Watkins, and C. Reigber. The gravity recovery and climate experiment: Mission overview and early results. *Geophysical Research Letters*, 31(9), 2004.

B. D. Tapley, M. M. Watkins, F. Flechtner, C. Reigber, S. Bettadpur, M. Rodell, I. Sasgen, J. S. Famiglietti, F. W. Landerer, D. P. Chambers, et al. Contributions of grace to understanding climate change. *Nature Climate Change*, page 1, 2019.

G. Tyc, J. Tulip, D. Schulten, M. Krischke, and M. Oxfort. The rapideye mission design. *Acta Astronautica*, 56(1-2):213–219, 2005.

P. Undén, L. Rontu, H. Jarvinen, P. Lynch, F. J. Calvo Sánchez, G. Cats, J. Cuxart, K. Eerola, C. Fortelius, J. A. García-Moya, et al. Hirlam-5 scientific documentation. 2002. doi: 20.500.11765/6323.

S. M. Uppala, P. Kållberg, A. Simmons, U. Andrae, V. D. C. Bechtold, M. Fiorino, J. Gibson, J. Haseler, A. Hernandez, G. Kelly, et al. The era-40 re-analysis. *Quarterly Journal of the royal meteorological society*, 131(612):2961–3012, 2005.

R. Van de Wal, W. Boot, C. Smeets, H. Snellen, M. Van den Broeke, J. Oerlemans, et al. Twenty-one years of mass balance observations along the k-transect, west greenland. *Earth system science data discussions*, 5:351–363, 2012.

J. Van Wessem, C. Reijmer, M. Morlighem, J. Mouginot, E. Rignot, B. Medley, I. Joughin, B. Wouters, M. Depoorter, J. Bamber, et al. Improved representation of east antarctic surface mass balance in a regional atmospheric climate model. *Journal of Glaciology*, 60 (222):761–770, 2014.

J. M. van Wessem, W. Jan Van De Berg, B. P. Noël, E. Van Meijgaard, C. Amory, G. Birnbaum, C. L. Jakobs, K. Krüger, J. Lenaerts, S. Lhermitte, et al. Modelling the climate and surface mass balance of polar ice sheets using racmo2: Part 2: Antarctica (1979-2016). *Cryosphere*, 12(4):1479–1498, 2018.

D. G. Vaughan, J. L. Bamber, M. Giovinetto, J. Russell, and A. P. R. Cooper. Reassessment of net surface mass balance in antarctica. *Journal of climate*, 12(4):933–946, 1999.

I. Velicogna and J. Wahr. Measurements of time-variable gravity show mass loss in antarctica. *science*, 311(5768):1754–1756, 2006.

I. Velicogna and J. Wahr. Time-variable gravity observations of ice sheet mass balance: Precision and limitations of the grace satellite data. *Geophysical Research Letters*, 40(12): 3055–3063, 2013.

I. Velicogna, T. Sutterley, and M. van den Broeke. Regional acceleration in ice mass loss from greenland and antarctica using grace time-variable gravity data. *Geophysical Research Letters*, 41(22):8130–8137, 2014.

P. Visser, R. Rummel, G. Balmino, H. Sünkel, J. Johannessen, M. Aguirre, P. Woodworth, C. Le Provost, G. Tscherning, and R. Sabadini. The european earth explorer mission goce: impact for the geosciences. *Ice Sheets, Sea Level and the Dynamic Earth*, 29:95–107, 2002.

J. Wahr, M. Molenaar, and F. Bryan. Time variability of the earth's gravity field: Hydrological and oceanic effects and their possible detection using grace. *Journal of Geophysical Research: Solid Earth*, 103(B12):30205–30229, 1998.

J. Wahr, S. Swenson, and I. Velicogna. Accuracy of grace mass estimates. *Geophysical Research Letters*, 33(6), 2006.

J. Wahr, R. S. Nerem, and S. V. Bettadpur. The pole tide and its effect on grace time-variable gravity measurements: Implications for estimates of surface mass variations. *Journal of Geophysical Research: Solid Earth*, 120(6):4597–4615, 2015.

Y. Wang, M. Ding, J. Van Wessem, E. Schlosser, S. Altnau, M. R. van den Broeke, J. T. Lenaerts, E. R. Thomas, E. Isaksson, J. Wang, et al. A comparison of antarctic ice sheet surface mass balance from atmospheric climate models and in situ observations. *Journal of Climate*, 29(14):5317–5337, 2016.

M. M. Watkins, D. N. Wiese, D.-N. Yuan, C. Boening, and F. W. Landerer. Improved methods for observing earth's time variable mass distribution with grace using spherical cap mascons. *Journal of Geophysical Research: Solid Earth*, 120(4):2648–2671, 2015.

J. Wen, K. C. Jezek, B. M. Csathó, U. C. Herzfeld, K. L. Farness, and P. Huybrechts. Mass budgets of the lambert, mellor and fisher glaciers and basal fluxes beneath their flowbands on amery ice shelf. *Science in China Series D: Earth Sciences*, 50(11):1693–1706, 2007.

J. Wen, L. Huang, W. Wang, T. Jacka, V. Damm, and Y. Liu. Ice thickness over the southern limit of the amery ice shelf, east antarctica, and reassessment of the mass balance of the central portion of the lambert glacier-amery ice shelf system. *Annals of Glaciology*, 55 (66):81–86, 2014.

P. L. Whitehouse, M. J. Bentley, G. A. Milne, M. A. King, and I. D. Thomas. A new glacial isostatic adjustment model for antarctica: calibrated and tested using observations of relative sea-level change and present-day uplift rates. *Geophysical Journal International*, 190(3):1464–1482, 2012.

D. N. Wiese, W. Folkner, and R. Nerem. Alternative mission architectures for a gravity recovery satellite mission. *Journal of Geodesy*, 83(6):569–581, 2009.

D. N. Wiese, F. W. Landerer, and M. M. Watkins. Quantifying and reducing leakage errors in the jpl rl05m grace mascon solution. *Water Resources Research*, 52(9):7490–7502, 2016.

S. D. Williams, P. Moore, M. A. King, and P. L. Whitehouse. Revisiting grace antarctic ice mass trends and accelerations considering autocorrelation. *Earth and Planetary Science Letters*, 385:12–21, 2014.

R. Winkelmann, A. Levermann, M. A. Martin, and K. Frieler. Increased future ice discharge from antarctica owing to higher snowfall. *Nature*, 492(7428):239, 2012.

A. Witkin, D. Terzopoulos, and M. Kass. Signal matching through scale space. In *Readings in Computer Vision*, pages 759–764. Elsevier, 1987.

M. Wood, E. Rignot, I. Fenty, D. Menemenlis, R. Millan, M. Morlighem, J. Mouginot, and H. Seroussi. Ocean-induced melt triggers glacier retreat in northwest greenland. *Geophysical Research Letters*, 45(16):8334–8342, 2018.

S. Wu, T. Zhao, Y. Gao, and X. Cheng. Design and implementation of a cube satellite mission for antarctic glacier and sea ice observation. *Acta Astronautica*, 139:313–320, 2017.

C. Wunsch, P. Heimbach, R. M. Ponte, and I. Fukumori. The global general circulation of the ocean estimated by the ecco-consortium. *Oceanography*, 22(2):88–103, 2009.

D. A. Young, A. P. Wright, J. L. Roberts, R. C. Warner, N. W. Young, J. S. Greenbaum, D. M. Schroeder, J. W. Holt, D. E. Sugden, D. D. Blankenship, et al. A dynamic early east antarctic ice sheet suggested by ice-covered fjord landscapes. *Nature*, 474(7349):72–75, 2011.

J. Yu, H. Liu, K. C. Jezek, R. C. Warner, and J. Wen. Analysis of velocity field, mass balance, and basal melt of the lambert glacier–amery ice shelf system by incorporating radarsat sar interferometry and icesat laser altimetry measurements. *Journal of Geophysical Research: Solid Earth*, 115(B11), 2010.

E. Zhang, L. Liu, and L. Huang. Automatically delineating the calving front of jakobshavn isbræ from multitemporal terrasar-x images: a deep learning approach. *The Cryosphere*, 13(6):1729–1741, 2019.

Appendix A

Supplementary Material to Chapter 3

Introduction Additional details are provided in the following two figures: Figure A.1 shows the GRACE-derived rate of mass change time-series of Totten and Moscow University glaciers using the sub-basin mascon configuration of Mohajerani et al. [2018] and corrected with the expectation value of the ensemble of 128,000 forward modeling runs of the Caron et al. [2018] GIA model, compared to mass budget time-series derived from RACMO2.3p1 [Van Wessem et al., 2014], RACMO2.3p2 [van Wessem et al., 2018], and MAR3.6.41 [Agosta et al., 2019]. Consistent with the results from Amery, MBM/RACMO2.3p2 and MBM/MAR3.6.41 produce less negative trends.

Figure A.2 shows the rate of mass change time-series for Amery where the mass budget data has been adjusted as follows: the mean monthly SMB magnitude of each model is scaled by that of RACMO2.3p1 such that all models have the same overall mean magnitude.

The rate-of-change time-series are calculated using a 36-month sliding window. For each time-step i, the rate of mass change is calculated as

$$\left.\frac{dm}{dt}\right|_{t=\bar{t}} \approx \frac{m_{i+36} - m_i}{t_{i+36} - t_i} \tag{A.1}$$

where $\bar{t}$ is the arithmetic mean of the time interval $[t_i, t_{i+36}]$.

In addition, Table A.1 compares the mean monthly SMB values for RACMO2.3p1, RACMO2.3p2, and MAR3.6.41 for the Amery and Getz basins. In the Amery basin, where the MBM estimates differ, the mean mangitudes of RACMO2.3p2 and MAR3.6.41 are more than 10 Gt/yr larger than that of RACMO2.3p1, resulting in more positive mass budget estimates. In contrast, the RCMs show similar magnitudes in the Getz region.

Figure A.1 Comparison of regionally-optimized mascons for Totten and Moscow University glaciers sub-basin region using the mascon configuration of Mohajerani et al. [2018] with the corresponding mass budget estimates.

Figure A.2 Time-series of adjusted Mass Budget results in Amery where the surface mass balance is adjusted based on the mean magnitude of RACMO2.3p1, compared with the corresponding GRACE results.

Table A.1 Comparison of mean monthly SMB magnitudes from January 1979 to December 2015 in the Getz and Amery regions for RACMO2.3p1, RACMO2.3p2, and MAR3.6.41.

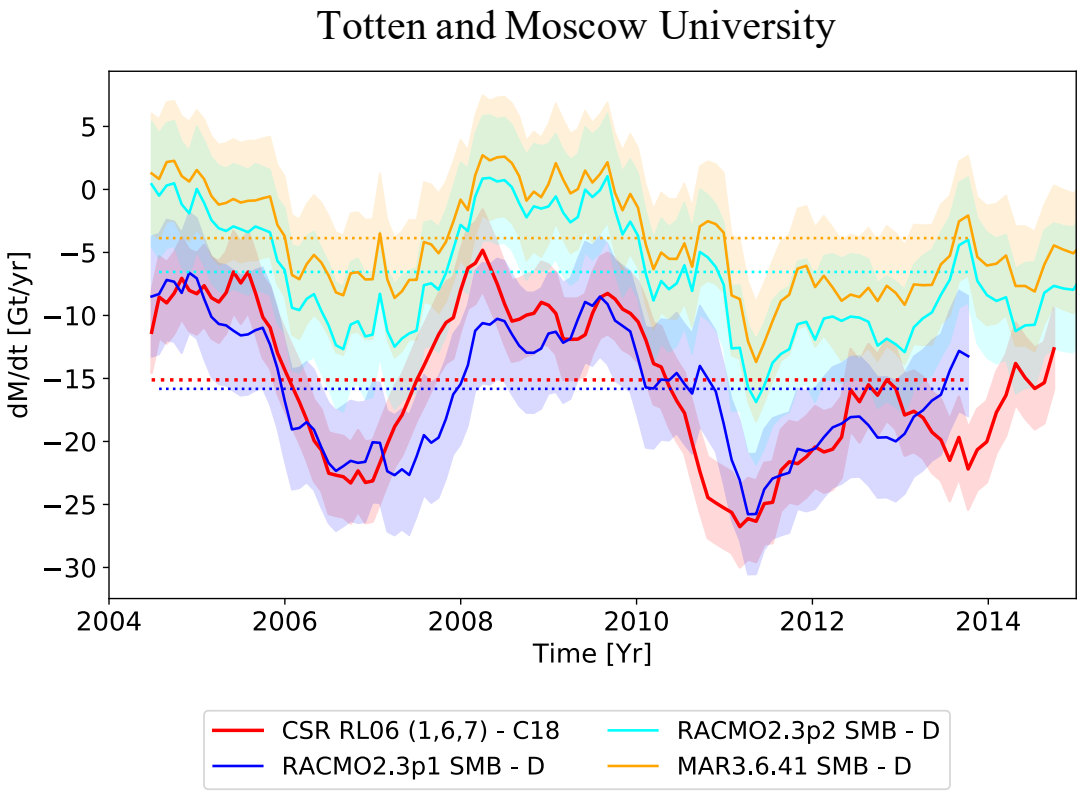

Figure A.1: Time-series of rate of mass change in gigatons per year (10^{12} kg per year) of Totten and Moscow University glaciers using the sub-basin mascon configuration of Mohajerani et al. [2018], where the GRACE estimate (red) has been corrected by the expectation value of the ensemble of GIA models from Caron et al. [2018], compared with Mass Budget estimates derived from RACMO2.3p1 (blue), RACMO2.3p2 (cyan), and MAR3.6.41 (orange). The dotted lines represent the mean trend during the common period.

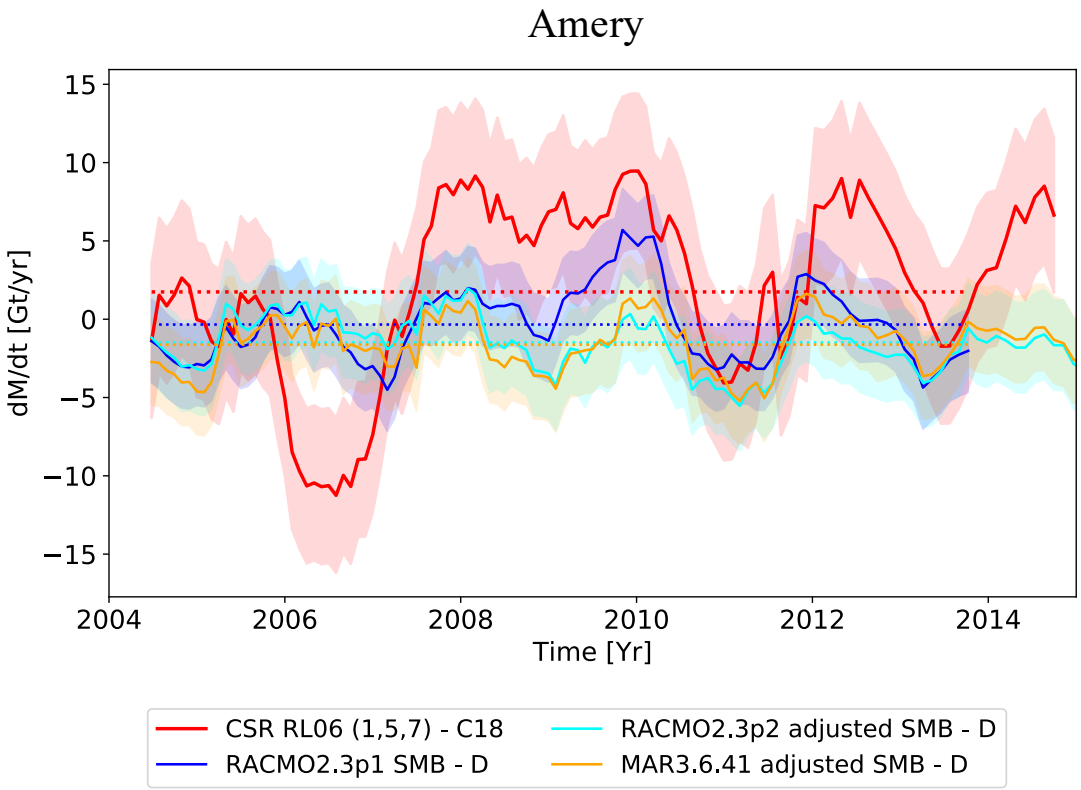

Figure A.2: Adjusted MBM time-series of rates of mass change in gigatons per year (10^{12} kg per year) in Amery for RACMO2.3p2 (cyan) and MAR3.6.41 (orange) using the reference period mean of RACMO2.3p1 (blue), compared with the GRACE time-series (red). The dotted lines represent the mean trend during the common period.

Table A.1: Comparison of mean monthly SMB magnitudes from January 1979 to December 2015 in Gt/yr. The errors are calculated following Rignot et al. [2019].

	Amery	Getz
RACMO2.3p1 (Gt/yr)	75.6±4.5	100.8±5.9
RACMO2.3p2 (Gt/yr)	85.8±5.1	100.2±5.9
MAR3.6.41 (Gt/yr)	87.1±5.1	101.3±6.0

Appendix B

Supplementary Material to Chapter 4

B.1 Architecture of Neural Network

Architecture of the neural network corresponding to Figure 4.2. "Conv" denotes a convolutional layer with ReLU activation a 3×3 kernel, unless specified otherwise as in layer 28. All layers are as described in Methods.

B.2 Seasonal Distribution of Location of Data

The seasonal distribution, location, and frames of the images used for training and testing.

B.3 Outputs and Errors on Helheim Glacier

The outputs and corresponding errors of the Neural Network (NN), Sobel filter, and manual technique for 10 test images from Helheim Glacier.

Table B.1

Layer	Type	Output Size
1	Input	240×152×1
2-4	Conv → Dropout (0.2) → Conv	240×152×32
5	MaxPool (2×2)	120×76×32
6-8	Conv → Dropout (0.2) → Conv	120×76×64
9	MaxPool (2×2)	60×38×64
10-12	Conv → Dropout (0.2) → Conv	60×38×128
13	MaxPool (2×2)	30×19×128
14-16	Conv → Dropout (0.2) → Conv	30×19×256
17	Upsample (2×2) and Concatenate with layer 12	60×38×256
18-20	Conv → Dropout (0.2) → Conv	60×38×128
21	Upsample (2×2) and Concatenate with layer 8	120×76×128
22-24	Conv → Dropout (0.2) → Conv	120×76×64
25	Upsample (2×2) and Concatenate with layer 4	240×152×64
26-28	Conv → Dropout (0.2) → Conv	240×152×32
27	Conv	240×152×3
28	Conv (1×1 - Sigmoid)	240×152×1
29	Flatten for dynamic weighting	36480×1

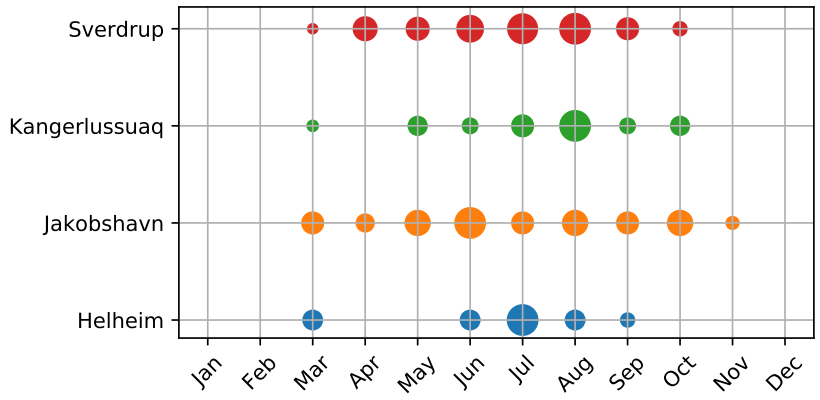

Figure B2.1: The seasonal distribution of the images used for training (top three rows: Sverdrup, Kangerlussuaq, and Jakobshavn glaciers), and testing (bottom row: Helheim glacier). The marker sizes correspond to the number of images for each month (normalized).

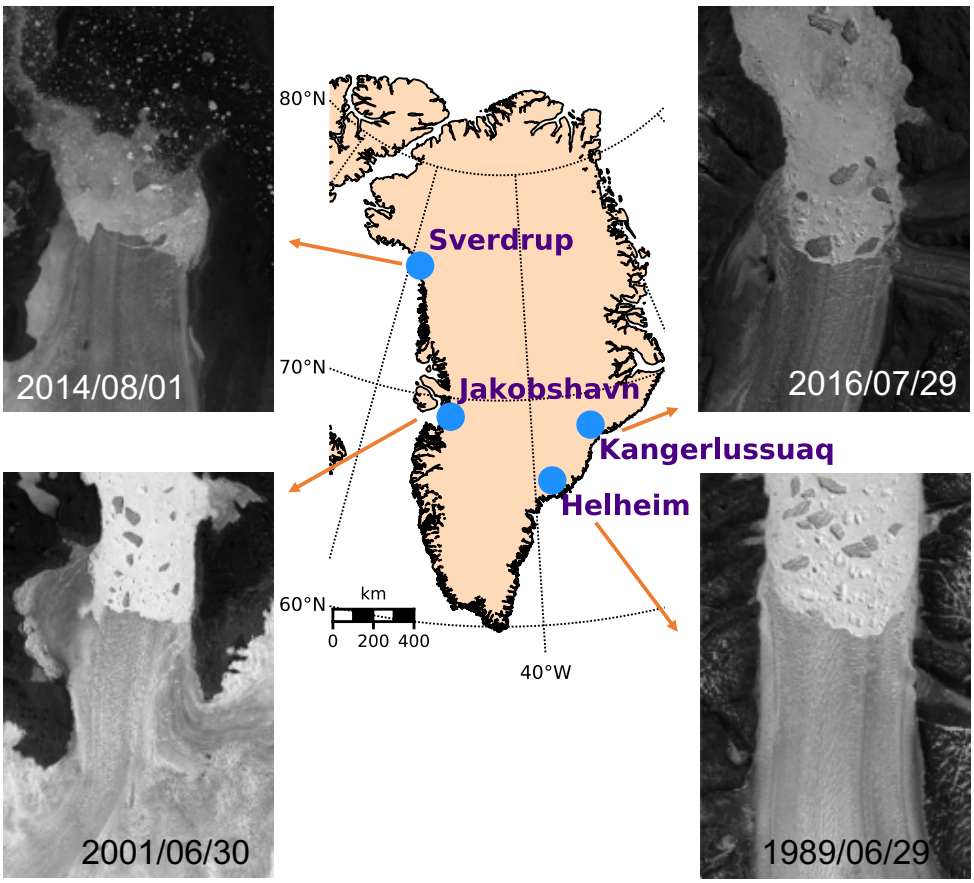

Figure B2.2: The location of the training (Sverdrup, Kangerlussuaq, and Jakobshavn glaciers) and testing (Helheim glacier) sites, with examples of each fjord to show the extent of the frames used in the neural network.

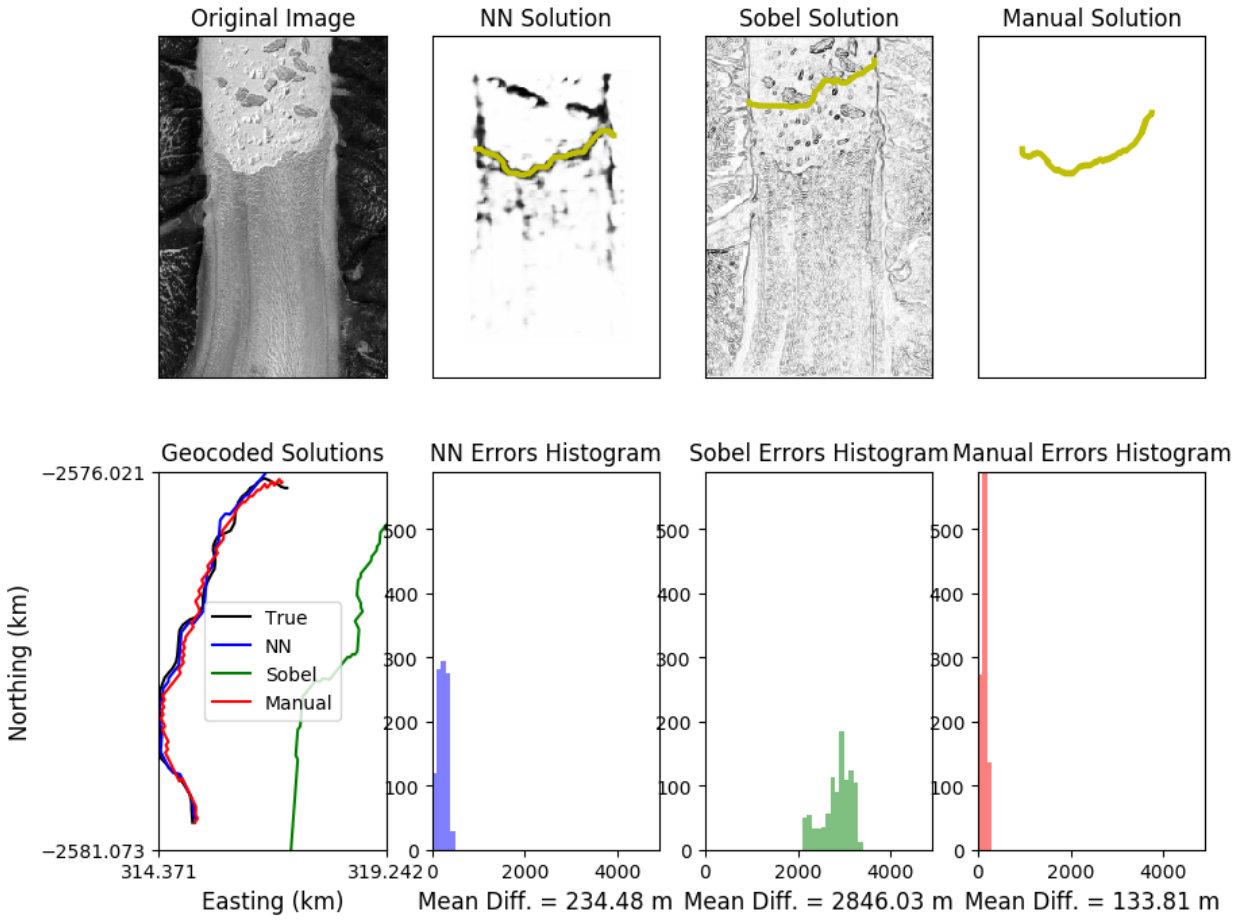

Figure B3.1: Landsat 5 - June 29, 1989

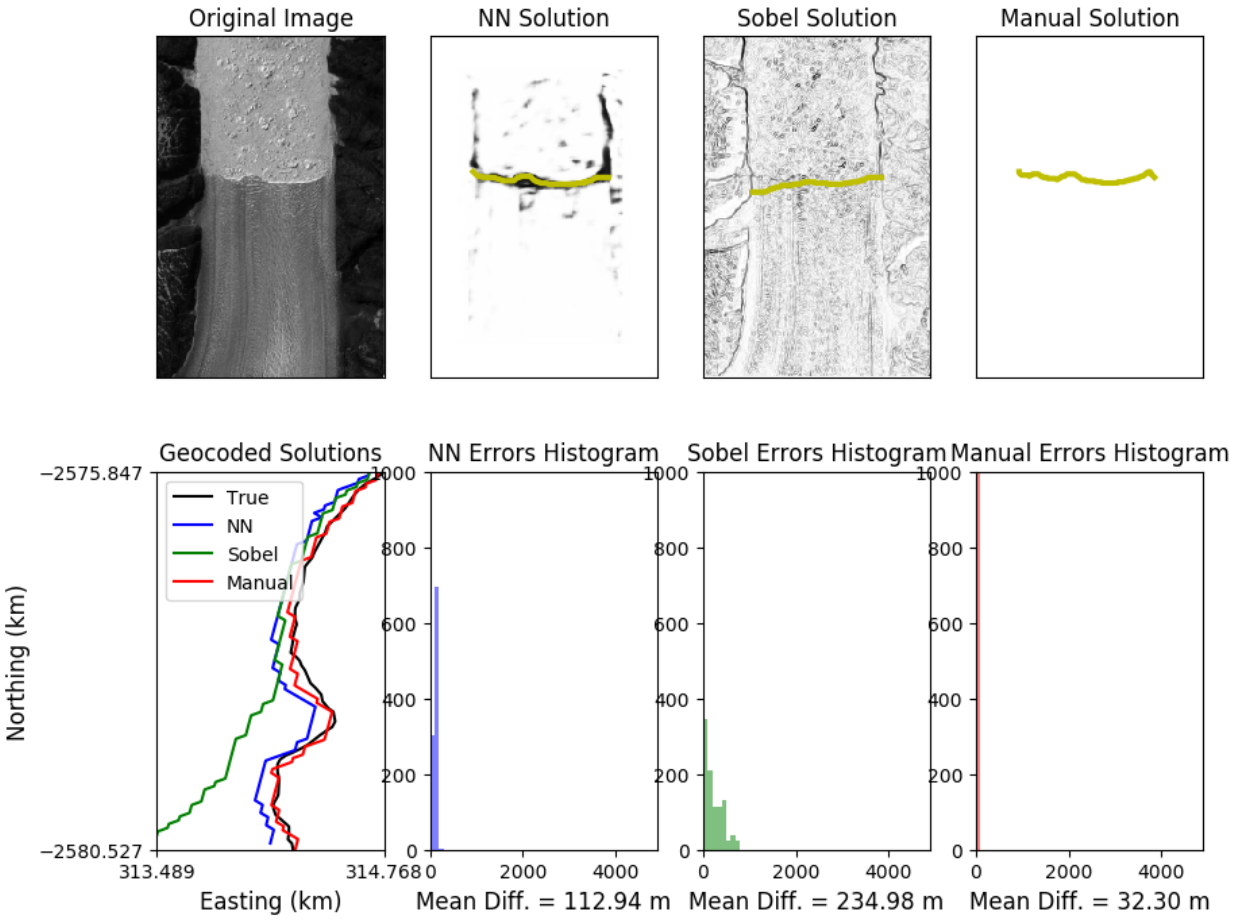

Figure B3.2: Landsat 5 - August 30, 1994

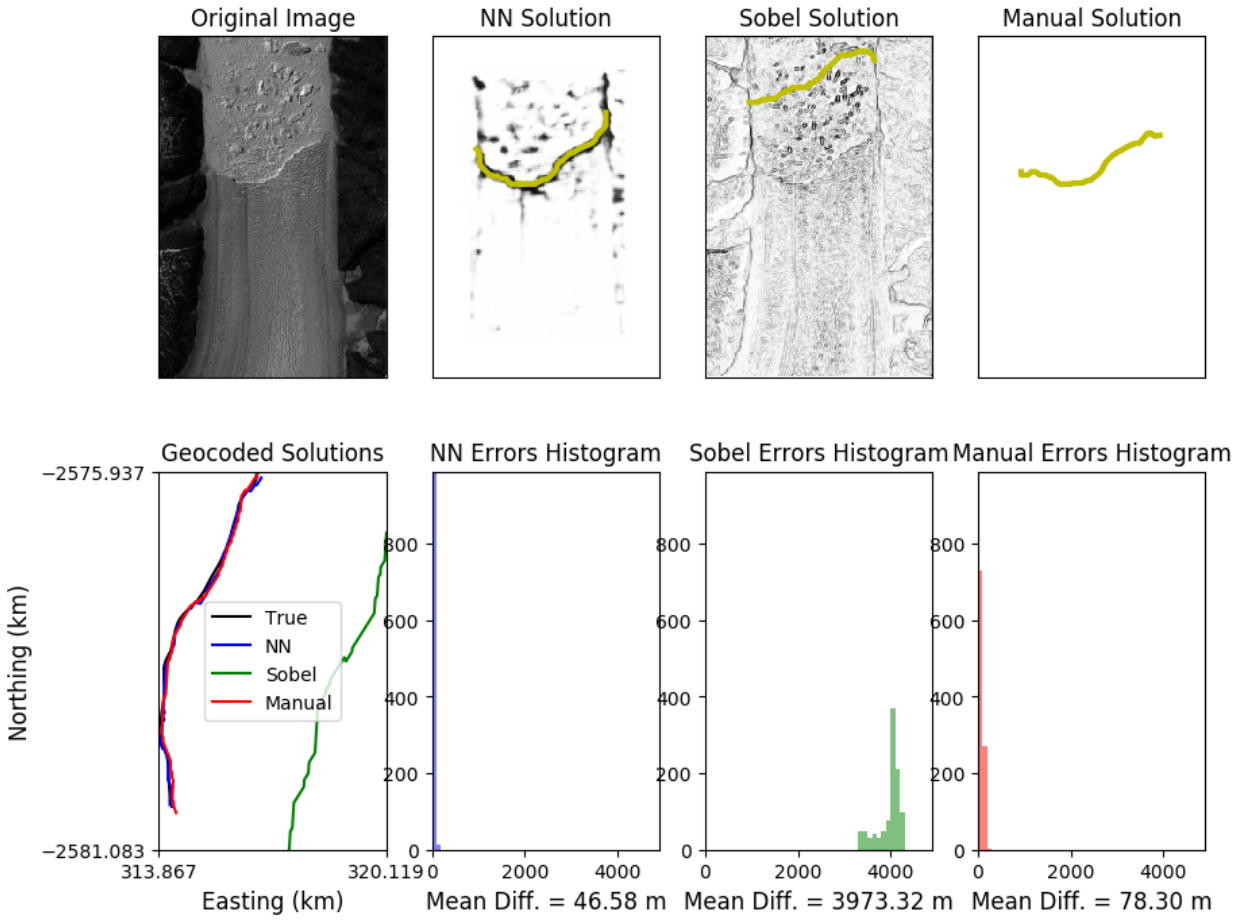

Figure B3.3: Landsat 5 - September 8, 1985

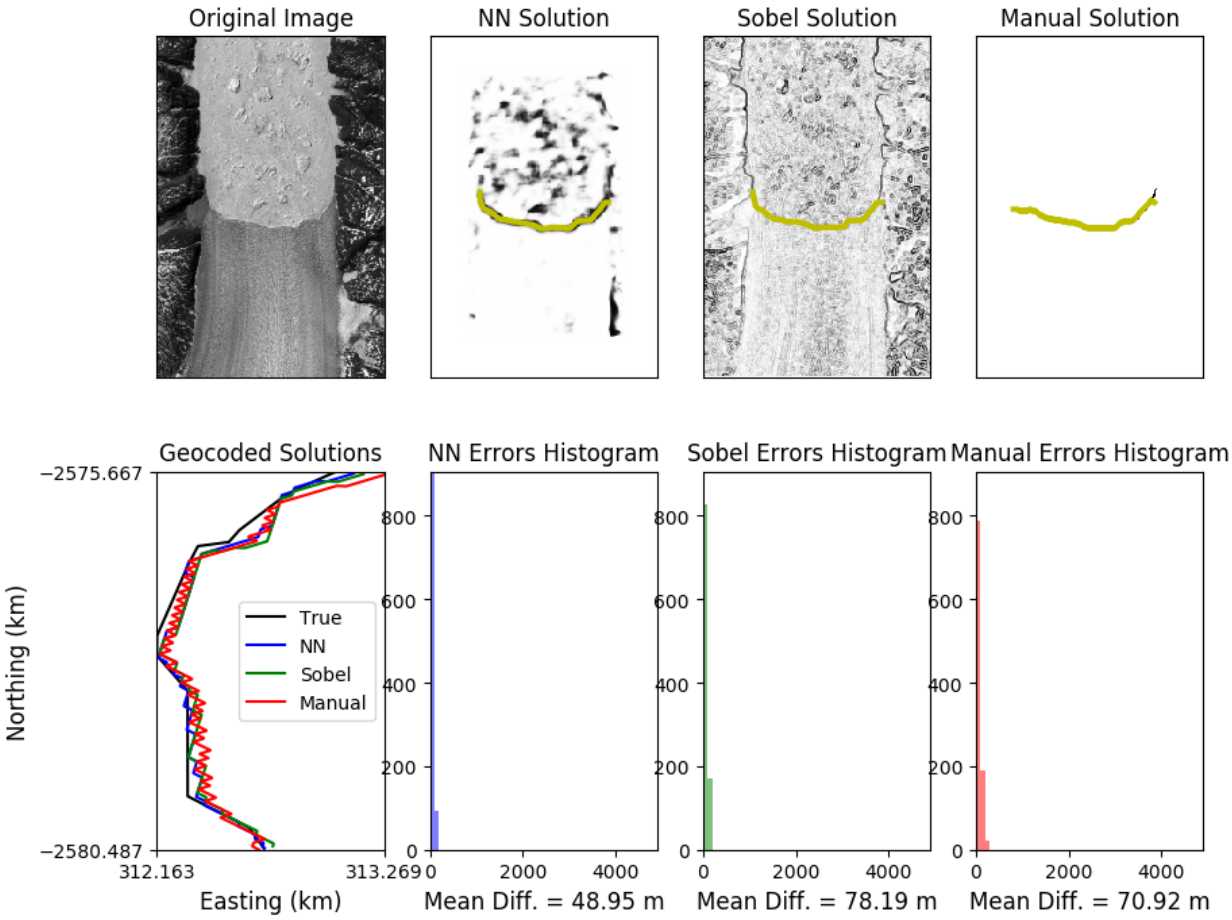

Figure B3.4: Landsat 7 - June 25, 2002

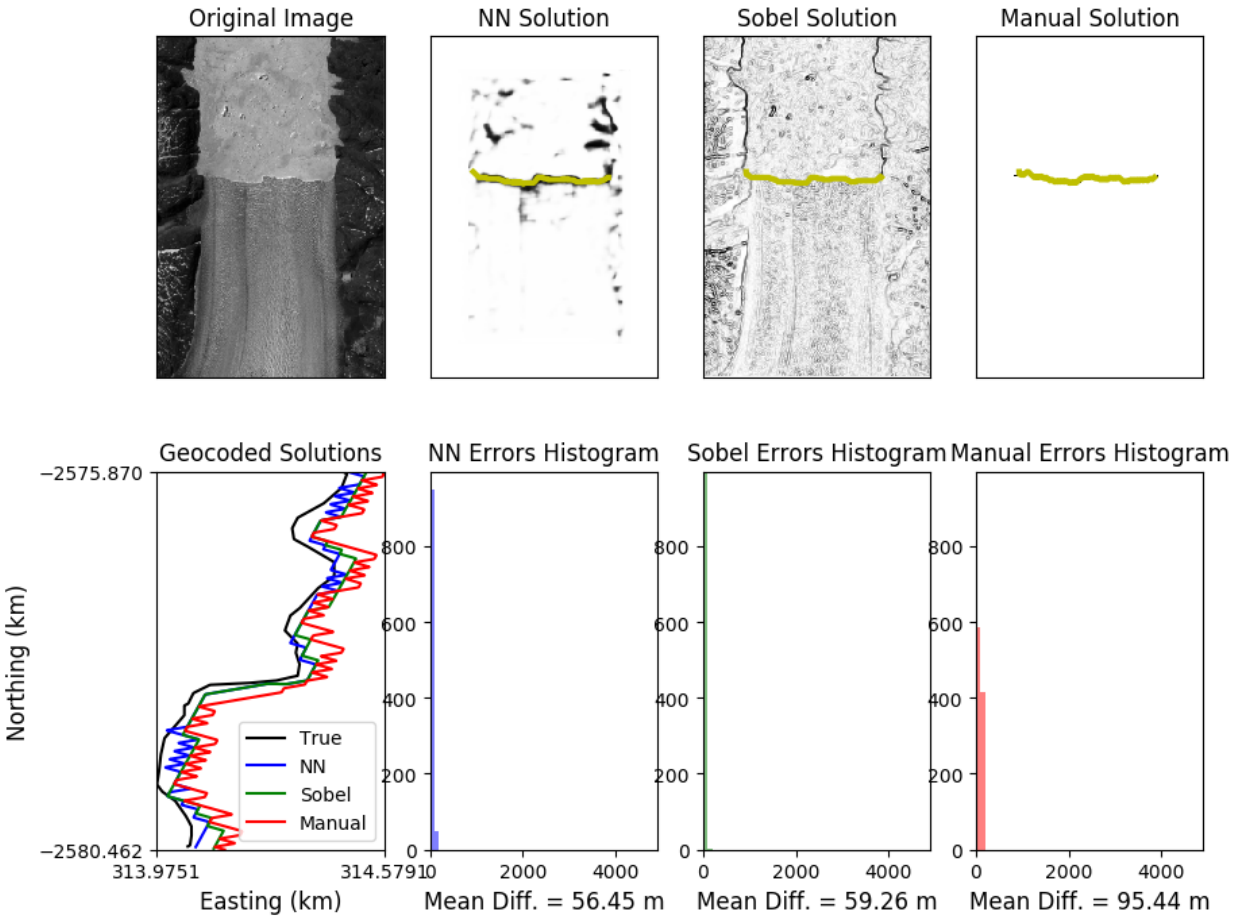

Figure B3.5: Landsat 7 - July 21, 2000

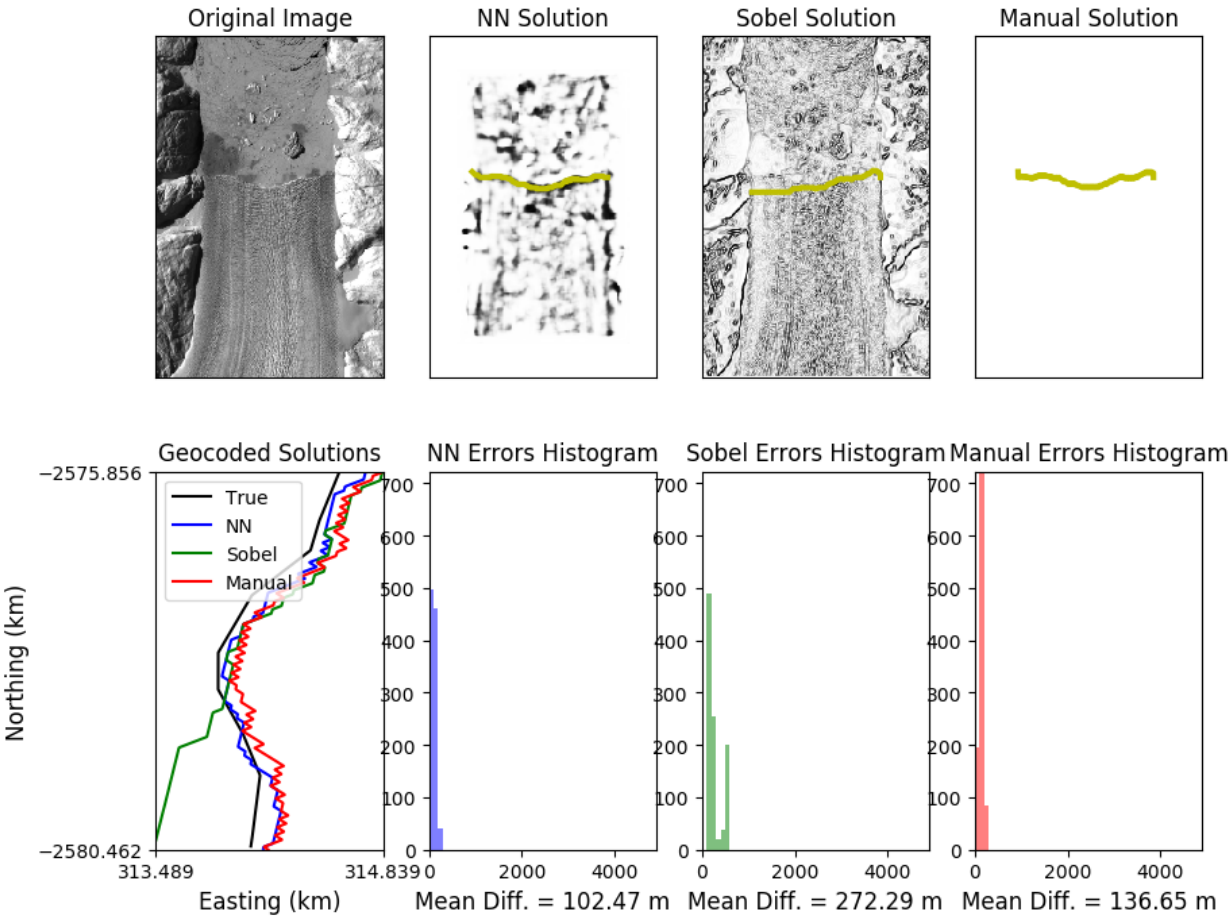

Figure B3.6: Landsat 7 - March 31, 2000

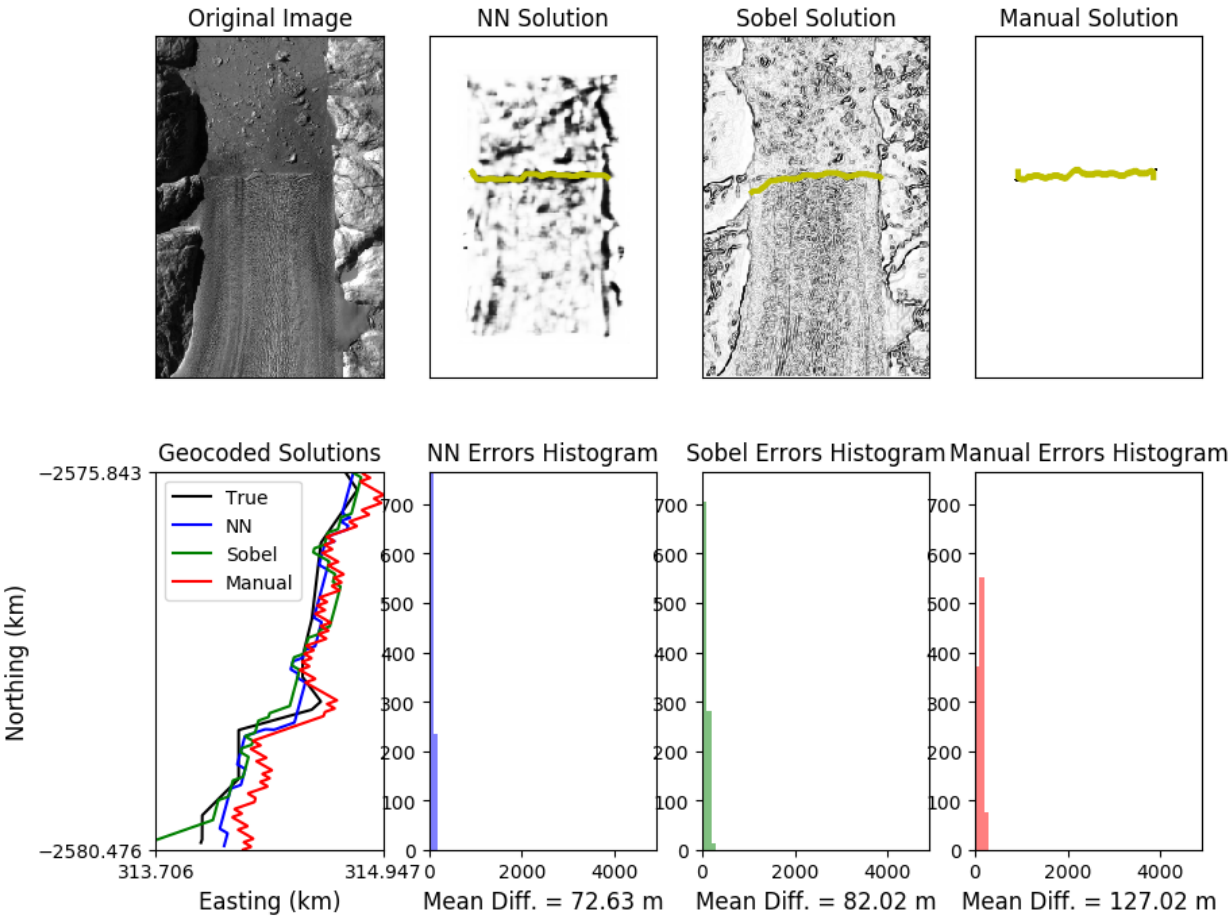

Figure B3.7: Landsat 7 - March 18, 2001

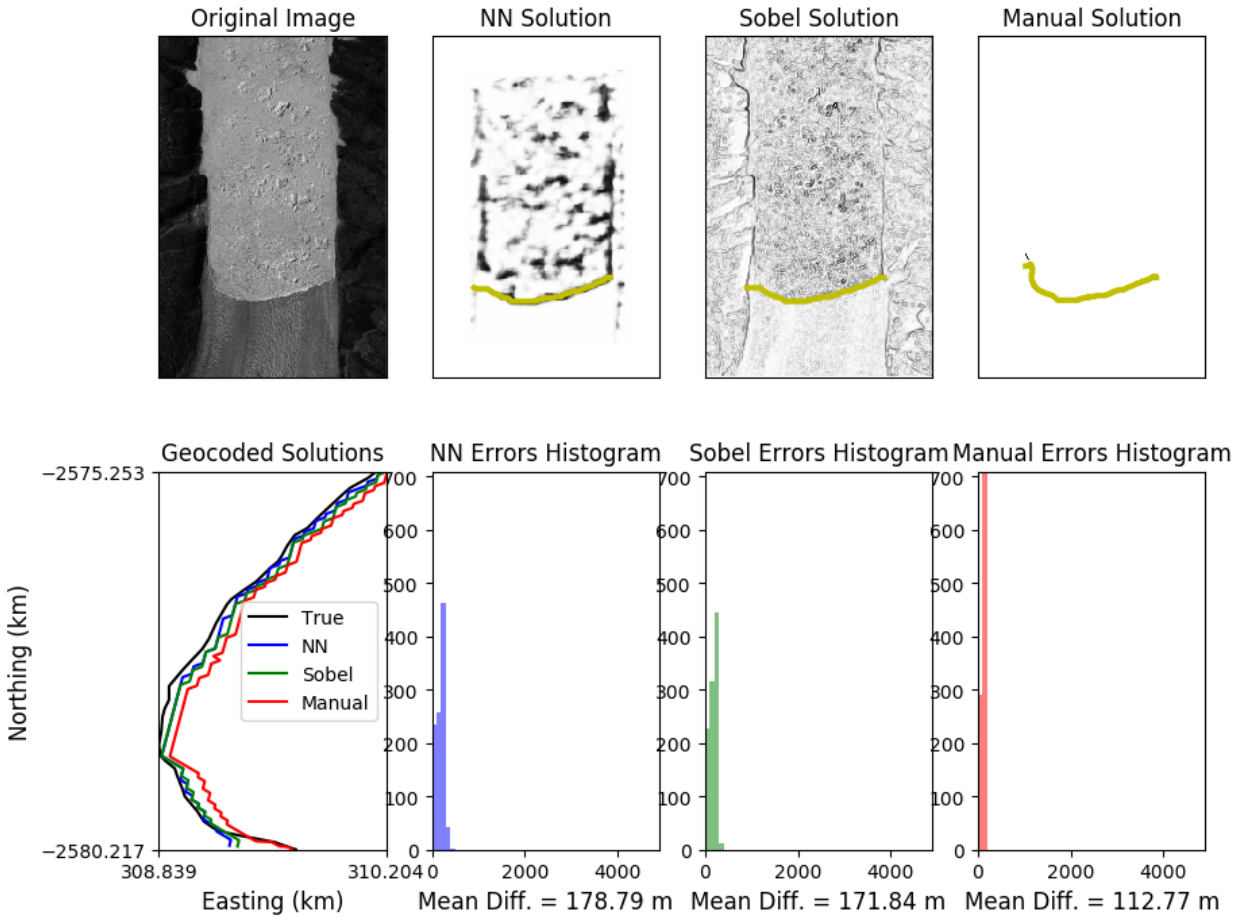

Figure B3.8: Landsat 8 - July 25, 2016

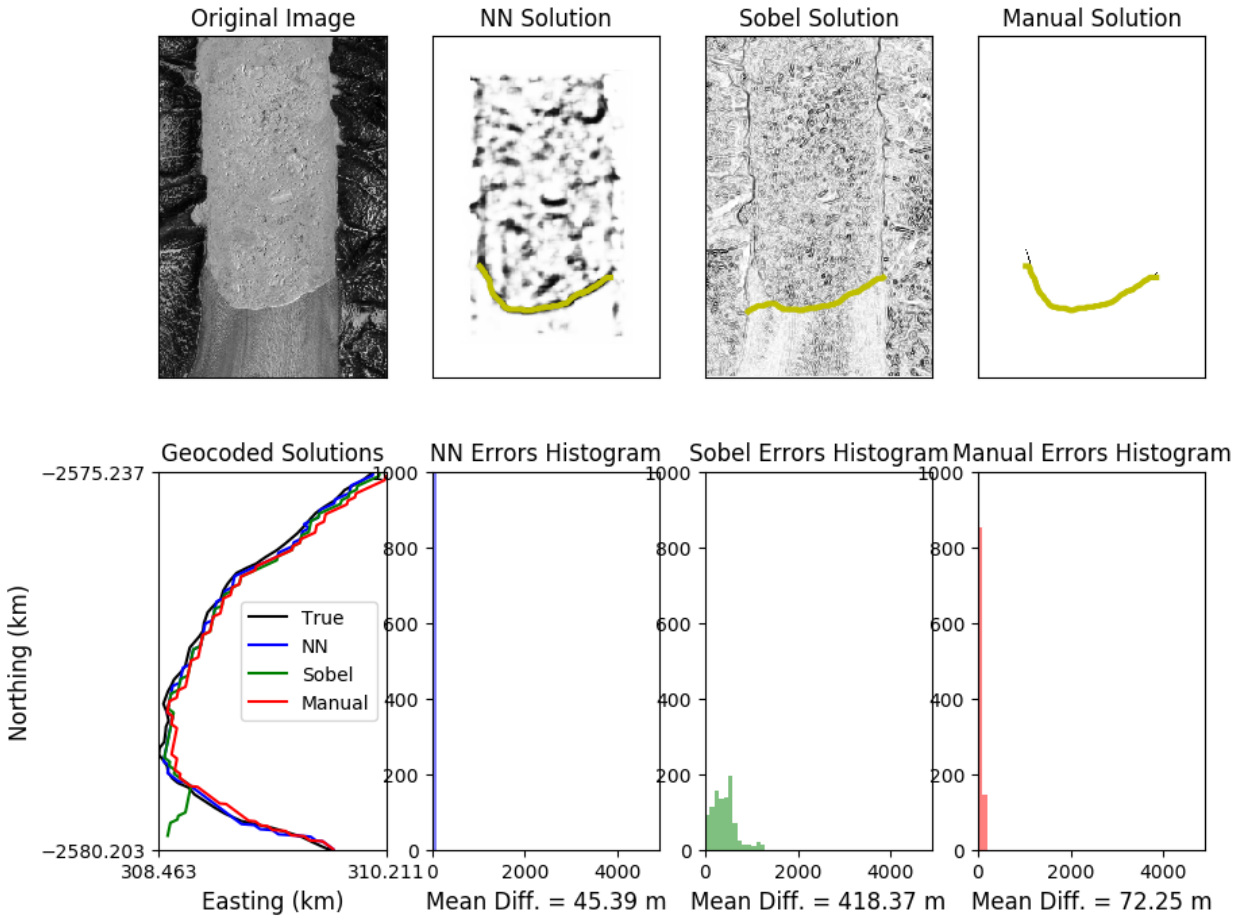

Figure B3.9: Landsat 8 - July 7, 2015

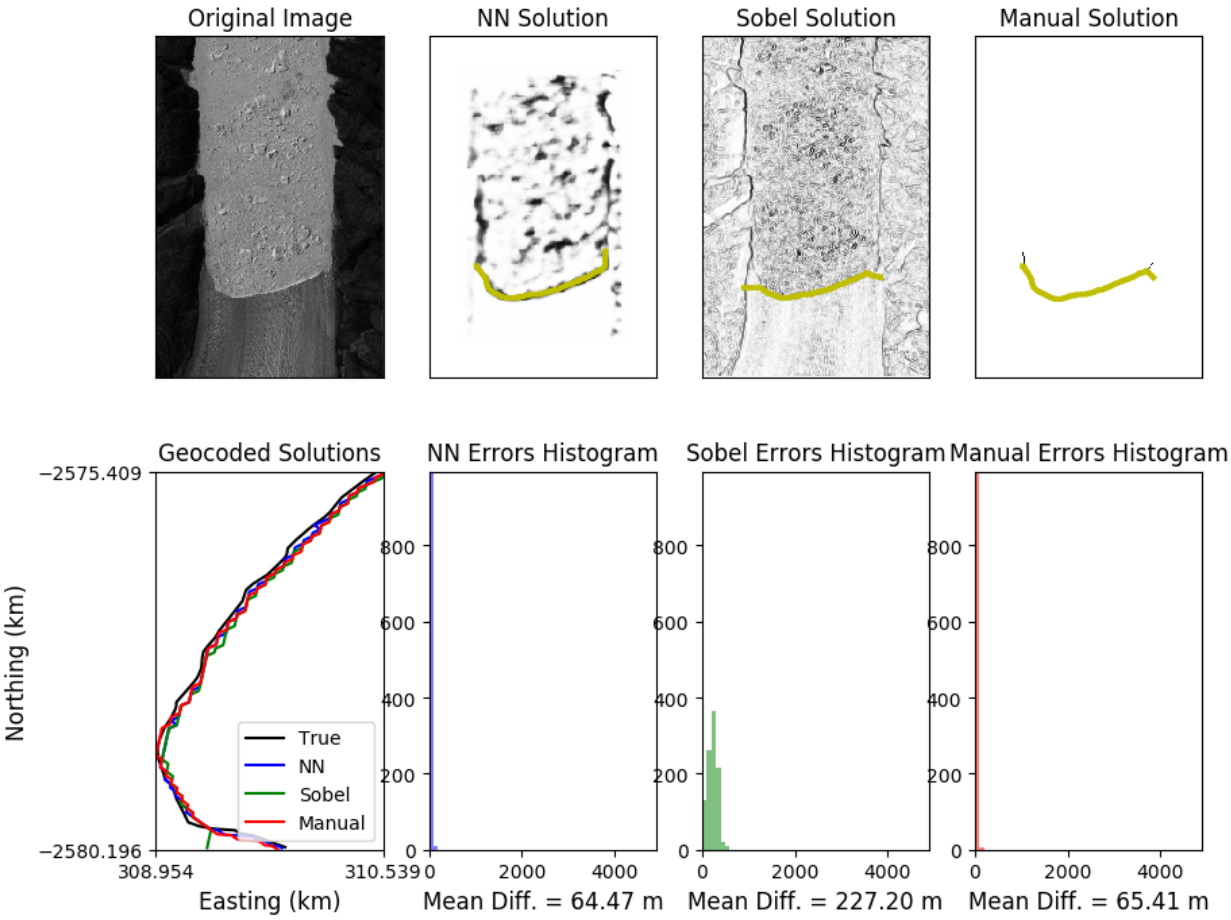

Figure B3.10: Landsat 8 - August 21, 2014